GSI

Diss. 2006 - 12
December

Direct mass measurements beyond the proton drip-line

C. Rauth

(Dissertation Universität Heidelberg)

Gesellschaft für Schwerionenforschung mbH
Planckstraße 1 · D-64291 Darmstadt · Germany
Postfach 11 05 52 · D-64220 Darmstadt · Germany

Dissertation
submitted to the
Combined Faculties for the Natural Sciences and for Mathematics
of the Rupertus-Carola University of Heidelberg, Germany
for the degree of
Doctor of Natural Sciences

presented by

Diplom-Physicist Christian Rauth

born in Saarbrücken, Germany

Oral examination: 07.02.2007

Direct mass measurements beyond the proton drip-line

Referees: Prof. Dr. H.-Jürgen Kluge
Prof. Dr. Andreas Wolf

Direkte Massenmessungen jenseits der Protonenabbruchkante
Das Penningfallen-Massenspektrometer SHIPTRAP wurde an der GSI in Darmstadt aufgebaut, um Präzisionsexperimente mit niederenergetischen Ionen durchzuführen. Diese werden durch Fusions-Evaporations-Reaktionen am Geschwindigkeitsfilter SHIP erzeugt. Im Rahmen der ersten Hochpräzisionsmessungen wurden die Massen von 18 neutronenarmen Isotopen der Elemente Terbium bis Thulium mit relativen Genauigkeiten von ungefähr $7 \cdot 10^{-8}$ bestimmt. Die Masse von neun Nukliden wurde zum ersten Mal gemessen, wovon vier (^{144,145}Ho and ^{147,148}Tm) sogar jenseits der Protonenabbruchkante liegen. Die Daten wurden der Atomaren Massen Evaluation (AME) hinzugefügt und zeigten größtenteils gute Übereinstimmung gegenüber den bereits gemessenen Massen. Die Auswirkungen der Daten auf die Kernstruktur und die Lage der Protonenabbruchkante werden anhand der Zweineutronen- und Einproton-Separationsenergien dargestellt. Mit Hilfe von Simulationen und Offline-Messungen wurde die Stoppeffizienz der Gaszelle untersucht sowie der Kontrast und die Qualität der Messung verbessert. Ungenauigkeiten, die durch Magnetfeldfluktuationen hervorgerufen werden, wurden quantifiziert.

Direct mass measurements beyond the proton drip-line
At GSI in Darmstadt the Penning trap spectrometer SHIPTRAP was set up to perform precision experiments with low-energetic radioactive ions produced in fusion-evaporation reactions at the velocity filter SHIP. First high-precision measurements were performed determining the masses of 18 neutron-deficient isotopes in the terbium-to-thulium region with relative uncertainties of about $7 \cdot 10^{-8}$. The masses of nine nuclides were measured for the first time. Four of them (^{144,145}Ho and ^{147,148}Tm) were determined to lie beyond the proton drip-line. The data were included into the Atomic Mass Evaluation (AME) and showed generally good agreement with previous measurements. The implication of the results on the nuclear structure and on the location of the proton drip-line is discussed by analyzing the two-neutron and one-proton separation energies. Further simulations and off-line measurements were performed to investigate the stopping efficiency in the gas cell, to optimize the contrast and the quality of the measurement and to determine the uncertainties arising from magnetic field fluctuations.

for Nina

The most exciting phrase to hear in science, the one that heralds new discoveries, is not 'Eureka!' but rather, 'hmm... that's funny...'

— Isaac Asimov

Contents

List of Tables

List of Figures

Chapter 1

Introduction

The origin of the chemical elements in our solar system is one of the main questions the growing field of nuclear astrophysics addresses. Several paths of stellar production mechanisms for heavy elements exist that explain the abundance of stable isotopes as we observe it today. Besides the stellar environment where the reactions take place, all known paths depend strongly on input data from nuclear physics like Q-values, branching ratios and decay constants. Calculations of the rp-process, for example, need a precise knowledge of the proton separation energies from the nuclides close to the proton drip-line. In this context, precise mass measurements of exotic nuclei are an essential source of information, especially where spectroscopic investigations are not possible [Sch98a].

Another important field modern nuclear physics research deals with are the borderlines of nuclear stability. While the neutron drip-line is experimentally still only reached for very light elements, the proton drip-line was accessed up to heavy elements like protactinium [Woo97, Nov02]. The first experimental indication of direct (in contrast to β-delayed) proton radioactivity was found in 1970 for the isomeric state ^{53m}Co [Jac70], while the first ground state proton emitter, ^{151}Lu, was discovered at GSI in 1981 [Hof82]. Other proton-decaying nuclides like ^{147}Tm were observed shortly after [Kle82].

Whereas the detection of proton decay is of course sufficient proof of the unbound character of the emitting state, the inverse relation does not necessarily hold: The proton radioactivity of a proton-unbound nuclide may well be too weak to be detected, especially in close vicinity to the proton drip-line. This is due to two effects. First, the Q value of direct proton decay Q_p, which is the negative of the proton separation energy S_p, strongly affects the decay rate. A small Q_p value results in a very low decay rate, i.e., a very long partial half-life, and thus a negligibly small branching ratio compared to the competing β decay. Second, it is experimentally very challenging to discriminate the low-energy proton against the background of β-decay positrons. For these reasons proton emitters are generally found only at some distance from the proton drip-line and can not be used to delineate its location precisely. Precise mass measurements can overcome these problems through a determination of the Q_p value by measuring the masses of the mother and the daughter nuclei of the direct proton decay.

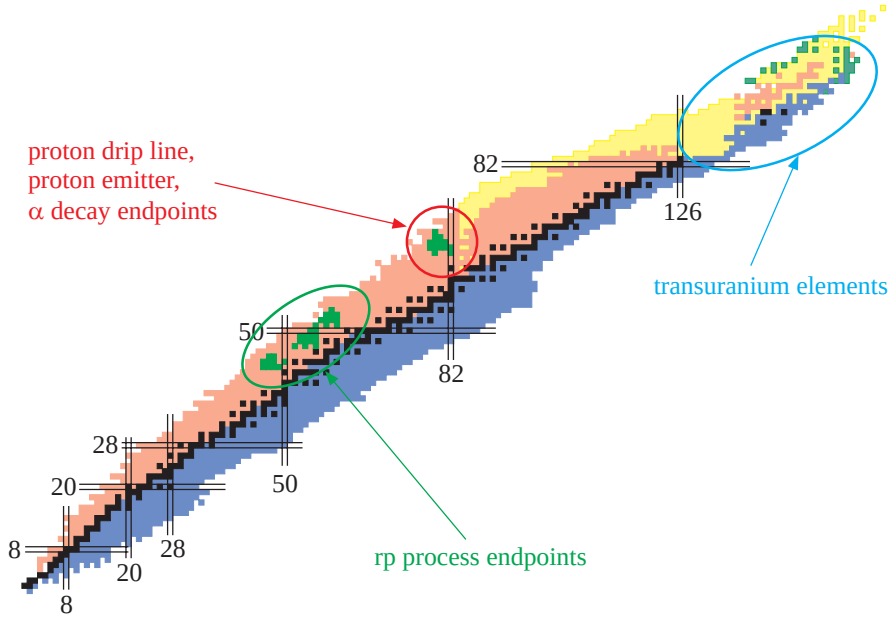

Figure 1.1: Interesting regions of the nuclear chart addressed at SHIPTRAP. The masses of the nuclides indicated by green squares were measured at SHIPTRAP.

Above only two examples were discussed where mass measurements act as an important source of information. Various other domains of physics also benefit from precise mass values, such as weak interaction studies in super allowed β decays [Har05], CPT tests by a comparison of the particle and antiparticle mass [Gab99] and many others [Sch06, Lun03, Bla06]. Depending on the type of investigation the necessary precision of the mass determination ranges from 10^{-5} (molecular mass spectrometry) to 10^{-11} (CPT and QED tests). The most precise mass measurements are performed in Penning traps, in which relative uncertainties of $8 \cdot 10^{-9}$ for radioactive ions [Bol06] and $1 \cdot 10^{-11}$ for stable ones [Dyc04] are currently reached.

At GSI Darmstadt the Penning trap mass spectrometer SHIPTRAP was setup to investigate radioactive ions produced in fusion-evaporation reactions at the velocity filter SHIP. Beside of accurate mass measurements SHIPTRAP addresses other precision experiments with low-energetic nuclides. These are ion-chemical reaction studies in the gas cell and investigations of the nuclear or atomic structure by means of trap-assisted decay or laser spectroscopy.

The in-flight separator SHIP produces neutron-deficient isotopes of medium-heavy to transuranium elements. Figure 1.1 shows three regions SHIPTRAP is concerned with. In the region below ^{100}Sn the rp process is supposed to end in the tin-antimony-tellurium cycle [Sch01], which needs precise mass values to deduce the proton separation energies. The transuranium region is especially interesting since many masses here are only known from extrapolations of systematic trends, which are very imprecise as the distance to experimental data grows [Wap03]. Experimentally, this region is quite challenging because of small production cross-sections ($< 1\,\mu$barn). However, measuring one di-

rect mass helps to pin down several others since many nuclides are linked by well-known α-decay chains.

The first mass measurements performed at SHIPTRAP focused on neutron-deficient terbium-to-thulium isotopes around mass number $A = 146$ and are the main subject of this thesis. This region is particularly interesting because of the proximity to the proton drip-line and the occurrence of ground-state proton radioactivity. Additionally, it contains several nuclides that are the endpoints of long α-decay chains. Pining down these 'base nuclides' allows one to determine also the masses of all connected ones. In this region the production rates at SHIP range from 100 000 ions/s down to only 500 ions/s (s. chapter 4).

Chapter 2 gives a detailed overview of the SHIPTRAP facility including a description of the individual parts and the measurement procedure. In chapter 3 follows a report about several off-line investigation, which helped to increase the quality of the measurements, to gain knowledge about the ion stopping process and to quantify systematic uncertainties. Chapter 4 reports about the on-line mass measurements in the rare-earth elements region. The analysis procedure, the results and their implications on different nuclear physics topics are discussed in detail.

Chapter 2

The SHIPTRAP facility

The Penning trap mass spectrometer SHIPTRAP is located in the low-energy experimental hall at GSI, Darmstadt (s. fig. 2.2). The main features of the facility are indicated in fig. 2.1. The radioactive ions to be investigated at SHIPTRAP are produced at the in-flight separator SHIP. First, they are stopped in a buffer gas cell. After extraction the ions are accumulated and cooled in a helium-filled radiofrequency quadrupole (RFQ) structure. The final mass separation and analysis takes place in two Penning traps. This chapter gives some detailed descriptions of these main components and the working principles of the SHIPTRAP facility.

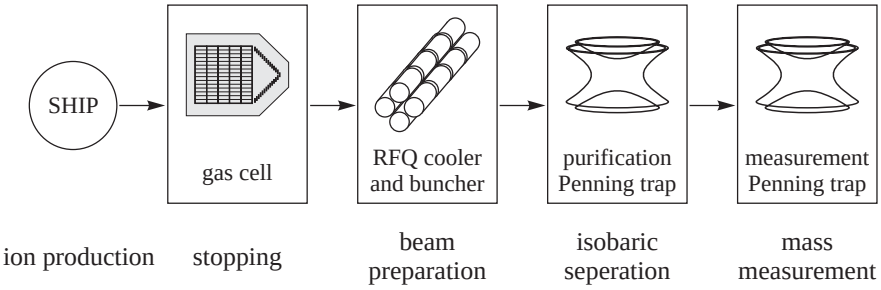

Figure 2.1: Main components of the SHIPTRAP facility. The radioactive ions delivered by SHIP are stopped in the gas cell, accumulated and cooled in the radiofrequency quadrupole (RFQ) buncher and finally isobarically separated and mass analyzed in two Penning traps.

2.1 The velocity filter SHIP

The **S**eparator for **H**eavy **I**on Reaction **P**roducts (SHIP) was one of the first experiments at GSI [Mün79] and world-wide known for the production and detection of super-heavy elements [Hof00]. The first discovery of the elements $Z = 107 - 111$ was done here and led to the honor of suggesting their names to the IUPAC.

A schematic overview of SHIP is shown in fig. 2.3. The heavy and superheavy elements are produced in fusion-evaporation reactions when a high-

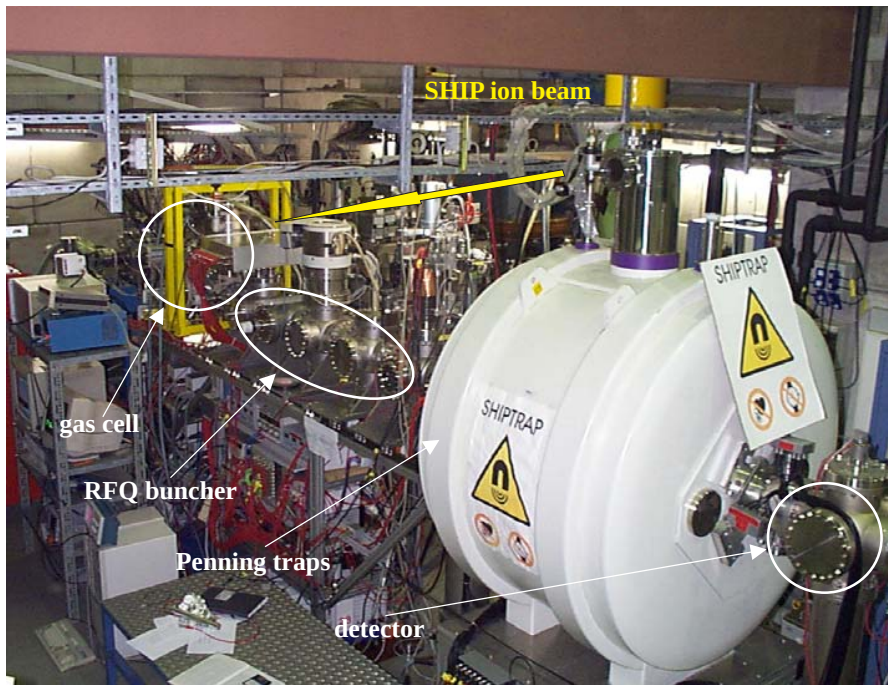

Figure 2.2: Photograph of the SHIPTRAP setup. The SHIPTRAP beamline is perpendicular to the direction of the beam delivered from SHIP. In the yellow frame the gas cell is located. The three subsequent vacuum crosses contain the RFQ buncher. The Penning traps are situated in the white superconducting magnet. The beamline ends with the detector vacuum cross.

intensity (particle-μA) primary beam impinges on a thin metal target foil. The primary beam energy around 5 MeV/u has to be chosen carefully. On the one hand, the energy has to be high enough to enable the nucleus of the projectile to penetrate through the Coulomb barrier of the target nucleus. On the other hand, a too high beam energy leads to a highly excited compound nucleus that decays almost immediately by fission. Chosen the right beam energy the compound nucleus cools down by evaporation of few nucleons or α particles depending on its excitation energy.

The fusion reaction products leave the target foil due to the recoil momentum transfer with typical energies of few 100 keV/u. They are kinematically separated from the primary beam by a double Wien filter, which is a special combination of electrostatic and magnetic deflectors. The homogeneous fields are chosen perpendicular to each other and to the beam direction, which leads to a beam deflection that is only dependent on the velocity of the ion and not on its mass-to-charge ratio. This separation method is advantageous for fusion-evaporation reactions since the charge state distribution of the reaction products is usually very broad. The transmitted velocity class can be changed by varying the electric or magnetic field strength.

Two quadrupole triplets and a dipole magnet are used to focus and deflect the beam onto arrays of position sensitive silicon detectors. Here, the super-

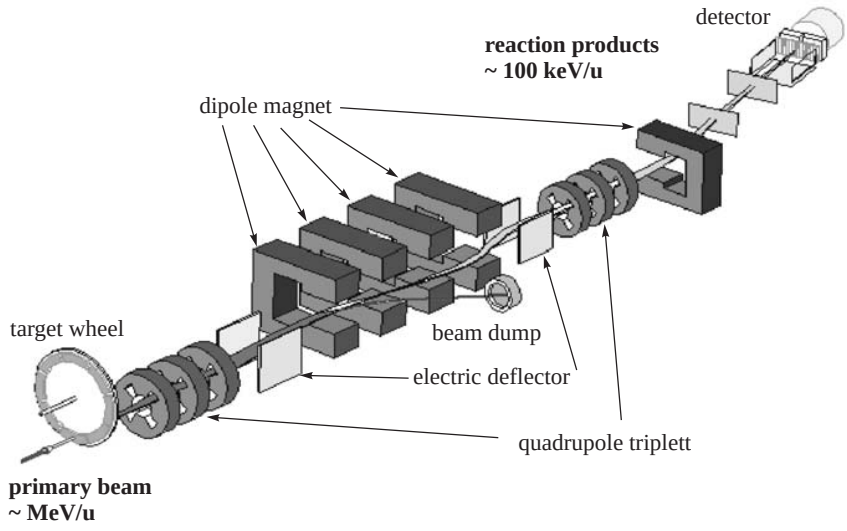

Figure 2.3: Overview of the SHIP separator. The primary beam impinges on a thin target foil to produce radioactive ions in fusion-evaporation reactions. In a double Wien filter geometry, which consists of crossed homogeneous electric and magnetic fields, the slower reaction products are kinematically separated from the primary beam.

heavy elements are identified by detecting the α-decay chains of the implanted reaction products. For on-line experiments at SHIPTRAP the SHIP-detector is removed and a beamline to the gas cell mounted.

The energies of the reaction products range from 10 - 1000 keV/u. Depending on the location in the foil where the fusion reaction takes place the produced ions experience different energy losses in the remaining path through the window.[1] The changing energy loss results in an energy spread in the order of 10 - 30 % mainly defined by the thickness of the target foil.

The suppression of the primary beam depends on the velocity ratio between the primary beam v_p and the reaction products v_c

$$\frac{v_c}{v_p} = \frac{m_p}{m_c} \quad , \tag{2.1}$$

where m_p is the mass of the projectile and $m_c = m_p + m_t$ the mass of the compound nucleus, which is the sum of projectile and target nucleus mass m_t. The equation shows that for a given compound nucleus the best suppression can be achieved by using a light projectile on a heavy target. Typical suppressions achieved are 10^7 - 10^{11} [Mün79].

The total efficiency of SHIP, which is the ratio between the number of particles seen at the detector and the produced ones, depends among other things on

[1] For thin foils, $< 1\,\mathrm{mg/cm^2}$, the energy loss of the primary beam can be neglected since the excitation function and therewith the number of produced ions is more or less constant.

the excitation energy and the mass of the projectile. A higher excitation energy leads to a higher number of evaporated particles that increases the angular straggling [Mün79]. Since the acceptance of the filter is fixed less particles will arrive at the detector. The same argument holds for the mass of the projectile. A lower mass results again in a higher angular straggling and a lower efficiency [Fau79]. The total efficiency was measured e.g. for the reaction $^{150}\mathrm{Nd}\,(^{40}\mathrm{Ar}, 6n)\,^{184}\mathrm{Pt}$ to 14(1) % [Mün79].

Summing up what was said above one recognizes that a high suppression demands for light projectiles, while heavy ones yield in a high efficiency. However, in practice the lower efficiency of the light projectiles is usually overcompensated by a higher beam intensity that is available for the light-ion beams. For this reason light projectile beams from argon, calcium, chromium or nickel are usually favorable.

In general one should try to avoid symmetric reactions (same projectile as target material) because of an inseparable background of primary beam in this case. The background results from the small fraction of ions that enter the accelerator out of phase and are not accelerated to the full energy. They arrive at SHIP with roughly half the velocity of the 'right' ions, which is also the velocity of the reaction residues, and can therefore not be separated by the velocity filter.

2.2 The experimental setup of SHIPTRAP

Behind SHIP and perpendicular to its beam direction SHIPTRAP was set up. Figure 2.4 shows a schematic overview of the facility. The individual parts are described in the following sections.

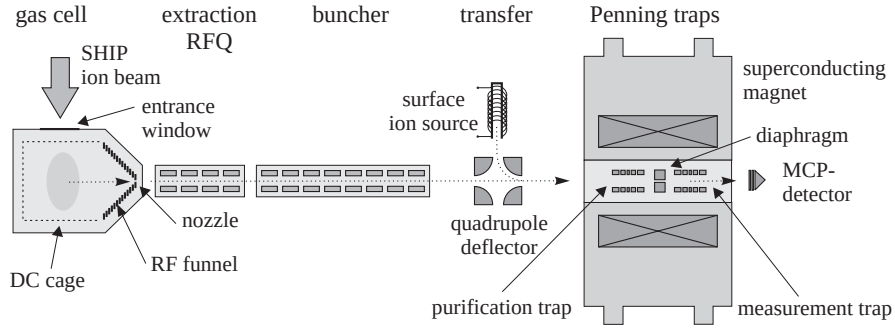

Figure 2.4: Schematic overview of the SHIPTRAP experiment. The radioactive ions delivered by SHIP are stopped (gas cell section), extracted and guided (extraction RFQ section), accumulated and cooled (buncher section) and transferred (transfer section) into the 7 T superconducting magnet (trap section). After isobaric cleaning (purification trap) the cyclotron frequency is determined (measurement trap).

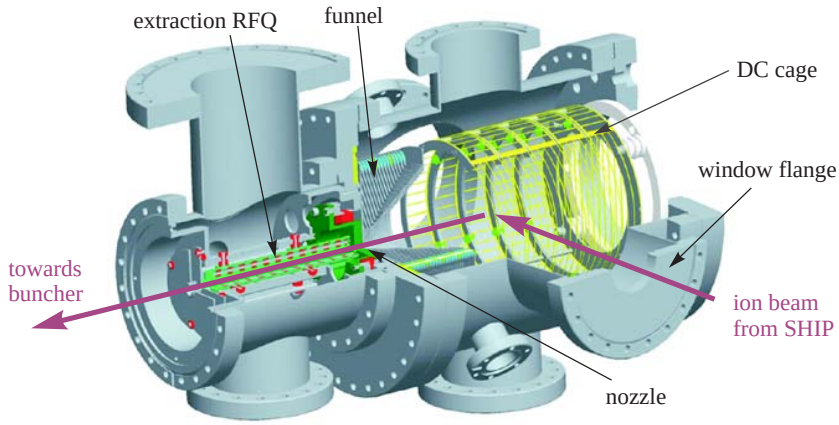

Figure 2.5: The SHIPTRAP gas cell and extraction RFQ. The radioactive ions from SHIP enter the cell through a window foil and are stopped by collisions with the buffer gas. Electrical DC (cage) and RF fields (funnel) guide the ions into the nozzle region. Here, a supersonic gas jet drags them out into the extraction RFQ that acts as an ion guide and provides differential pumping.

2.2.1 The gas cell

In comparison to other on-line Penning trap experiments like ISOLTRAP [Bol96, Her01] or JYFLTRAP [Kol04] the energy of the in-flight SHIP beam is much larger. To accept the full beam with a transversal spread of $50 \times 30\,\mathrm{mm}^2$ and an energy spread of 10 % at 50 - 100 MeV a dedicated gas cell was designed and built up [Neu06].

Figure 2.5 shows the design of the gas cell of SHIPTRAP setup. The ions from SHIP enter the gas cell through a few μm thin window foil, where the main energy loss happens. They are furthermore decelerated and finally thermalized by collisions with the helium buffer gas. The pressure, typically around 50 mbar, and the thickness of the window foil have to be chosen very carefully to ensure an efficient stopping inside the cell. The optimum values of pressure and foil thickness depend strongly on the absolute energy and the energy spread of the SHIP beam, which is mainly determined by the type of projectile and target in the fusion-evaporation reaction but also by the primary beam energy. For every new experiment the window foil and the pressure have to be chosen and optimized individually. This topic is discussed in more detail in section 3.1.

Each ion creates 10^5 or more $He^+ + e^-$ pairs in the stopping process [Huy02]. In order to prevent the radioactive ions from recombining with the electrons they have to be dragged out of the stopping volume as quickly as possible. This is done by electric fields from the DC cage (s. fig. 2.5), a longitudinally five times segmented wire structure, where typical voltages of 100 - 300 V create the necessary potential gradient. A funnel structure consisting of 40 concentric ring electrodes forces the ions further towards the nozzle region by applying an electric DC slope. Additionally a RF voltage creates a pseudo potential well to prevent the ions from hitting the structure. In the close vicinity of the nozzle,

Table 2.1: Important parameters of the gas cell and the extraction RFQ. The values marked with * are only approximate and have to be optimized for different ion species.

parameter	value
pressure after backing	$< 1 \cdot 10^{-9}$ mbar
helium gas pressure	40 mbar*
cage DC voltages	120-300 V
funnel DC voltages	90-120 V
funnel frequency	850 kHz
funnel RF amplitude	165 V_{pp}
nozzle voltage	90 V*
RFQ frequency	1 MHz
RFQ RF amplitude	400 V_{pp}

the viscous drag force of the supersonic gas flow finally drags the ions out of the gas cell. They drift into the extraction radiofrequency quadrupole (RFQ), which is a longitudinally segmented linear Paul trap similar to the buncher as will be explained in more detail in the next section. Guiding the ions towards the buncher the extraction RFQ allows one to differentially pump away the helium.

The important parameters of the gas cell are summarized in tab. 2.1. The gas pressure, usually between 40 - 60 mbar, has to be adapted to the kinetic energy of the reaction products for an efficient stopping process (s. section 3.1). The DC voltages on the cage and the RF amplitude at the funnel should be as high as possible to maximize the extraction efficiency. The most sensitive parameter is the potential difference of typically few Volt between the last funnel ring and the nozzle electrode. The voltages have to be tuned such that the drift velocity of the ions matches the velocity of the effusing helium gas.

The typical extraction times are in the order of 10 ms. This is mainly determined by the drift time in the gas cell, which depends on the gas pressure and the applied potentials. The extraction time sets the limit of measurable radioactive ions regarding their half-lives. If the half-life of a nuclide is smaller than the extraction time the majority of ions will decay already in the gas cell.

The total efficiency $\epsilon_{\text{gas cell}}$ of the gas cell, i.e., the number of ions leaving the extraction RFQ divided by the number of ions impinging on the window can be described by

$$\epsilon_{\text{gas cell}} = \epsilon_{\text{stop}} \times \epsilon_{\text{extr}} \tag{2.2}$$

as the product of stopping efficiency ϵ_{stop} and extraction efficiency ϵ_{extr}. While former one is hard to measure and was so far only deduced from simulations to roughly 30 % (s. section 3.1), ϵ_{extr} has been studied extensively using a radioactive ^{223}Ra ion source inside the gas cell [Eli06a]. The studies show that many correlated parameters, such as the pressure, the amplitude of the funnel RF voltage and the location in the stopping cell, influence ϵ_{extr}, which is typically

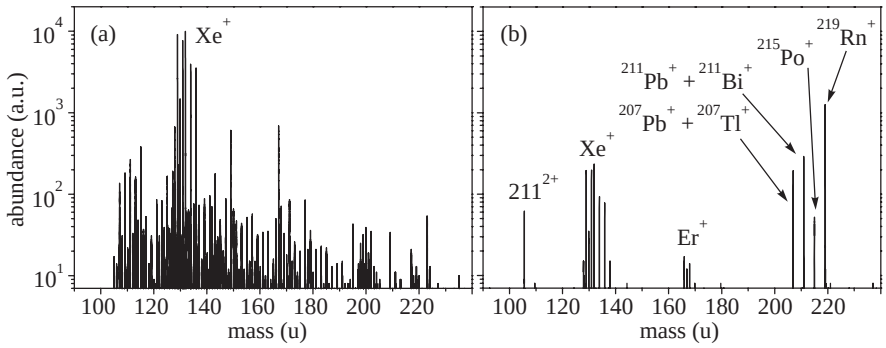

Figure 2.6: Mass spectra of the ions extracted from the gas cell before (a) and after baking of the cell for 20 h at 150 °C (b). The ^{219}Rn ions coming from a radioactive ion source in the gas cell and their decay products produce all other ions by charge exchange processes. The Xe^+ ions stemming from the helium gas can be frozen out in a liquid nitrogen cold trap.

between 10 - 20 %. The total efficiency was measured in several on-line experiments at the Maier-Leibnitz Laboratory (MLL) in Garching and at GSI with maximum values of 5 - 8 % [Neu06].

The studies of the extraction efficiency also showed that the residual gas pressure in the gas cell and the purity of the buffer gas are two extremely important issues: High residual gas pressures or impurities in the helium gas reduce the efficiency due to charge exchange processes or molecule formation. Good vacuum conditions can be achieved first of all by using appropriate materials with low outgassing rates like stainless steal or Al_2O_3 as well as oil-free vacuum pumps. The gas cell and the extraction RFQ are pumped by turbomolecular pumps with pumping speeds of 400 l/s and 1600 l/s, respectively, in combination with a oil-free scroll pump (20 m^3/h). Moreover, the necessary purity is obtained by careful baking of the cell for typically 1 - 3 d at 120 - 150 °C, which yields in residual gas pressures below $1 \cdot 10^{-9}$ mbar. The impact of baking on the gas cell impurity is visualized in fig. 2.6. With a quick-scanning broadband time-of-flight mass spectrometer (Ortho-TOF) [Eli02] the ions extracted from the gas cell were investigated. As ion source a filament of ^{223}Ra was introduced producing in the subsequent decay chain ions from ^{219}Rn to ^{207}Pb. Graph (a) shows the situation when the gas cell is only pumped for several days with a typical residual gas pressure of few 10^{-8} mbar. At almost every mass number some ions are created through charge exchange with the radioactive ions. After baking for only 20 h at a moderate temperature of 150 °C a pressure of $8 \cdot 10^{-10}$ mbar is achieved and almost all impurities disappear (b). The spectrum shows even doubly charged ions, which is a clear indication of the low density of impurities that have a high cross section for charge exchange with doubly charged ions. The remaining Xe impurities are introduced with the helium gas, even though a purity grade of 6.0 was chosen (99.9999 % He). They are effectively reduced by using a 'cold trap': The helium feeding line, a long metal tube, is put in a liquid nitrogen bath freezing out all remaining impurities.

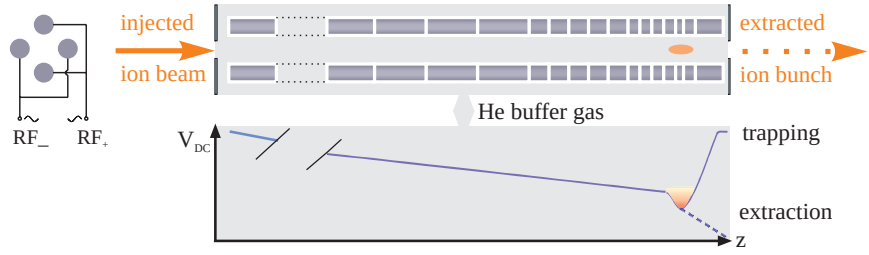

Figure 2.7: Schematic setup of the SHIPTRAP RFQ buncher. Top: Front and side view with electric connections. Bottom: Longitudinal DC potential. Due to collisions with the helium buffer gas the ions are cooled into the potential minimum. The DC voltage of the last segments can be lowered to eject the ions as a bunch.

2.2.2 The RFQ buncher

The SHIPTRAP RFQ buncher [Rod02] accumulates the ions coming as a quasi-dc beam from the gas cell for typically 1 s and ejects them afterwards as a temporally defined bunch. Furthermore, it cools the ion cloud to decrease the emittance of the ejected ion beam, which is mandatory for an efficient injection into the superconducting magnet.

The schematic setup is shown in fig. 2.7. The RFQ buncher is similar to a linear Paul mass filter as it is used for rest gas analysis [Her03]. A RF voltage applied to four parallel rods creates a pseudo-potential well that radially confines the ions. However, helium as a buffer gas with a typical pressure of $5 \cdot 10^{-3}$ mbar is introduced. By collisions with the helium atoms the ion motion is damped and the ion cloud is radially cooled. Furthermore, the rods are longitudinally segmented to apply a DC potential well as it is shown in fig. 2.7. Due to the collisions with the buffer gas the ions are also longitudinally cooled and trapped at the location of the potential minimum. For ejection the DC voltage of the last electrodes can be lowered. If this segment is permanently in the lower state the buncher can be also used as ion beam cooler and guide.

Since the buncher is generally used without additional quadrupolar DC field (RF-only mode) and due to the buffer gas its mass resolving power is typically

Table 2.2: Important parameters of the RFQ buncher and cooler. V_{switch} is the DC voltage of the last longitudinal segment when it is closed (open).

parameter	value
helium gas pressure	$5 \cdot 10^{-3}$ mbar
buncher frequency	850 MHz
buncher RF amplitude	180 V_{pp}
DC voltage slope	74-60 V
V_{switch}	90 V(0 V)

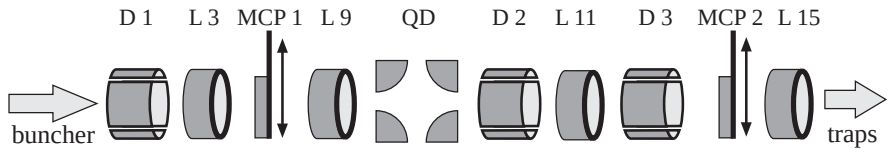

Figure 2.8: Main components of the transfer section. Two lenses (L 3 and L 9 and one deflector (D 1) thread the ion beam through the small aperture of the quadrupole deflector (QD). Two deflectors (D 2 and D 3) and lenses (L 11 and L 15) are used to efficiently inject the ions into the magnet. The remaining eleven lenses (not shown) stay on the common transfer potential of −940 V. Two multi-channel plate (MCP) detectors can be introduced for optimizing the transfer efficiency.

lower than 50. However, it can be used as a 'high-pass' to reduce the number of low-mass ions like helium, water and nitrogen, which are usually created in high amounts in the gas cell through charge-exchange processes (s. section 2.2.1). To get rid of contaminant ions in the medium-mass region an additional dipole excitation can be applied to the electrodes at the potential minimum.

The important parameters of the RFQ buncher are listed in tab. 2.2. The typical widths of the extracted pulses are around 2 μs. The efficiency ϵ_{bunch}, which is the ratio between the number of ions entering the buncher to the ones leaving it, is almost 100 % without and in the order of 50 % with bunching [Rod02].

2.2.3 The transfer section

The transfer section consists of ion-optical components to steer and focus the ion beam ejected from the buncher into the magnet. It consists of three electrostatic deflectors and 15 tubes, from which only 4 are used to establish Einzel lenses while the other eleven remain on the common transfer potential of −940 V. The main components are shown in fig. 2.8. The potentials applied to the electrodes are listed in tab. 2.3. The first deflector and two lenses are used to transfer the

Table 2.3: Settings of the ion-optical elements (c.f. fig. 2.8) in the transfer section used during the beamtime in October 2005. The values depend on the mass-to-charge ratio of the investigated ions.

electrode	voltage (V)
deflector D 1 (up/down/left/right)	-910/-970/-960/-920
lens L 3	-240
lens L 9	-190
deflector D 2 (up/down/left/right)	-940/-940/-940/-940
lens L 11	-300
lens L 15	-1000
deflector D 3 (up/down/left/right)	-940/-940/-940/-940

ions through the small aperture of the quadrupole deflector. The second set of lenses and deflectors are necessary for the efficient injection into the magnet. Both, the direction as well as the divergence have to be optimized carefully, otherwise the ion beam is reflected in the steep magnetic field gradient.

The transfer section also includes two multi-channel plate (MCP) detectors. MCP 1 is the first detector after the gas cell and used whenever some gas-cell or buncher settings are being optimized. MCP 2 allows one to confirm the undisturbed transfer through the quadrupole deflector and measure the number of ions coming from the off-line ion sources.

The quadrupole bender enables one to inject not only ions from the gas cell or buncher into the magnet but also from off-line devices mounted perpendicular to the beam line. On one side a surface ion source is attached providing cesium, rubidium and potassium ions, which are used for reference measurements and optimization. On the other side alternative ion sources, like a carbon-cluster ion source [Cha06], but also diagnostic tools like a quick-scanning broadband time-of-flight mass spectrometer (Ortho-TOF) [Eli02] have been mounted.

2.2.4 The Penning traps

The basics of Penning traps

$$\nu_z = \frac{1}{2\pi}\sqrt{\frac{qU_0}{md^2}} \tag{2.3}$$

A Penning trap is an instrument in which a quadrupole electric potential is combined with a homogeneous axial magnetic field allowing one to store charged particles in free space [Deh90, Bro86]. The quadrupole field is usually achieved by applying a voltage between two hyperbolically shaped end-cap electrodes and a ring electrode as shown on the left side of fig. 2.9. Another common Penning trap type is the cylindrical trap as it is used at SHIPTRAP and shown in fig. 2.11. The main advantages of this geometry are the unproblematic in- and

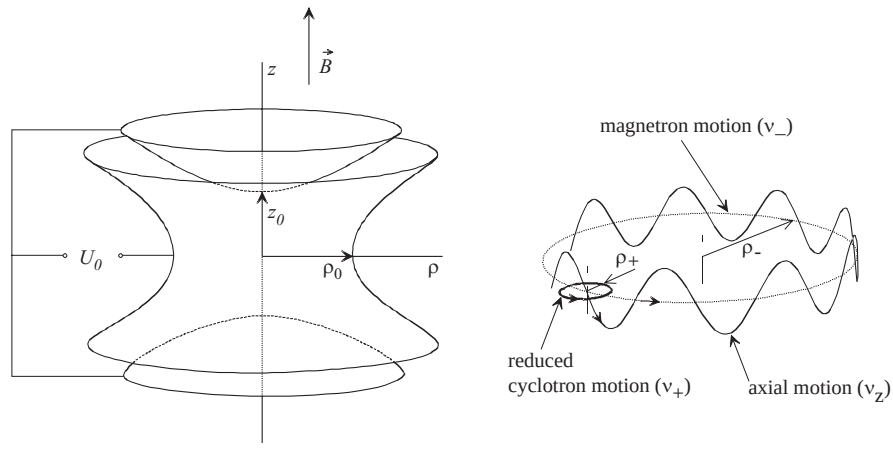

Figure 2.9: Left: Hyperboloidal Penning trap. Right: The evolution of an ion in a Penning trap is a superposition of three characteristic eigenmotions.

ejection of the ions due to the open apertures and the simpler manufacturing process. However, the volume in which a pure quadrupole field exists is smaller in a cylindrical compared to the hyperboloidal trap. This reduction of the harmonic field region can be circumvented by using additional correction electrodes [Gab84, Gab89].

The equation of motion for a charged particle in a Penning trap resulting from the Maxwell equations can be solved analytically. The evolution of an ion with mass m and charge q is a superposition of three characteristic harmonic eigenmotions as shown on the right side of fig. 2.9: The ion oscillates axially with a frequency depending on the electric potential U_0 and the characteristic dimension of the trap $d = \sqrt{z_0^2 + \rho_0^2}$. The radial motion is a superposition of the slow magnetron motion with frequency ν_- and fast modified cyclotron motion with frequency ν_+:

$$\nu_\pm = \frac{\nu_c}{2} \pm \sqrt{\frac{\nu_c^2}{4} - \frac{\nu_z^2}{2}} \quad , \tag{2.4}$$

where ν_c is the true cyclotron frequency, i.e. the frequency with which the ion circulates in a pure magnetic field B

$$\nu_c = \frac{1}{2\pi}\frac{q}{m}B \quad . \tag{2.5}$$

An expansion of eq. (2.4) shows that ν_- is in first order independent of the ion mass but only depends on the electric and magnetic field strengths. Another important fact resulting from eq. (2.4) is that the sum frequency of the radial eigenmotions is exactly the cyclotron frequency

$$\nu_- + \nu_+ = \nu_c \quad , \tag{2.6}$$

which can be exploited to determine ν_c (s. below).

Each of the three eigenmotions can be excited with a *dipolar* RF field by tuning the excitation frequency ν_d to the corresponding eigenfrequency. Like the forced harmonic oscillator the energy transfer is maximal if ν_d exactly equals the characteristic resonance frequency. The excitation by a dipolar RF field results in an increased amplitude or radius of that particular motion. It is usually used for two purposes: Applying an RF field with the mass-dependent modified cyclotron frequency can selectively purify the ion cloud from one ion species. Their radius is increased until they hit the wall of the trap. The dipolar excitation is also used to generally increase the radii of all ions in the trap by tuning ν_d to the mass-independent magnetron frequency. Both techniques are applied in the measurement cycle of SHIPTRAP as described below.

While the dipolar excitation affects one eigenmotions independently from each other, an azimuthal *quadrupolar* RF field couples two motions. This allows one to transfer energy from one eigenmotion into the other and vice versa. The efficiency of the transfer depends on the excitation frequency ν_q. For example, for a maximal energy transfer between magnetron and modified cyclotron frequency ν_q needs to be exactly the sum frequency, which is, as seen in eq. (2.6), the cyclotron frequency.

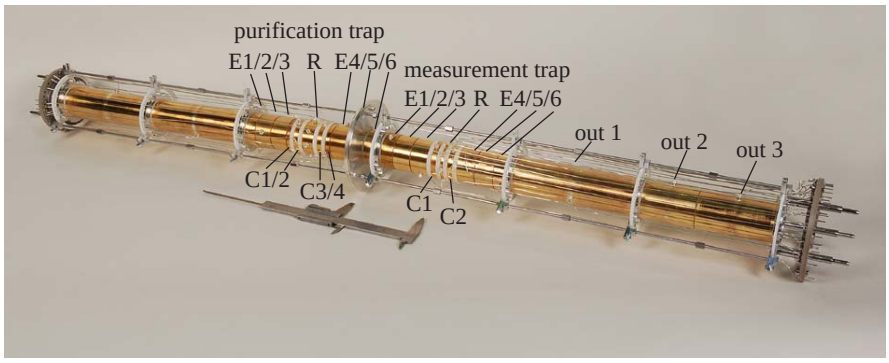

Figure 2.10: Photograph of the Penning traps at SHIPTRAP. The purification (left) and measurement trap (right) consist of 20 cylindrical end-cap, correction and ring electrodes (c.f. fig. 2.11).

The dipolar and quadrupolar fields are technically realized by an azimuthal segmentation of the ring electrode. For a dipolar excitation two segments are necessary, for a quadrupolar four. The RF voltage is divided into a positive and a negative phase, which are applied onto opposite (dipolar) or neighboring segments (quadrupolar, c.f. fig. 2.7). The ring electrodes of SHIPTRAP are eightfold segmented allowing one to manipulate the ions also with an octupolar RF field [Eli06b].

The Penning traps at SHIPTRAP

The cylindrical Penning traps of SHIPTRAP [Sik03, Rah05], as shown on the photograph in fig. 2.10, are situated in two homogeneous regions of a superconducting magnet with a field strength of 7 T. Figure 2.11 shows a drawing of the electrodes and the predominant electric and magnetic fields. The traps are separated by a channel, which is necessary for the mass selection procedure used in the first trap (purification trap) and for differential pumping between purification trap and measurement trap. In the purification trap a pressure of about 10^{-6} mbar is needed for the cooling process, while in the second trap (measurement trap) it should be below 10^{-8} mbar to ensure a high mass resolution. Currently, the channel has a diameter of 3 mm and a length of 50 mm, which results in a suppression factor of only 70. This limits the width of the resonances to bigger than 1 Hz (s. below). A new channel with a diameter of only 1.5 mm is presently being installed. Additionally, new designs of pumping barriers are investigated [Nei06]. The effective storing volume of the purification trap is larger than that of the measurement trap to enhance the injection efficiency.

The purification trap

The task of the first trap (purification trap) is to select and prepare for the later mass measurement only one nuclide from the mixture of different ion species

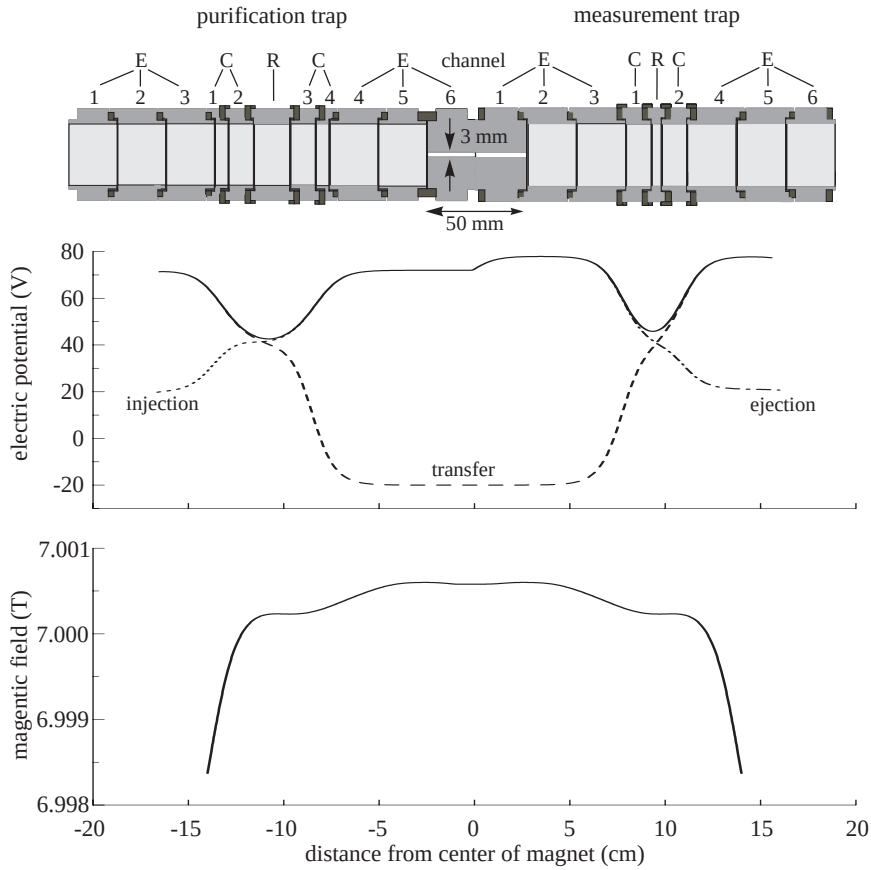

Figure 2.11: Layout of the two cylindrical Penning traps used for purification and mass measurement. Each trap consists of end-cap (E), correction (C) and ring electrodes (R). The plot in the middle shows the axial electric potentials for the closed traps (solid line) and while injecting ions into the purification trap (dotted line), while transferring them to the measurement trap (dashed line) and while ejecting them towards the detector (dotted-dashed line). The lower graph shows the axial magnetic field strength. Only the interesting field region inside the trap is enlarged to visualize the two homogeneous centers.

in the ion bunch. Since this is the first device that is really mass selective a separation method is mandatory that offers not only a high resolution but also a high sensitivity. The cleaning is accomplished by the mass-selective buffer-gas technique [Sav91]. A buffer gas, usually helium, is introduced to a pressure of few 10^{-6} mbar in the trap leading to a damping of the ion motions. While the amplitudes of the axial and the modified cyclotron motion get smaller, the one of the magnetron motion increases due to the collision processes. Without further measures the ions would be lost latest after some 100 ms depending on the gas pressure. To avoid this a quadrupolar RF field at the true cyclotron frequency of the ion of interest is applied, which leads to a coupling and an energy transfer from the magnetron to the modified cyclotron motion (s. above). Since the damping of the modified cyclotron motion is much faster due to the higher

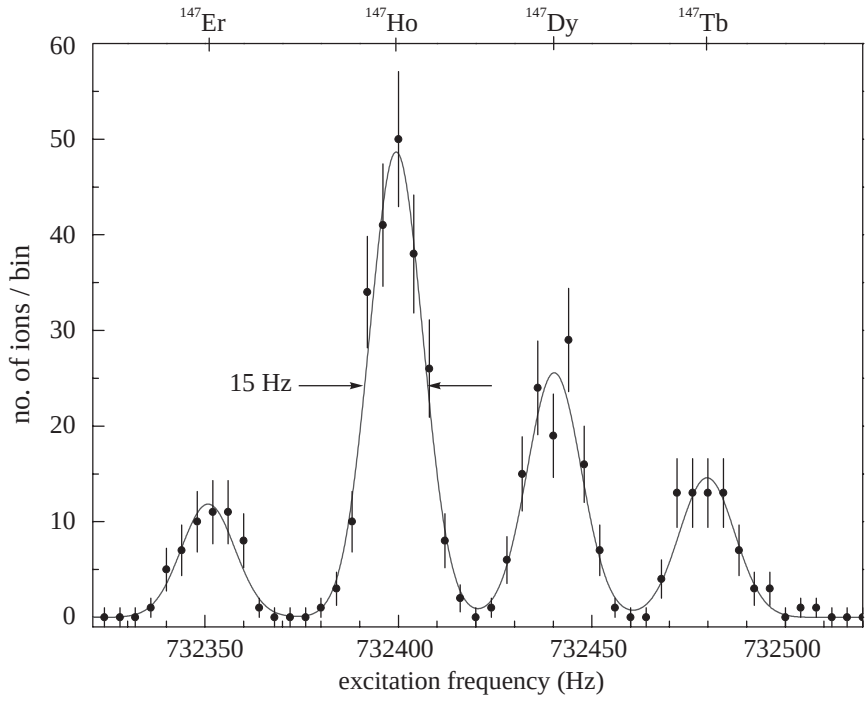

Figure 2.12: Cooling resonances in the purification trap for $A = 147$ isobars. With a mass resolving power of 50 000 all isobars can be separated from each other.

velocity, the magnetron amplitude is also reduced and the ions will accumulate in the center of the trap. This process is mass-dependent because only those ions are cooled for which the correct cyclotron frequency (2.5) is applied.

The cleaning process is usually performed in two steps. The injected ions are excited with a dipolar RF field at the magnetron frequency, which increases the magnetron orbit of all ions to 5 - 10 mm. The radius has to be chosen such that the ions can not fly through the small opening of the channel when transferred to the measurement trap. The second step is a quadrupolar excitation with a certain cyclotron frequency. As described above, this cools and centers only those ions whose mass-to-charge ratio corresponds to the applied cyclotron frequency. Only centered ions can pass the channel. Additionally to the cleaning, this centering process is also important for the subsequent mass determination in the measurement trap.

A scan of the applied cyclotron frequency (commonly called *cooling resonance*), as shown in fig. 2.12, gives a measure for the mass resolution of the purification trap and allows one to visualize the isobars in the ion sample. The mass resolution depends on the excitation amplitude but also on the gas pressure [Sav91]. A higher RF amplitude results in a broader resonance and a lower resolution. However, a lower amplitude needs a longer excitation time since the conversion process is slower. The usual voltages in the purification trap are given in tab. 2.4.

Table 2.4: Voltages of the end-cap, correction and ring electrodes of the purification trap (c.f. fig. 2.11). In brackets the values are given used for opening the trap for injection or transfer to the measurement trap.

electrode	voltage (V)
end-cap electrodes E 1/2/3	72 (20)
correction electrode C 1	66.3 (20)
correction electrode C 2	44.2
ring electrode R	40
correction electrode C 3	44.2
correction electrode C 4	66.3 (-20)
end-cap electrodes E 4/5/6	72 (-20)

The measurement trap

After cooling and preparation in the purification trap the potential between the traps is lowered (s. fig. 2.11) allowing the ions to drift into the measurement trap, where the precision mass determination is performed. Using eq. (2.5) this task is reduced to a measurement of the cyclotron frequency. At SHIPTRAP ν_c is obtained by means of the time-of-flight ion-cyclotron-resonance (TOF-ICR) method [Grä80]. It consists of two steps: First, the ions are excited with a dipolar RF field at the magnetron frequency to enhance their radial energy. This is necessary to increase the contrast (s. below) of the measurement. However, the excitation amplitude must not be chosen too high since this would lead to a decrease of the efficiency. Only a certain volume of the trap can be ion-optically imaged to the detector, ions with a too large radius are not detectable. Additionally, field inhomogeneities increase the farer the ions are out of the trap center, which result in a broader or shifted resonance. Second, the ions in the trap are excited by a quadrupolar RF field with frequencies close to the cyclotron frequency. This leads again to a coupling of the two radial motions and an energy transfer from the primary magnetron motion into the modified cyclotron motion. The strength of the coupling depends on how close the excitation frequency is to the cyclotron frequency.

The ions are ejected from the trap by lowering the voltage of the end-cap electrodes (s. tab. 2.5). They pass the strong magnetic field gradient until they hit the detector located outside of the magnet at a magnetic field of 50 mT. The magnetic moment of the ion

$$\mu = \frac{E_r}{B} \quad , \tag{2.7}$$

which depends on the radial energy E_r and the field strength B, interacts with the field gradient and leads to a force $F = \mu \cdot \nabla B$ that accelerates the ions in axial direction. In other words, the radial energy is converted into axial energy. To measure the cyclotron frequency the time of flight of the ions from the trap to the detector is measured as a function of the excitation frequency detuning. If the excitation frequency equals the cyclotron frequency the radial energy increase

Table 2.5: Voltages of the end-cap (E), correction (C) and ring (R) electrodes of the measurement trap. In brackets are the values when opening the trap for injection or ejection to detector.

electrode	voltage (V)
end-cap electrodes E 1/2/3	78 (-20)
correction electrode C 1	42
ring electrode R	35
correction electrode C 2	42
end-cap electrodes E 4/5/6	78 (21)

is maximal because of the strongest coupling. Due to the conversion process in the field gradient this leads to a maximal axial energy and to a minimal time of flight.

The result of a typical time-of-flight ion-cyclotron resonance (in the following simply called cyclotron resonance) is shown in fig. 2.13. The line shape is well understood and can analytically be reproduced [Kön95]. This allows one to perform a least-squares fit to the data extracting the measured cyclotron frequency. The sidebands of the resonance result from the finite excitation time that corresponds to a rectangular envelope of the RF signal. The achievable resolution

$$R = \nu_c/\Delta\nu_{\mathrm{FWHM}} \tag{2.8}$$

is determined by the width $\Delta\nu_{\mathrm{FWHM}} \propto 1/T_{\mathrm{RF}}$, which is inversely proportional to the excitation time T_{RF} of the RF signal [Bol01]. As indicated above, the residual gas pressure sets upper limits on the achievable width and thus on the resolution. The relative precision with which the cyclotron frequency can be determined is in first order proportional to the resolution and the number of ions N in the scan,

$$\frac{\delta\nu_c}{\nu_c} \propto \frac{1}{R\sqrt{N}} \quad . \tag{2.9}$$

The quality of the resonance, i.e. how well the time of flight of the resonant ions is separated from the one of the non-resonant ions, is described by the contrast. A detailed description of the definition and the optimization of the contrast is given in section 3.2.

2.3 The performance of SHIPTRAP

The efficiencies of the individual parts of SHIPTRAP as discussed in the previous sections were mostly determined from off-line measurements or simulations. The on-line measurements presented in chapter 4 can also deliver information about the current performance of SHIPTRAP. The detection of the isomeric state in ^{143}Dy shows that a resolution of better than 310 keV is presently achieved. For medium-heavy nuclides around $A = 100$ a typical resolving power

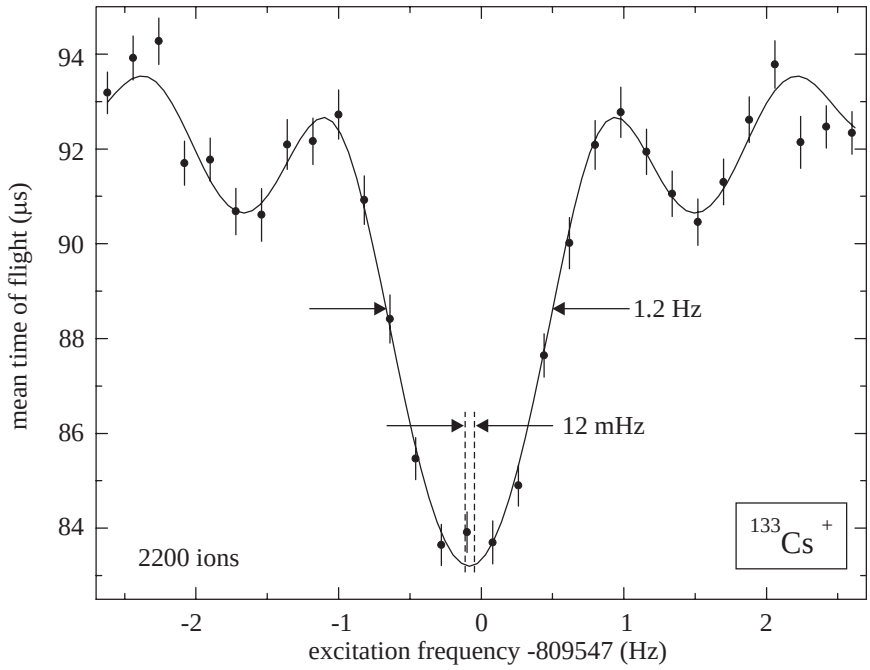

Figure 2.13: Cyclotron resonance of ^{133}Cs. The excitation time of 900 ms corresponds to a resonance width of 1.2 Hz, which determines the resolution to $6.7 \cdot 10^5$. The center frequency is obtained by a least-squares fit with a standard deviation of 12 mHz leading to a relative precision of $1.5 \cdot 10^{-8}$.

of $7 \cdot 10^5$ (c.f. fig. 2.13) would allow one to separate isomeric states with an excitation energy of about 100 keV.

^{147}Tm has with 700 ms the shortest half-life of the measured nuclides. With a typical measurement cycle time of about 1 s the short half-life did not yet set boundaries to the measurement. For nuclides with even shorter half-lives it would still be possible to shorten the excitation time in the purification and that in the measurement trap. This would, however, also result in a lower mass resolution. The lower limit of about 10 ms sets the diffusion time out of the gas cell.

Beside the short half-life ^{147}Tm has the smallest production cross section. It was determined by two different experiments to 100 μb [Sew97] and 200 μb [Kle82][2]. The known cross section allows one to estimate the total efficiency of the SHIPTRAP setup during the experiments. Assuming a SHIP transmission of 50 % [Maz06] and a cross section of 100 μb the overall efficiency ϵ_{tot} is calculated to $2(1) \cdot 10^{-4}$. The uncertainty lies in the determination of the primary beam current, which defines the number of projectile ions. The current was not recorded electronicly but on a plotter. The calibration and integration was done graphically with an assumed uncertainty of 50 %.

[2] In these experiments the cross section of the 15% p-decay branch [Tot93b] was measured to 16 μbarn and 30 μbarn, respectively.

Table 2.6: Individual efficiencies of the SHIPTRAP components during the on-line experiments in December and October 2005.

efficiency	value	source of information
ϵ_{stop}	30 %	SRIM simulation
ϵ_{extr}	3 %	measured
ϵ_{bunch}	50 %	measured
ϵ_{trans}	50 %	measured
ϵ_{traps}	50 %	measured
ϵ_{det}	30 %	measured
ϵ_{tot}	$3 \cdot 10^{-4}$	calculated acc. to eq. (2.10)

The result of the efficiency determination can be reproduced by factorizing the total efficiency into its individual parts,

$$\epsilon_{\text{tot}} = \epsilon_{\text{stop}} \cdot \epsilon_{\text{extr}} \cdot \epsilon_{\text{bunch}} \cdot \epsilon_{\text{trans}} \cdot \epsilon_{\text{traps}} \cdot \epsilon_{\text{det}} \quad , \tag{2.10}$$

which are the stopping ϵ_{stop} and extraction efficiency ϵ_{extr} in the gas cell, the efficiencies of the buncher ϵ_{bunch}, of the transfer section ϵ_{trans} and of both Penning traps ϵ_{traps} including all separation and measurement processes. Finally, the detection efficiency ϵ_{det} is included. Table 2.6 lists all estimated and measured efficiencies. While ϵ_{extr}, ϵ_{bunch} and ϵ_{det} were measured and are reliable numbers, ϵ_{stop} is the major unknown magnitude since all present numbers stem from SRIM simulations (c.f. section 3.1). The transfer and trap efficiencies are usually close to 100 %. They were optimized using the radioactive ^{219}Rn ions from a off-line source in the gas cell (s. section 2.2.1). During the beamtime, however, they were not reoptimized for the much lighter reaction products, which caused the efficiency loss.

2.4 The measurement procedure

The radioactive ions from SHIP leave the gas cell as a quasi-DC beam and are accumulated in the RFQ buncher. After cooling, the ions are ejected as a bunch out of the RFQ buncher. Special care has to be taken upon the correct opening and closing times of the traps. These have to match the ion's time of flight, which is determined by their mass-to-charge ratio and the applied electric fields.

Figure 2.14 shows the complete timing sequence of SHIPTRAP. The ions accumulated in the buncher are ejected at a certain time that defines the start of the cycle. Alternatively, ions from one of the ion sources can be injected into the traps for magnetic-field calibration or tests of the setup. After waiting for about 70 μs the purification trap is opened for 40 μs by lowering the front end-cap and correction electrode voltages (c.f. fig. 2.11). This capture waiting time is a very sensitive parameter since a change of only few μs can cause the

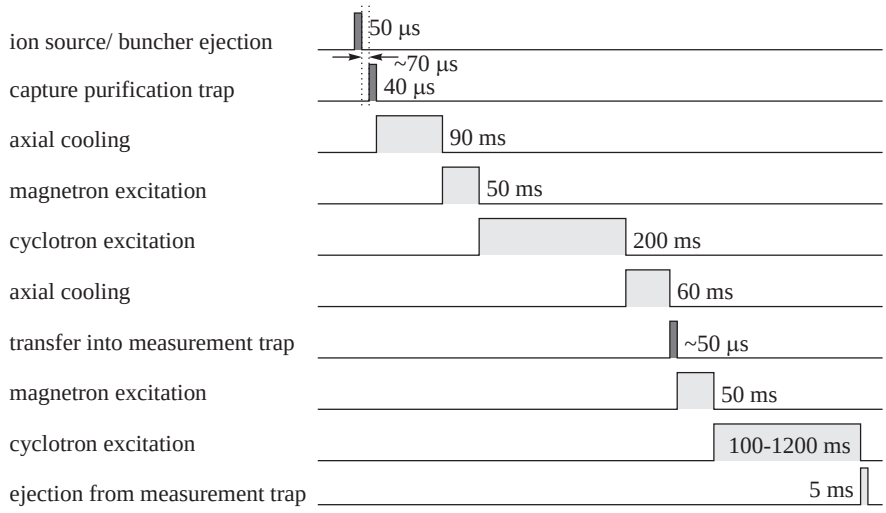

Figure 2.14: Timing sequence of a measurement. The dark gray pulses are not to scale but enlarged for better visibility. Times marked with ∼ are dependent on the ions mass-to-charge ratio and have to be adapted to each new ion species.

ions to be lost. The correct value depends not only on the starting point of the ions (buncher or ion source) but also on the voltages in the transfer section and the ion's mass-over-charge ratio.

The ions remain in the purification trap for usually 400 ms, which includes the waiting time for axial cooling, the magnetron and cyclotron excitation and finally another waiting period for further axial and radial cooling. After that, they are transferred into the measurement trap by lowering potential of the end-cap electrodes E 4/5/6 of the purification trap and E 1/2/3 of the measurement trap (c.f. fig. 2.11). The timing of the switching of the potentials is again very critical and has to be optimized for maximal efficiency. Additionally to the loss of the ions, an incorrect transfer time can also lead to an axial excitation of the ions in the measurement trap. If the ions are not captured in the center of the trap they will gain axial energy when ramping up the potential of the end-cap electrodes for closing the trap. This energy increase has to be avoided since it reduces the contrast and limits the achievable precision of the measurement.

In the measurement trap the ions are again excited by dipolar RF fields at the magnetron frequency followed by a quadrupolar one with a frequency close to the expected cyclotron frequency. The excitation time of the quadrupolar signal is chosen between 100 ms and 1200 ms depending on the half-life of the isotope under investigation and the wanted resolution. A further increase of the excitation time is at the moment not reasonable at SHIPTRAP since the narrowest width of the resonances is around 1 Hz due to broadening by collision with residual gas atoms. The helium pressure in the measurement trap is calculated to be about $1 \cdot 10^{-8}$ mbar. A reduction of the channel diameter from 3 mm to 1.5 mm, which is presently performed, would reduce the residual gas pressure in the measurement trap by a factor of about ten and allow for even

longer excitation times for higher-precision measurements. The last step is the ejection of the ions by lowering the end-cap electrodes E 4/5/6 of the measurement trap (c.f. fig. 2.11). This pulse is also the start signal for the time-of-flight measurement. The stop pulse is produced by the arrival of the ion at the MCP detector.

The sequence described above is called a cycle. After one ion bunch ran through this cycle the quadrupolar excitation frequency in the measurement trap is changed and another cycle begins. A typical measurement consists of 41 different cycles with frequencies around the expected cyclotron frequency. After finishing 41 cycles, which is called one scan, the process starts from the beginning in order to improve the statistics. Several scans are accumulated until the number of ions is sufficient for the precision aimed at.

From the obtained resonance curve the cyclotron frequency is extracted. Using eq. (2.5) the mass of the ion can be calculated if B and q are known. While the charge state is usually only one or two, the direct measurement of the magnetic field strength with the needed precision is not possible. To calibrate B the cyclotron frequency ν_{ref} of a reference ion with a well-known mass m_{ref} is measured. For this the quadrupole deflector voltages are changed to inject ions from the reference ion source (surface ion source, fig. 2.4) and the waiting and transfer timings (s. above) are scaled to match the new mass-over-charge ratio. Usually, the reference measurement is performed once before and after the measurement of the ion of interest or at least every hour to reduce systematic uncertainties arising from magnetic field fluctuations (s. section 3.3). The result of the measurement is finally a frequency ratio $r = \nu_{ref}/\nu_c$. The precision with which ν_{ref} is determined has to be better than the one of ν_c to prevent an additional increase in the uncertainty of r.

From the frequency ratio the mass of the atomic nuclide can be calculated as

$$m = \frac{z}{z_{ref}} r \left(m_{ref} - z_{ref} m_e\right) + z\, m_e \quad , \tag{2.11}$$

where z and z_{ref} are the charge states of the ion of interest and the reference ion and m_e is the electron mass. The binding energies of some eV for the outer electrons can be neglected for a mass uncertainty above 1 keV. A detailed description of the analysis procedure is given in section 4.2.

2.5 The control system

The SHIPTRAP facility is run and supervised by a program called CS [Bec04], which is a dedicated control system framework based on the programming language LabVIEW by National Instruments. It has been specially developed to match the demands of a medium-size experiment such as SHIPTRAP. LabVIEW was chosen since this language is easy to learn and the programs are modular and quickly understood. This is an important argument for those experiments that are supervised and maintained by students, whose typical working period is usually not longer than three years. New students can quickly understand

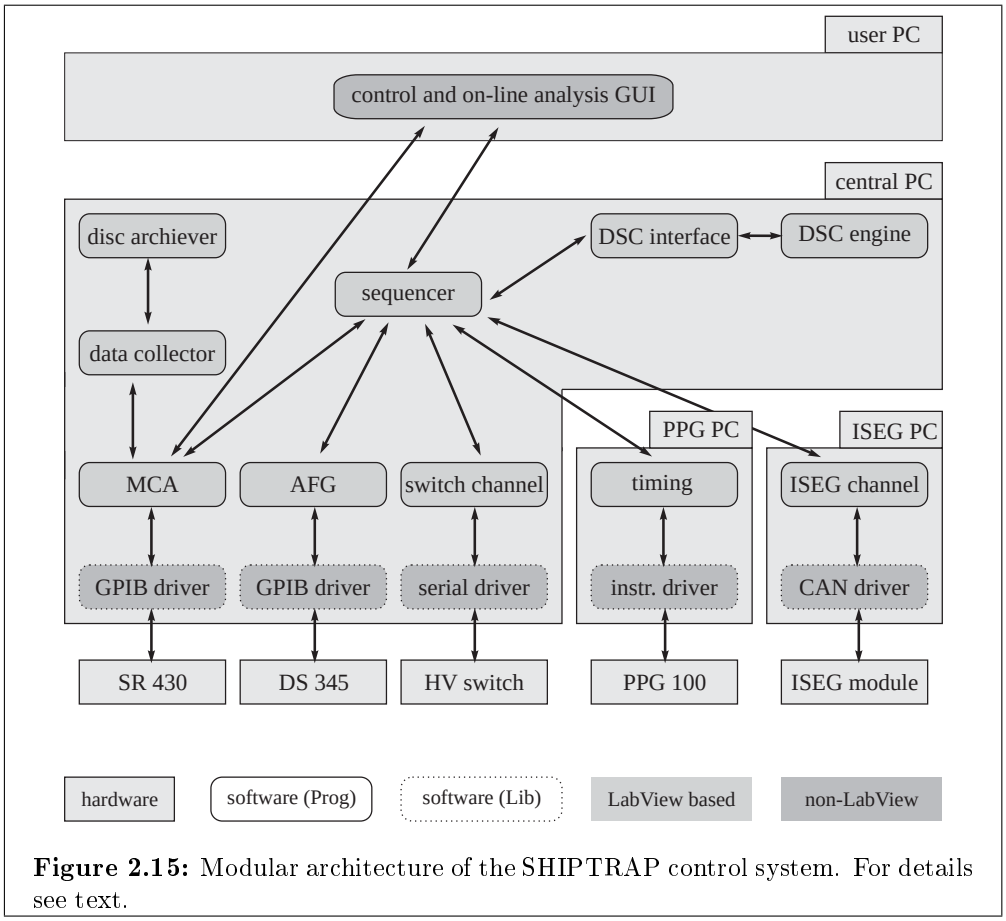

Figure 2.15: Modular architecture of the SHIPTRAP control system. For details see text.

the existing parts and after a relatively short learning time start to implement new components. Within this work CS was adapted, maintained and advanced at SHIPTRAP. Several new classes were implemented or tested. Furthermore, a new real-time CS system for vacuum control was set up and tested (s. below).

The basis of CS is an object-oriented, multi-threaded and event-driven framework, which is now used by several other experiments and facilities. The task of the individual user is to adapt this framework to their needs by adding few specific classes to instantiate experiment specific objects from.

Figure 2.15 shows the simplified architecture of the CS used at SHIPTRAP. The whole experiment is usually controlled by four PCs. While three of them (central, PPG and ISEG PC) are located directly at the setup and act as interfaces to the individual devices, the fourth (user) PC may be any ordinary PC. Here, the C++ control GUI is running, which is the main interface to the experiment. It allows one to set the parameters of the scans, to start and stop the scans and also to visualize the results on-line.

The control GUI talks via TCP/IP with the *sequencer* situated on the central PC. This object is not only the interface between the C++ GUI and the LabVIEW CS but can be seen as the 'brain' of the program. It understands the commands coming from the GUI and distributes them to the addressed

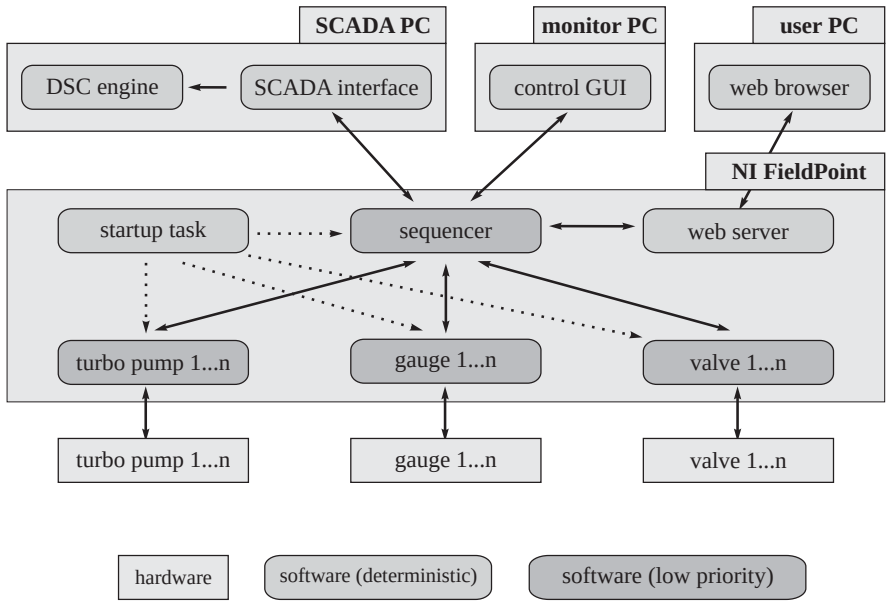

Figure 2.16: Architecture of the real-time vacuum safety system implemented on a National Intruments FieldPoint RT device. For details see text.

devices. Furthermore, the *sequencer* executes all necessary actions when for example a scan has to be started. The realization of the measurement sequence as described in section 2.4 is implemented here.

On the device layer each channel of every device is represented by an individual object. These objects act as interfaces to the device drivers that communicate over different bus types with the devices. The main components are shown in the lower part of fig. 2.15. On the central PC a GPIB interface talks with the frequency generators (Stanford Research DS 345) and the data acquisition device, a multi channel scaler (MCS) for the time-of-flight measurement (Stanford Research SR 430). Via a RS 485 interface 16 fast high voltage switches are controlled, which are used for switching the trap electrodes for opening and closing of the traps. The PPG PC includes a 10 MHz pulse pattern generator (PPG) card, which creates the timing sequences described in the last section (s. fig. 2.14). Finally, the ISEG PC communicates via CAN bus with two ISEG crates, where all static DC voltages are controlled.

The data from the MCS are collected by the *data collector*, which distributes them to the control GUI for on-line visualization and analysis or to the *disc archiver* that writes them on a hard disc. Additionally, all important parameters are monitored and logged with a supervisory-control and data-acquisition (SCADA) system. The LabVIEW internal data-logging and supervisory-control (DSC) module is used for this purpose.

The CS is designed for slow controls and, as it runs on ordinary PCs, is not deterministic. However, for some purposes (data acquisition or safety systems) a time-critical deterministic processing is mandatory. Within this work the CS framework was for the first time implemented on a real-time system [Bec06]. It

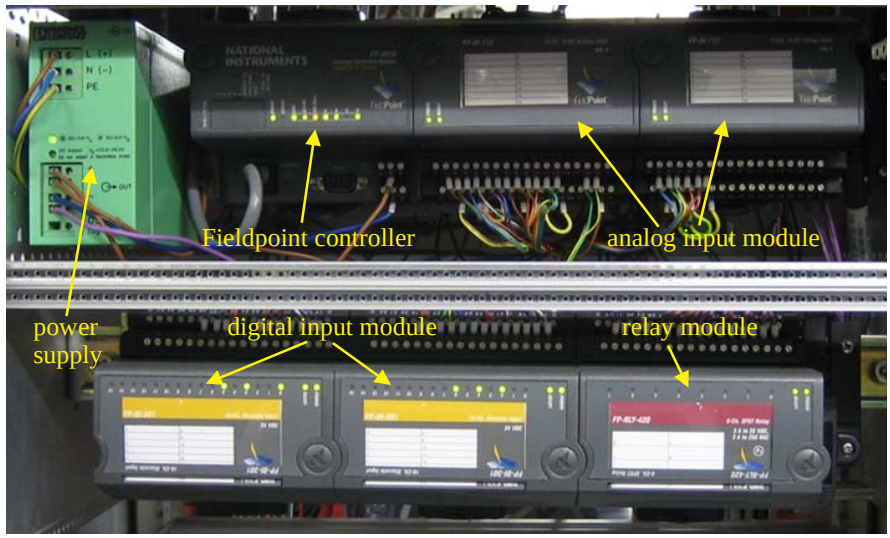

Figure 2.17: Photograph of the National Instruments Fieldpoint setup. The green power supply delivers the 24 V DC working voltage. The connection to the Fieldpoint controller (FP-2010), in which the realtime CPU is located, is accomplished via TCP/IP. The analog input modules (AI-112) are used to read the pressure measured by different gauges, while the digital input modules (DI-301) determine the status of the turbo pumps. Supervised by the security program running in the controller the relay modules (RLY-420) allow one to switch gate and pre-vacuum valves.

was designed for the vacuum safety control of SHIPTRAP and implemented on a National Instruments Fieldpoint RT device programed with LabVIEW RT. Figure 2.17 shows a photograph of Fieldpoint controller and the used modules. The main task is to supervise the pressure as well as the functional of different turbo molecular and roughing pumps. If an error occurs, the system has to react by quickly closing the appropriate gate or pre-vacuum valves.

The simplified architecture of the CS real-time system is shown in fig. 2.16. The center of the system is again the *sequencer* that runs in a time-critical loop and contains the complete logic. A big difference compared to the PC system is that the communication with the external devices is no longer accomplished by complicated bus systems but by fast digital and analog in- and output channels. The communication and the *sequencer* are the only tasks that run with high priority. All other processes have low priority and run non-deterministicly.

A *startup task* starts all other objects and the *sequencer* independently to ensure continuous running after a power cut. The control and monitoring can be accomplished by different methods. A web server is implemented in every NI Fieldpoint allowing to publish the actual performance and monitor it with any web browser. For control purposes like the manual opening or closing of valves a dedicated GUI communicates with the *sequencer* via TCP/IP. Finally the *sequencer* publishes via TCP/IP important data and parameters to a special CS-SCADA object, which is located on an ordinary PC. This object sends the data to a SCADA backend like the DSC engine (s. above).

Chapter 3

Off-line investigations

On-line measurements with radioactive ions require high efficiency and resolution of the experimental setup. The more exotic the nuclide the lower the production cross section and the higher the efficiency has to be to perform a measurement in a reasonable time.

The optimization starts already before an on-line experiment by choosing the appropriate window material and thickness. To ensure efficient stopping in the gas cell both have to be adapted to the energy of the ions, which is mainly defined by the mass ratio of the selected fusion-evaporation reactant and the primary beam energy. The following section 3.1 concentrates on this topic and describes investigations of the thickness and the roughness of different window foils.

During the on-line experiment the optimizing procedure starts with tuning the parameters of the gas cell. Monitoring the count rate at MCP 1 (c.f. fig. 2.8) the gas pressure and the different RF and DC voltages are tuned. While the cage voltages and funnel RF amplitudes (c.f. fig. 2.5) are chosen as high as possible without causing discharges, the voltages of the nozzle and the last funnel electrode have to be carefully adjusted to the gas flow (s. section 2.2.1). The extraction RFQ and buncher are usually not retuned for a new ion species. Only if a high contamination occurs, which can not be separated in the purification trap, an additional 'dipole cleaning' is performed as described in section 2.2.2. Switching to MCP 2 and later to MCP 3 the transfer and injection into the magnet is optimized. After applying the trap electrode potentials the capture waiting time of the purification trap and later the transfer time to the measurement trap are fine-tuned (s. section 2.4). Storing the ions in the purification trap the optimal excitation settings for the mass-selective buffer gas cleaning are determined by scans of the magnetron and cyclotron amplitudes and frequencies. Finally, in the measurement trap the excitation and ejection parameters are optimized to achieve an optimal conversion and maximize the contrast. The latter issue is addressed in detail in section 3.2.

The last section of this chapter reports about studies to investigate uncertainties in the determination of the frequency ratio, which arise from magnetic-field instabilities.

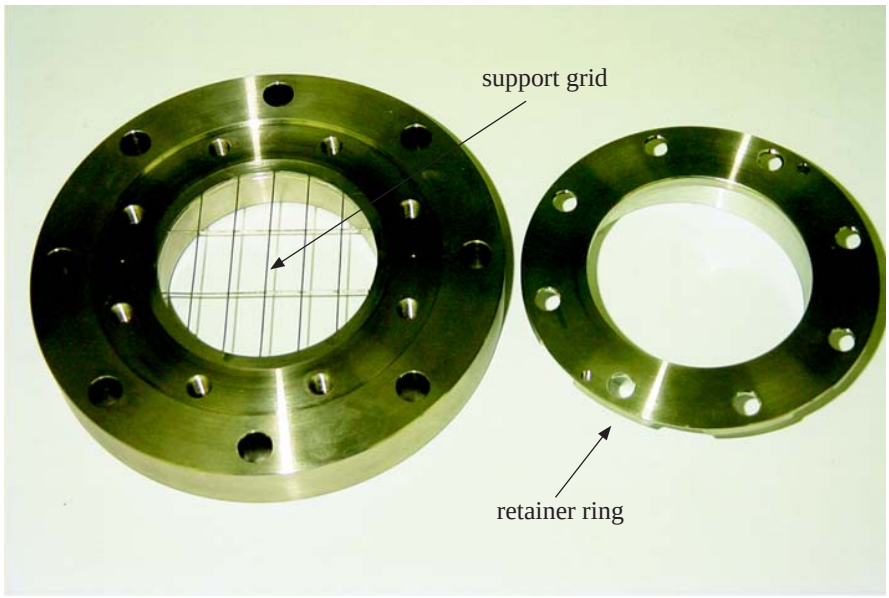

Figure 3.1: Photograph of the gas cell window flange and its retainer ring. Thin metal wires support the window foil enabling it to withstand higher pressure differences.

3.1 Investigations of the window foils

The gas cell forms in many respects the most sensitive part of the SHIPTRAP setup. It has the lowest efficiency of all parts and many parameters have to be retuned carefully for every new experiment. Looking for example at the stopping efficiency the window foil thickness and the gas pressure have to be chosen very precisely to match the energy and energy spread of the radioactive ion beam (s. section 2.1).

3.1.1 Dependence of the stopping efficiency on the window thickness

The gas cell window is used for two purposes. First, it separates the high pressure region in the gas cell (typically 40 - 60 mbar) from the vacuum in the SHIP beamline (typically $1 \cdot 10^{-6}$ mbar). Second, it acts as final energy degrader for the high-energetic reaction products. Finding the right thickness to fulfill both tasks is not trivial. The stopping range for a fixed ion energy is defined by the gas pressure and the window thickness. The gas pressure determines mainly the width of the distribution, while the thickness defines the location of the center. For a smaller distribution a higher gas pressure is necessary, which demands a thinner window to keep the stopping volume in the middle of the cell. However, for the higher pressure one would need a thicker window foil to stand the pressure difference.

In practice, the availability of pinhole-free foils set additional boundaries on the thickness. The window should be also ultra-high vacuum compatible and

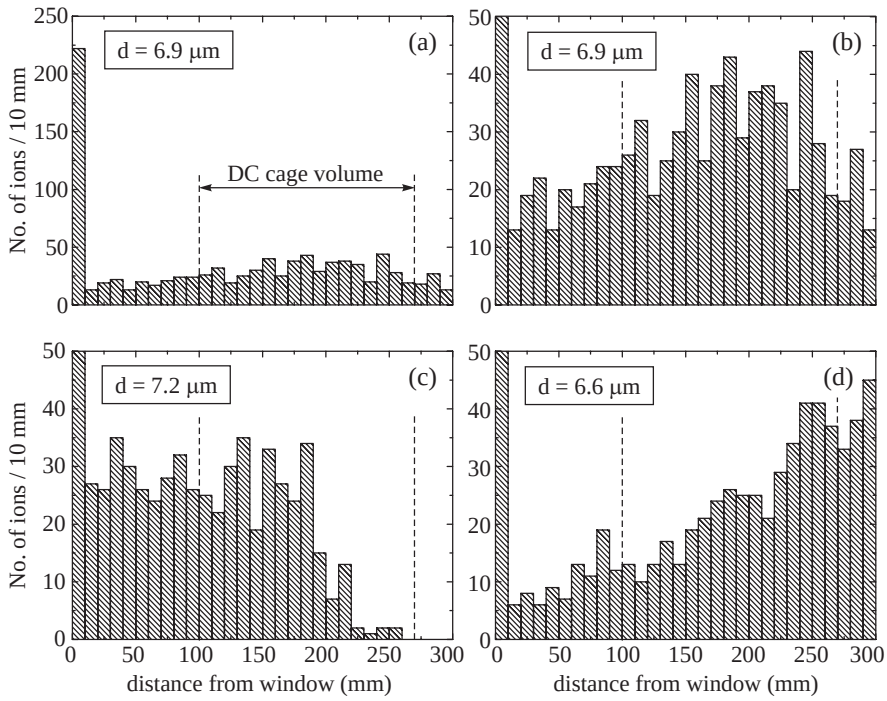

Figure 3.2: The stopping distribution of 77 Mev ^{146}Er ions in the gas cell with a titanium window of indicated thickness and a helium gas pressure of 50 mbar. The distributions was simulated using the SRIM code. The y-axis shows the number of ions stopped in a range of 10 mm. In each example 1000 ions were simulated. The dashed lines indicate the boundaries of the DC cage (c.f. fig. 2.5), which are used for the stopping efficiency calculation. The first bin contains the stopping effect of the titanium foil. For the optimal thickness of 6.9 μm 20 % of the ions are stopped in the foil (a). To visualize the stopping distribution, graph (b) shows the same simulation with an enlarged y-axes. The stopping distributions for a 0.3 μm thiner and thicker window are plotted in graphs (c) and (d).

allow for baking. Typical materials that fulfill theses conditions are light metals like aluminum and titanium. To obtain the desired thickness the target lab at GSI reduces the thickness of a commercially available foil with a plate roll. By weighing and measuring the area of the foil they specify its thickness with a precision of 10 %. To enable the window to withstand even higher pressure differences the window foil is supported by a wire grid when mounted into the window flange (s. fig. 3.1).

How sensitive the stopping distribution depends on the window foil thickness can be seen in fig. 3.2. Using the code SRIM [Bie80, Zie06] the stopping in the gas cell was simulated for ^{146}Er ions with a fixed energy of 77 MeV and a titanium window with three different thicknesses in steps of 0.3 μm. The gas pressure in the cell was set to 50 mbar. Graph (a) shows the result for the optimal thickness of 6.9 μm. 20 % of the ions are stopped already in the window foil itself, while the rest of them are distributed broadly over the full diameter (30 cm) of the gas cell. The graphs (b) to (d) visualize the shift in the stopping distribution with

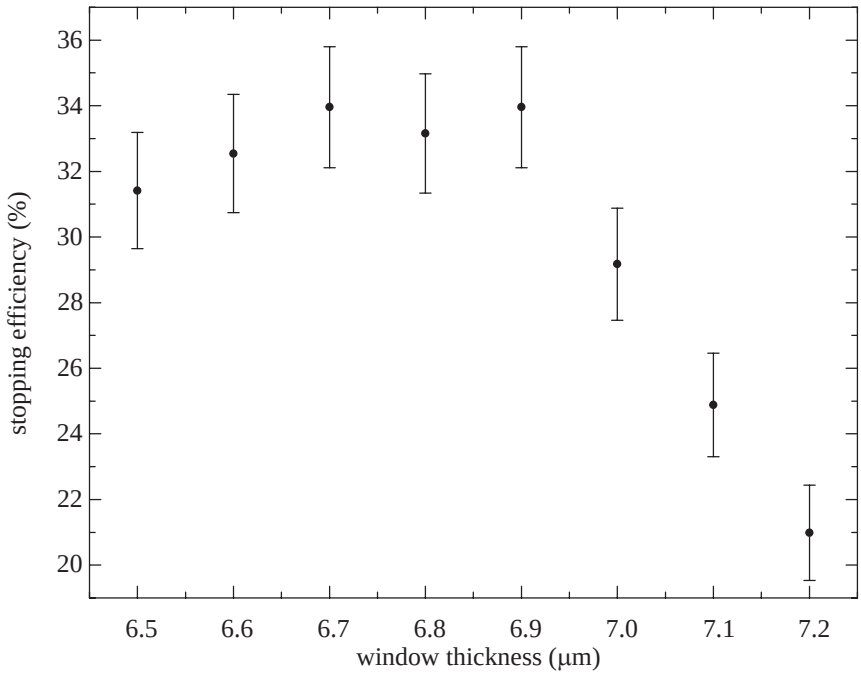

Figure 3.3: Stopping efficiency as a function of the thickness of the titanium window thickness resulting from the SRIM calculations. The pressure in the gas cell was 50 mbar. The stopping volume is defined by the volume of the DC cage (c.f. fig. 3.2.

changed window thickness. Increasing (c) or decreasing (d) the thickness by only 0.3 μm compared to the optimal thickness (b) drastically shifts the maximum of the distribution.

Figure 3.2 shows the distribution only for a certain energy of reaction products. In reality, the ions have an energy distribution depending on the place of their production in the target foil (s. section 2.1). Due to the energy they loose while traveling through the target material the ions have a lower energy when produced at the front of the foil and a higher one when produced at the end. In this example the energy ranges from 65 MeV to 83 MeV. Although the production cross section is generally energy dependent it is almost constant in this small range. Hence, the energy distribution can be assumed as of rectangular shape.

For seven distinct energies between 65 MeV and 83 MeV the simulation was performed for different window thicknesses and a helium pressure of 50 mbar. To calculate the stopping efficiency all ions stopped in a volume defined by the DC cage boundaries (c.f. fig. 3.2) were divided by the total number of ions (1000). All results for one thickness were averaged. The final result of the simulation is shown in fig. 3.3. The stopping efficiency reaches a maximum of 33 % and is relatively constant around the center value of 6.8 μm. The variation of stopping efficiency as a function of energy can be explained by looking at fig. 3.2: While for a thin window (d) the distribution has due to the longer tail still a significant number of stopped ions in the DC cage volume, in the simulation with the thick

window (c) the distribution falls relatively sharp at the center of the cage. For this reason one would choose the window thickness rather too thin as too thick, especially since additional energy degraders can still be introduced in the SHIP beamline in front of the gas cell.

3.1.2 Measurement of the window foil thickness

The simulations presented in the previous section show that a high stopping efficiency requires foils of precisely defined and known thicknesses, which have, in addition, to be uniform within ±10 %. Whithin the GSI summerstudent program 2006 measurements were performed to reproduce the thicknesses of four window foils as specified by the target lab (s. above) and to investigate the roughness of these foils.

The thickness of a thin metal foil can be determined by measuring the energy loss of an ion when penetrating through the foil. The energy loss per path unit of a charged particle in solid matter is described by the relativistic Bethe-Bloch formula

$$\frac{dE}{dx} = -\frac{4\pi n z^2 e^4}{m_e \beta^2 c^2}\left[\ln\frac{\gamma^2 m_e \beta^2 c^2}{I(1-\beta^2)} - \beta^2\right] \quad , \tag{3.1}$$

where m_e and n are the electron mass and density in the target material, z the charge state and $\beta = v/c$ and $\gamma = (1-\beta^2)^{-1/2}$ the relativistic velocity and Lorentz factor of the projectile. I is the mean ionization potential of the target atoms. Integrating eq. (3.1) over the foil thickness allows one to calculate the energy loss of a charged particle after penetrating a foil of a given thickness. Vice versa the thickness of the foil can be determined when knowing the energy

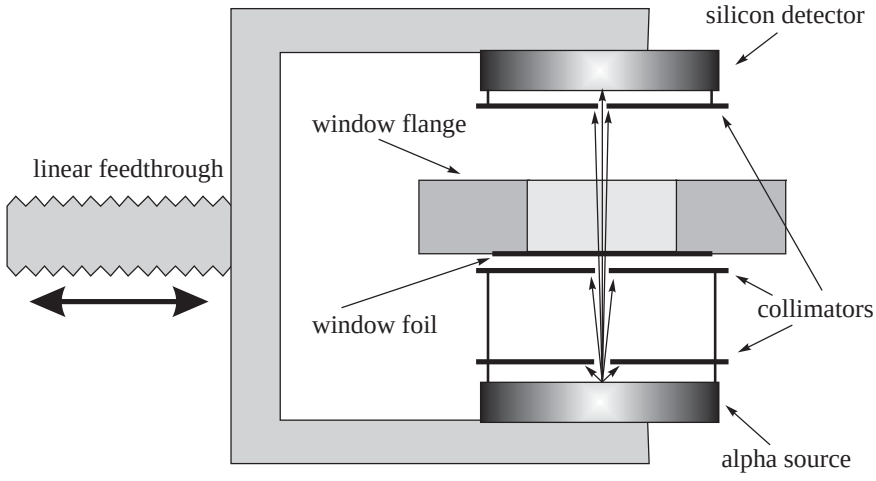

Figure 3.4: Schematic drawing of the test bench setup. An α source is mounted opposite of a silicon detector. The window flange can be moved in and out to measure the energy difference. Additionally the source and detector frame can be moved by a linear feedthrough enabling a spatial scanning of the foil. Three collimators are used to obtain a good spatial resolution.

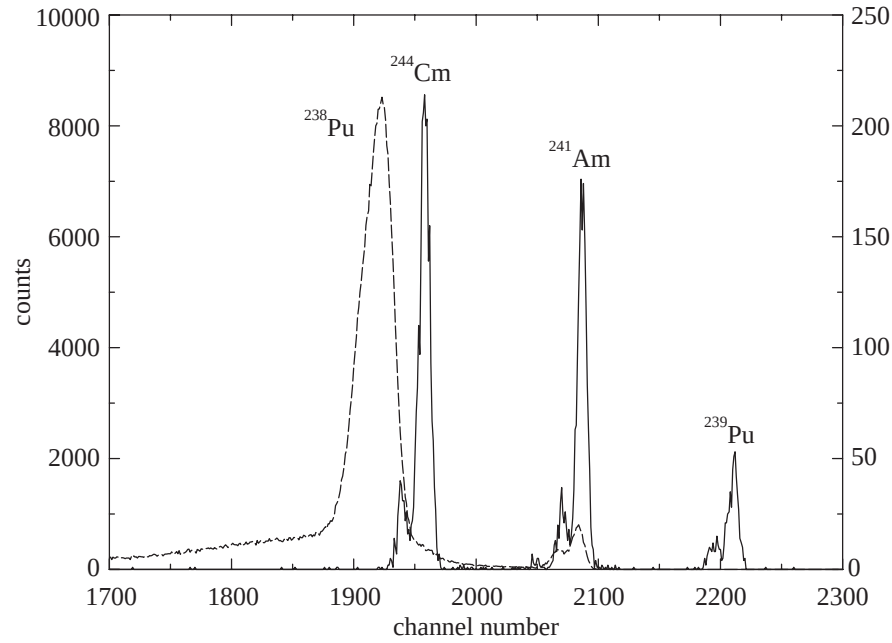

Figure 3.5: Energy spectrum of the two α sources used to determine the thickness of the gas cell window foils. For the thickness measurement the high-activity (30 MBq) ^{238}Pu source (dashed line, left y-axis) was used, which was calibrated with a 10 kBq α source consisting of a mixture of ^{239}Pu, ^{242}Am and ^{244}Cm (solid line, right y-axis).

loss. Modern codes are based on this formula but also take the more complicated electron structure of the foil material into account. The code used in the following is called ATIMA and was developed at GSI [Sch98b, Wei06].

To measure the energy loss a dedicated vacuum chamber was set up, which is schematically shown in fig. 3.4. The window foil mounted on a window flange is brought to a fixed position in this chamber. On a U-formed holder a radioactive α source and a silicon detector are mounted. The whole unit can be moved by a linear feedthrough to measure the window thickness at different positions. Three collimators with holes of 1 mm diameter are used to enable a spatial resolution in the order of 1 mm and prevent one from measuring scattered α particles, which decrease the energy resolution of the measurement. The whole assembly is situated in a vacuum chamber that is pumped by a roughing pump to pressures below 1 mbar. The readout of the silicon detector was done with a conventional ADC connected to a PC.

Two different α sources were used during the measurement. For the thickness measurement a high-activity (30 MBq) ^{238}Pu source was taken. However, for safety reason this source is covered with a 5 μm thin nickel layer, which shifts and broadens the α line and makes the energy calibration difficult. For this purpose a weaker (10 kBq) but uncovered α source containing a mixture of ^{239}Pu, ^{242}Am and ^{244}Cm was used (s. tab. 3.1). Both energy spectra are shown in fig. 3.5.

Table 3.1: Half-lives $T_{1/2}$ and α energies E_α of the nuclides used for energy calibration [Pfe98]. Only the α energies of the two most intense α decays are given.

nuclide	E_{α_1} (MeV)	E_{α_1} (MeV)	$T_{1/2}$
^{239}Pu	5.175	5.144	2000 a
^{242}Am	5.486	5.433	432.2 a
^{244}Cm	5.805	5.762	18.0 a

To measure the foil thickness the α spectrum is recorded with and without foil. Figure 3.6 shows as an example a measurement of a titanium foil with a thickness of 2.3 μm as specified by the target lab. A Gauss fit is used to determine the centers of the peaks. From the corresponding energies the thickness is calculated with ATIMA. The dominating uncertainty arises in the calibration process. As shown in fig. 3.5 the α energy of ^{238}Pu is lower than the ones of the three calibrants. Therefore the calibration has to be extrapolated to the energy region of the measurement, which results in an average uncertainty of 25 keV.

The thickness was measured for four foils, one made from aluminum and three from titanium. Each foil was scanned in steps of 1 mm by moving the source-detector assembly with the linear feedthrough. The results of two measurements are shown in fig. 3.7. One recognizes in the two graphs a significant scattering around the mean value in the order of $\pm 1.5\,\%$. From all thickness measurements of one foil the weighted average was calculated to obtain a mean

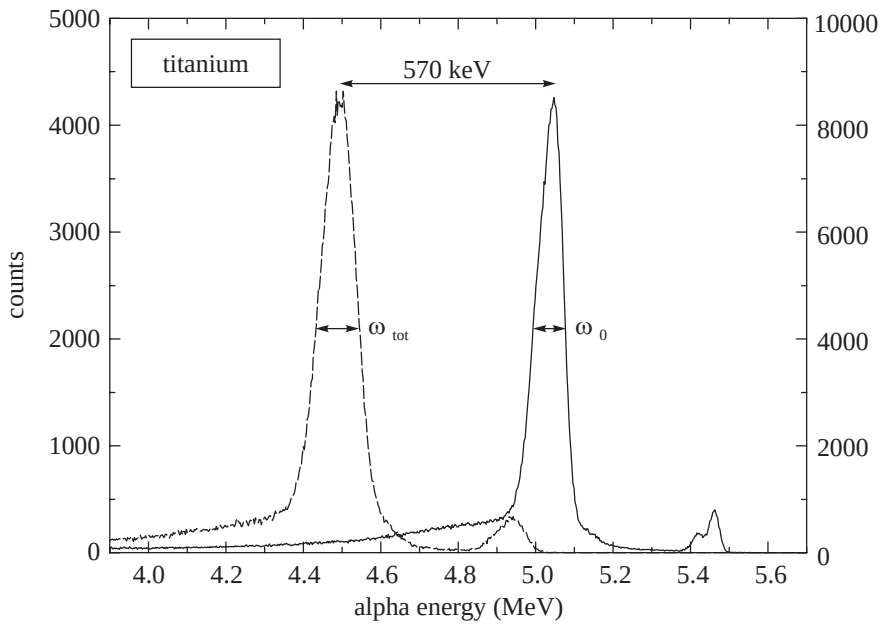

Figure 3.6: Energy spectrum with (dashed line, left y-axis) and without (solid line, right y-axis) a 2.3 μm thin titanium foil. The width of the two peaks (ω_0 and ω_{tot}) are used to estimate the roughness of the foil (s. section 3.1.3).

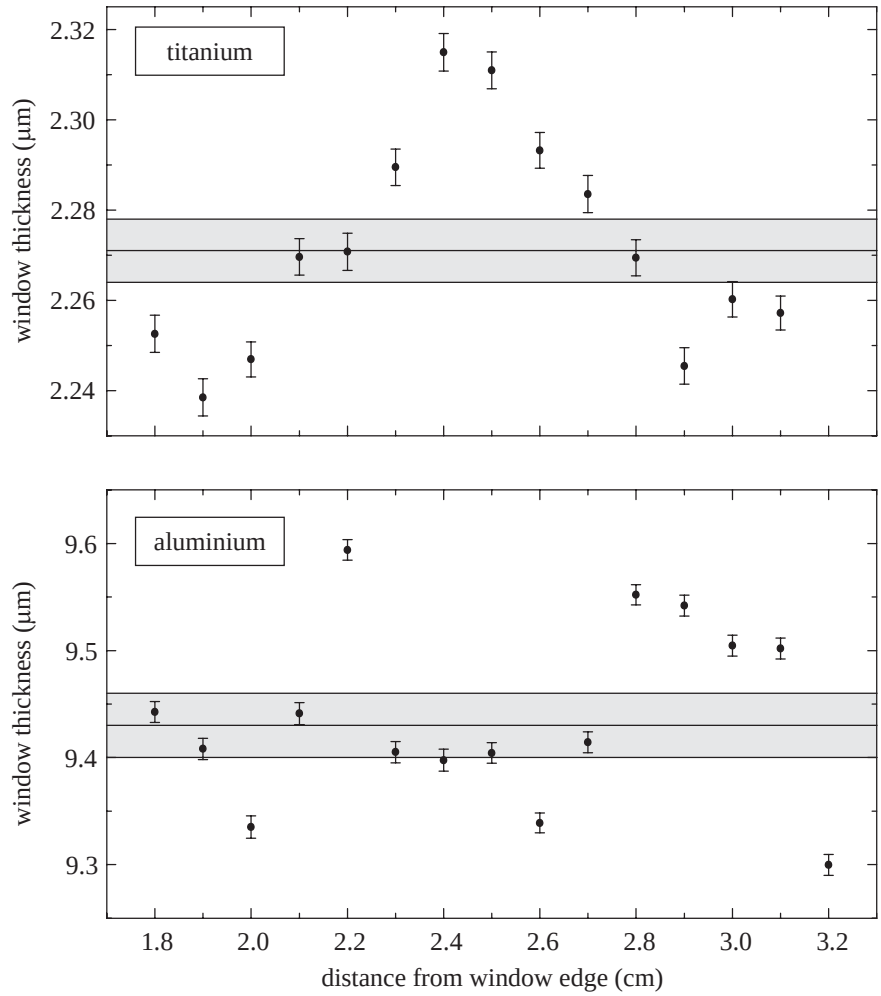

Figure 3.7: Thickness of two window foils for different foil positions determined by measuring the energy loss of α particles. The line shows the mean thicknesses of 2.271(7) μm and 9.43(3) μm, respectively, which reproduce well the target lab specification of 2.3(2) μm and 9.3(9) μm. However, the variations of the foil thickness range from 2 % to 10 % (s. below).

thickness. The results are summarized in tab. 3.2 and show good agreement compared to the values specified by the target lab.

3.1.3 Estimate of the foil roughness

The spatial resolution during the thickness measurement was around 1 mm, due to the 1 mm diameter of collimators. If the variations of the thickness are on a scale below that the measurement will not resolve the true variations and the result of ± 1.5 % is only an average value. A different way to estimate an upper limit for the roughness of the window foil is to measure the broadening of the α peak in the energy spectrum (s. fig. 3.6). The following points can affect the width of an α line:

Table 3.2: Results of the foil investigations. Listed are the measured mean thicknesses d_{meas} compared to the ones d_{spec} specified by the target lab. $\omega_0 = 79(1)\,\text{keV}$ is the linewidth without energy straggling. ω_0' is the linewidth resulting from energy loss and straggling in the different foils calculated with ATIMA. The total width ω_{tot} is determined from a Gauss fit to the measured alpha line (c.f. fig. 3.6). The broadening of the α line due to roughness of the window foil ω_{rough} are calculated according to eq. (3.2). R_{max} is the upper limit for the roughness of the window foils extracted from the broadening of the α peak.

foil number	1	2	3	4
material	Ti	Ti	Ti	Al
d_{spec}	2.3(2) μm	3.3(3) μm	7.1(7) μm	9.3(9) μm
d_{meas}	2.271(7) μm	3.1(4) μm	7.0(3) μm	9.43(3) μm
ω_0'	85(2) keV	90(3) keV	109(3) keV	105(2) keV
ω_{tot}	119(1) keV	116(2) keV	235(5) keV	231(2) keV
ω_{rough}	83(3) keV	73(7) keV	208(7) keV	206(3) keV
R_{max}	$\pm$14.6(6) %	$\pm$9.9(9) %	$\pm$9.6(3) %	$\pm$10.4(2) %

- the resolution of the detector, the amplifiers and the readout electronics,
- scattering of α particles on walls and other surfaces,
- energy straggling when penetrating a thin foil,
- variations of target foil thickness.

The first point defines the linewidth ω_0 of the measurement that is determined by the used detector and electronics. The scattering of α particles can be avoided by using collimators. Additionally blade-shaped edges help to prevent scattering on the collimator walls. The energy straggling in the foil can not be avoided and broadens the line to ω_0'. However, the mechanism is theoretically well-understood and included in the ATIMA code thus allowing to calculate its magnitude. The variations of the target foil thickness, which is the effect this investigation aims at, additionally broadens the α line by ω_{rough}.

If one assumes the α line to follow a Gaussian distribution, the total width ω_{tot} is simply the quadratic sum of the individual ones

$$\omega_{tot} = \sqrt{\omega_{rough}^2 + \omega_0'^2} \quad . \tag{3.2}$$

The linewidth[1] without energy straggling, $\omega_0 = 79(1)\,\text{keV}$, can be determined from a measurement without the window foil (right peak in fig. 3.6). With this value the linewidth including the energy straggling, ω_0', is calculated for the four foils using the ATIMA code. The total width is extracted from the measurements with the window foil (left peak in fig. 3.6). The weighted mean is used in eq. (3.2) to calculate ω_{rough}. All numbers are summarized in tab. 3.2.

[1] All width are in the following given as full width at half maximum.

With ω_{rough} one can estimate an upper limit for the roughness of the investigated foils. Via ATIMA the maximal deviation of the window thickness Δd_{max} is calculated from ω_{rough}. The relative thickness variation $\Delta d_{max}/d = R_{max}$ is then the maximal roughness R_{max} of the window foil, which is also listed in tab. 3.2.

The estimates show that the upper limits of the foil roughness are much higher than the variations one obtains from the direct thickness measurement shown in fig. 3.7. Thickness variations in the order of $\pm 10\,\%$ can already significantly influence the stopping efficiency, as demonstrated in section 3.1.1. Finally, only a direct measurement in the gas cell, which is planned for the near future, will show the true stopping distribution and efficiency.

3.2 Optimization of the ejection from the measurement trap

The contrast[2] is an important quantity to describe the quality of a cyclotron resonance and is defined as

$$C = \frac{t_{\mathrm{off}} - t_{\mathrm{in}}}{\sqrt{\sigma_{\mathrm{off}}^2 + \sigma_{\mathrm{in}}^2}} \quad , \tag{3.3}$$

where t_{in} is the time of flight of the ions that were resonantly excited by the cyclotron excitation and t_{off} is the time of flight of those ions that were not resonantly excited. σ_{in} and σ_{off} are the corresponding uncertainties. The definition of C is illustrated in fig. 3.8. It describes how well the non-resonantly excited ions are separated from the resonantly excited ones with respect to their time of flight.

A high contrast is for example needed in an on-line experiment when searching for an exotic nuclide with unknown mass. The better the contrast the less ions are necessary to find the cyclotron resonance of an ion with unknown mass. Especially for nuclides with very low production rates the measurement times become very long, which limit the achievable precision due to fluctuations and drifts of the magnetic field (s. section 3.3). In the worst case these field variations 'smear out' the resonance so much that a detection is no longer possible.

In addition to the impact on the measurement time, the contrast also influences the precision with which the cyclotron frequency can be determined for a given number of ions. As indicated in eq. (2.9) the uncertainty of the cyclotron frequency $\delta\nu_c$ is inversely proportional to the resolution and the square root of the number of ions. This relation results from the assumption that the resonance curve can be approximated by a Gaussian distribution. For a Gaussian curve the uncertainty of the centroid is exactly the standard deviation divided by the square root of the number of ions. However, ν_c is determined by a least-squares fit of the theoretically expected curve to the data points. Thus, the relation

[2] Sometimes one also finds the misleading expression 'signal-to-noise ratio'

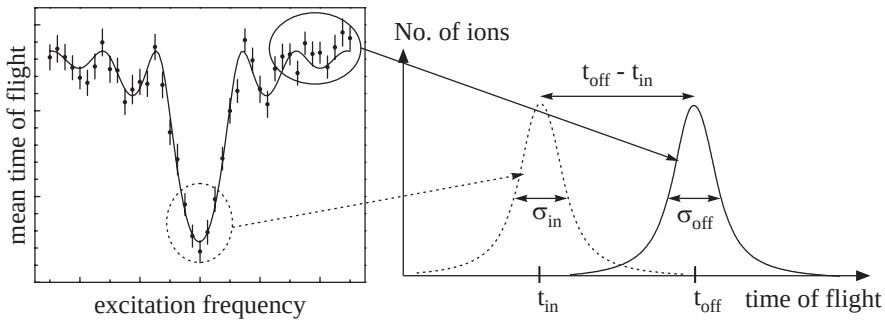

Figure 3.8: Definition of the contrast, which describes how well the resonant ions are separated from the non-resonant ones.

between $\delta\nu_c$ and R has to be modified:

$$\delta\nu_c = a\,\frac{\Delta\nu_{\mathrm{FWHM}}}{\sqrt{N}} = a\frac{\nu_c}{R\sqrt{N}} \quad . \tag{3.4}$$

The proportionality constant a describes the difference between the uncertainty resulting from the least-squares method and the one from the Gaussian theory.[3] Generally, the fit with the more complex resonance curve results in a smaller uncertainty than predicted by a pure Gaussian curve. For the cyclotron resonance shown in fig. 2.13, e.g., a reduction by $a \approx 0.5$ was obtained. The size of a depends on the contrast of the resonance and how the ions are distributed over frequency [Dwo06]. The latter dependence results from the fact that the data points on the steep slopes of a curve are more valuable for a fit than the ones in the extrema where the slope is almost zero. In any peak-fitting procedure the points around the maximum or on the baseline have less statistical weight in the determination of the centroid than the ones on the rising or falling edges. The dependence of a on the contrast can be explained similarly. A resonance with higher contrast has steeper slopes compared to one with lower contrast. As described above this results in a more precise determination of the centroid.

The quality of the resonance was in former times described by the TOF effect

$$TE = \frac{t_{\mathrm{off}} - t_{\mathrm{in}}}{t_{\mathrm{off}}} \quad , \tag{3.5}$$

which only takes the temporal separation between the resonantly excited and not resonantly excited ions into account. The contrast additionally considers the width of the time-of-flight distributions (denominator of C). This is important, since the temporal separation that is necessary to unambiguously divide the resonantly excited ions from the other ones depends on the width of their distributions, as shown in fig. 3.8. Usually one speaks about a significant separation when the difference between the two peaks is bigger than one full width at half maximum (FWHM), which corresponds to $C \approx 1.4$.

[3] In the Gaussian theory the standard deviation σ is used as width. The constant scaling factor between the here used full width at half maximum and σ is included in a.

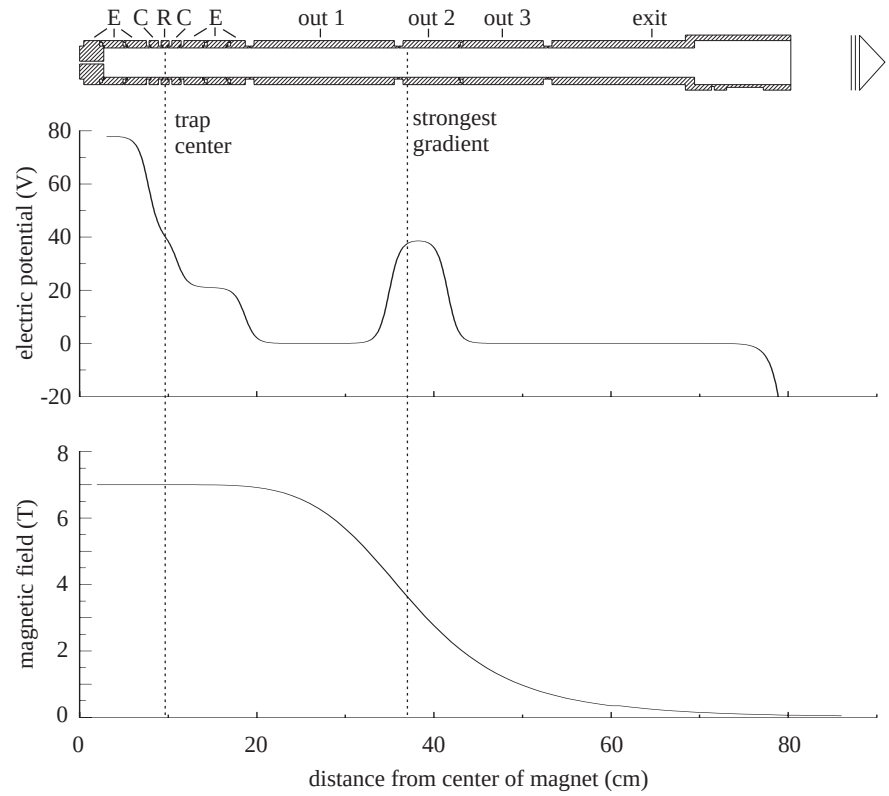

Figure 3.9: Axial electric potentials and magnetic field strengths, when ejecting the ions from the measurement trap. The drawing shows the electrodes of the measurement trap (c.f. fig. 2.11), the subsequent extraction electrodes and the multi-channel plate detector.

The contrast is maximized by increasing the depth of the resonance or decreasing the widths of the time-of-flight distributions. The depth depends mainly on the radial energy of the ions, which is defined by the amplitude of the magnetron excitation. As described in section 2.2.4 this way has certain limits due to a reduction of the extraction efficiency with too high magnetron amplitudes. The widths of the time-of-flight distributions are determined mainly by the axial energy distribution and the ejection of the ion cloud from the trap to the detector. The energy distribution is determined by the cooling in the purification trap and the transfer and capturing process in the measurement trap. Concerning the ejection, a faster extraction is generally advantageous for a small distribution. However, if the ions pass the magnetic field gradient too quickly the energy conversion from radial to axial motion will not be complete and one looses again in contrast. Thus, an optimal extraction scheme drags the ions quickly out of the trap, decelerates them in the region of the strongest gradient and accelerates them again to the detector.

Figure 3.9 shows in detail how such an extraction scheme can be accomplished. In the upper drawing the extraction electrodes from the measurement trap to the detector are shown. The magnetic field gradient is maximal around

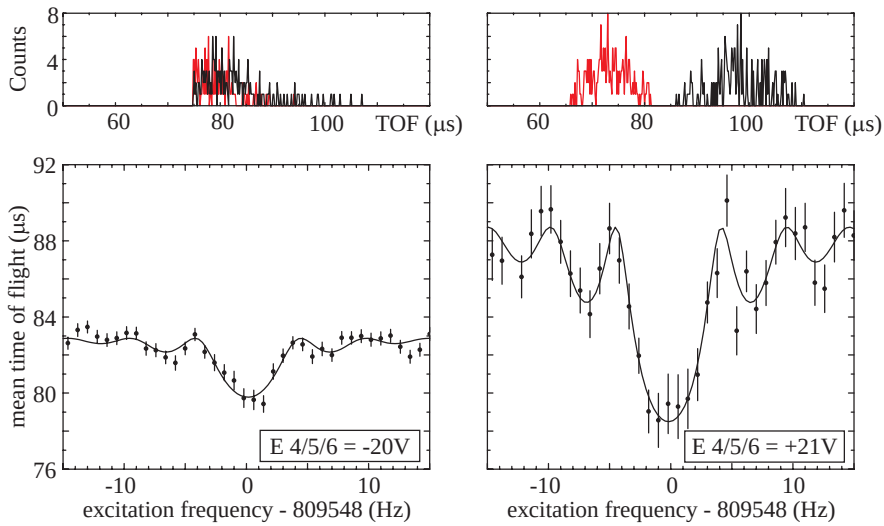

Figure 3.10: Comparison between a low ($C = 1.0$) and a high-contrast ($C = 1.8$) measurement. The only difference in the extraction is the potential of the end-cap electrodes E 4/5/6 of the measurement trap (c.f. fig. 3.9), which is changed from $-20\,\mathrm{V}$ to $+21\,\mathrm{V}$.

the electrode 'out 2', as indicated in the lower graph. The electric potentials of the optimized extraction scheme are plotted in the middle graph. Table 3.3 lists the corresponding voltages. The ions are first gently accelerated out of the trap by the end-cap electrodes. In the region of the strong field gradient they are almost stopped again to ensure a maximum conversion. Subsequently, they are accelerated to the detector in two steps, first by the electrodes 'out 3' and 'exit' and after completely leaving the gradient very strongly by the negative detector potential. A further decrease of the transfer potentials between the trap and the conversion region reduces the width of the time-of-flight distribution but does not help to gain in contrast. The same is true for the region after 'out 2'. However, an additional segmentation of the electrode 'out 3' may be advantageous to start the fast acceleration already earlier.

How sensitive the extraction potentials affect the contrast can be seen in

Table 3.3: Optimal potentials of the extraction electrodes resulting from the contrast optimization (c.f. fig. 3.9).

electrode	potential (V)
end-cap electrode E 4/5/6	21
extraction electrode out 1	0
extraction electrode out 2	37
extraction electrode out 3	0
extraction electrode exit	0

fig. 3.10, where a low-contrast measurement is compared with a high-contrast one. The only difference between the two measurements is the voltage at the end-cap electrodes, which is changed from $-20\,\mathrm{V}$ to $+21\,\mathrm{V}$. The two graphs at the bottom show the corresponding cyclotron resonances, which are scaled equally to visualize the clear difference between the measurements. For both measurements around 1600 ions were used leading in the frequency determination to a relative uncertainty of $2 \cdot 10^{-7}$ and $1 \cdot 10^{-7}$ in the low-contrast and in the high-contrast case, respectively. The effect can also be seen in the time-of-flight distributions shown in the upper graphs. While the two distributions are well separated in the high-contrast example they are indistinguishable in the low-contrast one.

The result of this optimizations is a significant increase in the contrast by 80 %. Under these conditions only 300 ions are necessary to optain a distinct resonance.

3.3 Uncertainties due to magnetic field fluctuations

Investigations of the uncertainties in the determination of the cyclotron frequency ratios (c.f. section 2.4) show that next to the pure statistical uncertainties several additional uncertainties have to be taken into account [Kel03]. In section 4.2 all uncertainty contributions are listed that are considered in the analysis procedure. One of the uncertainties originates from a lack of knowledge about the true magnetic field at the time of the measurement. As described in section 2.4 the field is calibrated by an interpolation of two reference measurements taken once before and once after the measurement of the ion of interest. Variations of the magnetic field in the time scale of the measurement time will lead to uncertainties in the field calibration and by that in the frequency ratio determination.

The main mechanisms causing fluctuations or drifts in the field of a superconducting magnet are:

- Even though the resistivity is zero the current in a superconducting coil is reduced due to a phenomenon called flux creep [And62, And64]. The decrease follows a logarithmic decay with long characteristic times of many years. Thus in short periods ($\leq 1\,\mathrm{a}$) the decay can be approximated to be linear. For the SHIPTRAP magnet the flux creep was determined to be around $2 \cdot 10^{-8}/\mathrm{h}$.

- Any ferromagnetic or paramagnetic object moving in the vicinity of the magnet can change its field. Significant variations can be seen for either very massive objects, e.g. the big crane of the experimental hall, or for objects like heavy tools that are used very close to the bore. These fluctuations are of course non-statistical and can only be avoided by preventing their causes.

- The magnetic susceptibility of any material depends on its temperature. The trap electrodes for example, which strongly influence the magnetic

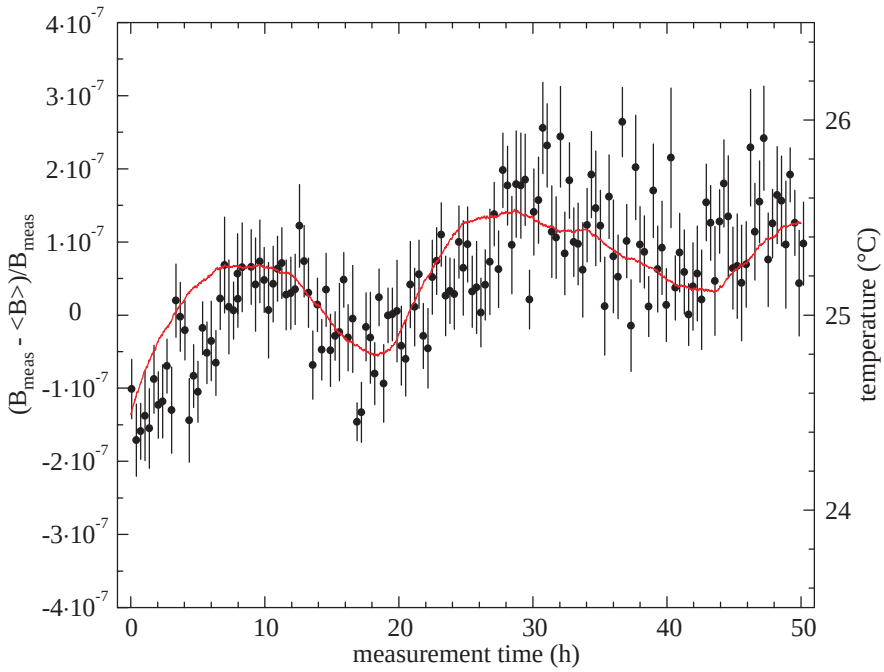

Figure 3.11: Temporal progression of the temperature (full line) and the magnetic field (data points) in the measurement trap. The temperature was measured with a Pt 100 resistor at the bore. The magnetic field was determined by the measuring the cyclotron frequency of ^{85}Rb ions.

field at the location of the ion cloud, are thermally connected to the bore of the magnet and the outer vacuum vessels and thus change their temperature with the room temperature. The magnetic field drift due to a temperature variation can be investigated by continuously measuring the cyclotron frequency of a reference ion over time. The result of such a measurement is shown in fig. 3.11, where the magnetic field and the temperature of the bore were recorded over two days. The plot shows that the mean trend of the magnetic field is clearly correlated to the room temperature leading to a shift of the magnetic field in the order of $3 \cdot 10^{-7}$/K.

- The air pressure determines the boiling point and by that the temperature of the liquid helium. As in the case of variations in the ambient temperature the magnetic susceptibility of every material thermally connected to the liquid helium dewar changes and leads to a variation of the magnetic field. The effect was measured to be in the order of $1{\cdot}10^{-9}$/mbar [Emm93].

The dependence of the magnetic field of the superconducting magnet on temperature and pressure has been studied at other Penning trap experiments like SMILETRAP [Ber02] and ISOLTRAP [Mar05, Her06]. The investigations show that the fluctuations of the magnetic field can be drastically reduced by a temperature and pressure stabilization. At SHIPTRAP the main influence on the magnetic field is the temperature (s. fig. 3.11), which will be stabilized in the near future.

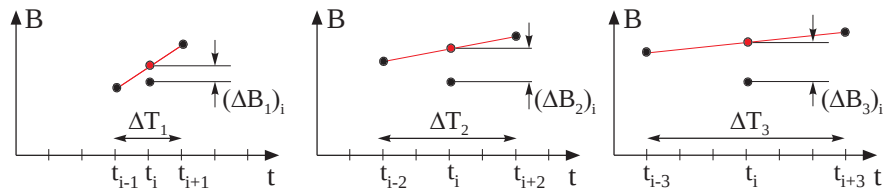

Figure 3.12: Principle of the magnetic field calibration. Magnetic field fluctuations lead to a deviation (δB) between the true (black point) and the interpolated value (red point) causing uncertainties in the frequency determination. The magnitude of the uncertainty depends on the time between the reference measurements ΔT as schematically indicated in the three graphs. The larger the time between the reference measurements gets ($\Delta T_3 > \Delta T_2 > \Delta T_1$) the higher the mean deviation will be ($\langle \Delta B_3 \rangle > \langle \Delta B_2 \rangle > \langle \Delta B_1 \rangle$).

Figure 3.11 shows that the magnetic field drifts due to temperature fluctuation are with a typical time scale of several hours longer than the usual measurement time (≤ 1 h). If the time of a measurement was much longer the strong correlation with the temperature would allow one to correct for the drift by recording the temperature. The graph also shows that there are short-time fluctuations that statistically scatter around the mean value. These arbitrary fluctuation can not be corrected for and lead to an additional uncertainty in the determination of the frequency ratio.

As said above a part of the additional uncertainty in the determination of the frequency ratio depends on the time between the reference measurements. To determine the magnitude of this time-dependent uncertainty the following measurement and analysis procedure was used: The cyclotron frequencies of ^{85}Rb or ^{133}Cs ions were recorded over some days. The data set was divided into bins of 20 min length and defined as 'frequency measurement of the ion under investigation' or as 'frequency measurement of the reference ion'. Using equation (2.5) the magnetic field was calculated (c.f. fig. 3.11). Always three succeeding measurements were grouped, as shown in the left graph of fig. 3.12. The two outer measurements are interpolated to the time of the central one (t_i) to calculate the difference in the magnetic field $(\Delta B_1)_i$. Repeating this procedure for the full data set one obtained a distribution of the $(\Delta B_1)_i$ as shown in fig. 3.13. The width of this distribution given by the standard deviation is a measure for the additional uncertainty. For example, for a measurement where the time span is 40 min the standard deviation is $6.8 \cdot 10^{-8}$ (fig. 3.13).

To extract only the time-dependent part in the additional uncertainty the same method as described in the last paragraph was repeated for different times between the reference measurements ΔT. This is done by selecting only every second, third, etc. measurement as shown in the middle and right graph of fig. 3.12. Calculating the standard deviation of the resulting distributions leads to additional data points. The result of this procedure is shown in fig. 3.14. The standard deviation of the ΔB distribution is plotted for ΔT up to 5 h. As expected the standard deviation increases with higher ΔT. The data point at ΔT= 0 ($\sigma = 5.2 \cdot 10^{-8}$) is the average uncertainty of all 20 min measure-

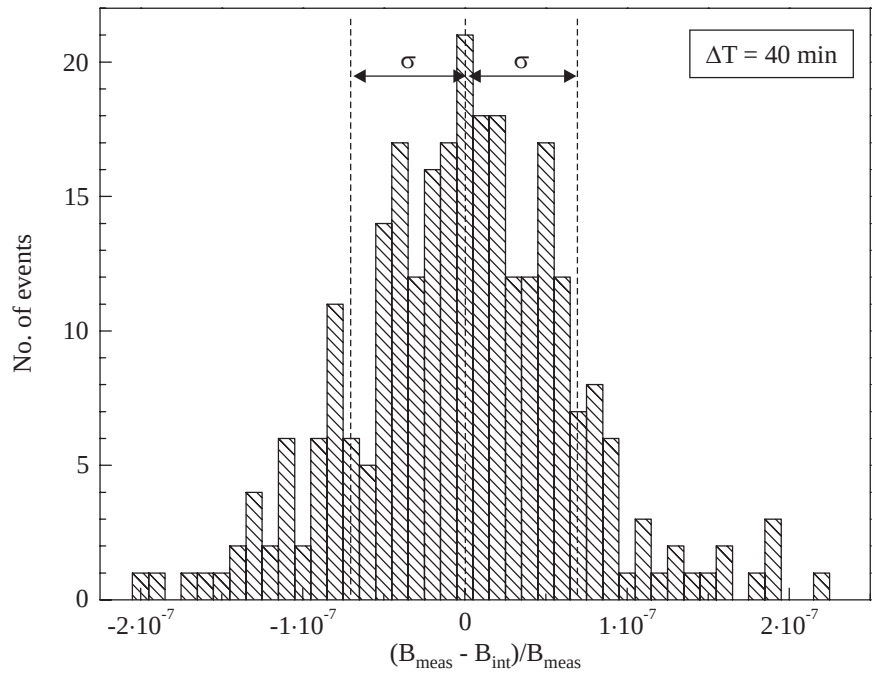

Figure 3.13: Histogram of the deviations between the true magnetic field and the interpolated one. The difference between the two reference measurements is 40 min. The standard deviation of this distribution is $\sigma = 6.8 \cdot 10^{-8}$.

ments, which represents the limiting uncertainty for a frequency determination of a 20 min measurement. Recent measurements with better statistics [Cha06] specify this value to $4.2 \cdot 10^{-8}$ (c.f. section 4.2). In first order the rise of the uncertainty with ΔT can be approximated to be linear (s. fig. 3.14). The time-dependent part of the additional uncertainty can then be determined by the slope of the fitted straight:

$$\sigma_{\mathrm{B}} = \frac{\partial \mathrm{B}}{\partial t} \cdot \frac{1}{\mathrm{B}} = 3 \cdot 10^{-9}/\mathrm{h} = 5 \cdot 10^{-11}/\mathrm{min} \tag{3.6}$$

The result shows that for the usual measurement times below 1 h the time-dependent uncertainty increases the residual uncertainty by at most 10 %. However, for, e.g., transuranium elements with production cross sections below 1 μb the measurement times will surely be longer than 1 h and the time-dependent uncertainty will significantly raise the total uncertainty.

The magnitude of the short-time fluctuations that limit the precision of a mass measurement at SHIPTRAP is significantly larger as for instance the ones measured at ISOLTRAP. There, a residual systematic uncertainty of $8 \cdot 10^{-9}$ [Kel03] could be measured because of the smaller short-time fluctuations. To investigate the origin of the fluctuations the data shown in fig. 3.11 were further analyzed. A fast Fourier transformation of the data, which could reveal individual noise sources, did not show any distinct peaks in the frequency spectra but only the usual 1/f and white noise. Furthermore, all histograms used for the analysis (c.f. fig. 3.13) show symmetric peaks around zero that follow a Gaussian

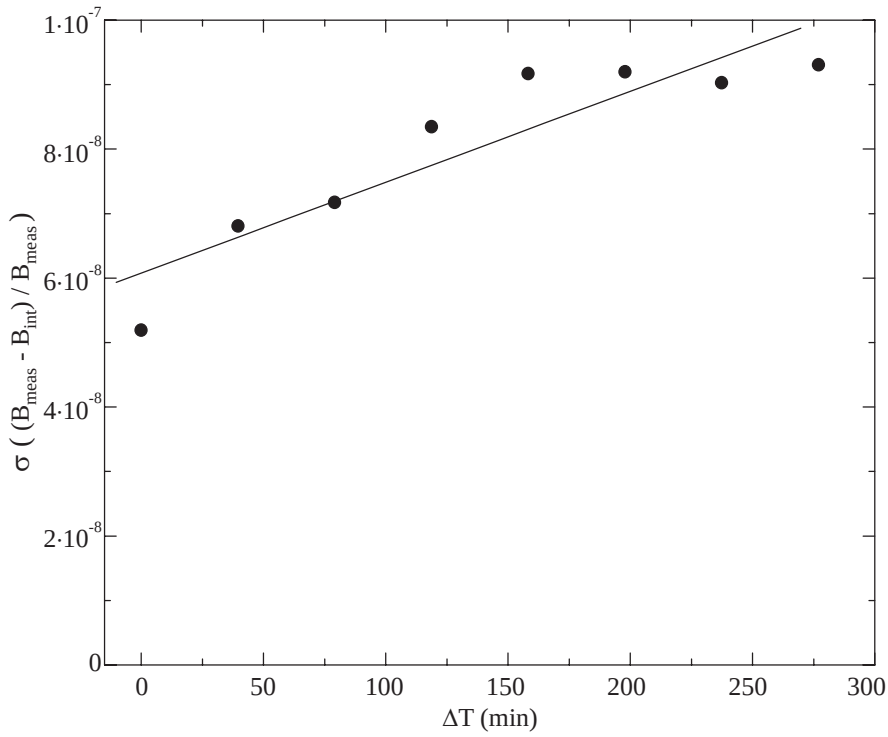

Figure 3.14: The standard deviations of the distribution of the relative magnetic field deviations as a function of the time between two reference measurements. The line shows a linear fit to the data points. The histogram leading to the data point at $\Delta T = 40$ min is shown in fig. 3.13.

distribution. A possible source for the fluctuations could lie in the instability of the power supplies used for the trap electrodes. A slight shift in the trap depth U_0 (c.f. fig. 2.9) changes the axial energy of the ions according to eq. (2.3). For a not ideal trap in which the magnetic field is not completely harmonic and/or the electrical field deviates from the pure quadrupole field, the change in the axial energy can lead to a shift of the cyclotron frequency [Bro86]. If power supplies with a better stability can reduce the magnitude of the short-time fluctuations will be seen in the near future, when the old power supplies are replaced by newer and more stable ones.

Chapter 4

On-line mass measurements around $A = 146$

At the end of 2005 two on-line experiments were performed at SHIPTRAP to investigate neutron-deficient isotopes of the rare-earth elements terbium, dysprosium, holmium, erbium and thulium. The results of these experiments are the first high-precision mass data at SHIPTRAP [Rau06a, Rau06b]. This chapter presents details of the experiments and describes the data analysis procedure and evaluation within the Atomic Mass Evaluation (AME) [Wap03]. In addition, the implications of the new data on nuclear structure and the location of the proton drip-line are discussed.

Figure 4.1: Nuclear chart displaying the 18 investigated nuclides. The mass values of the nine orange nuclides were known before, while the masses of the nine red nuclides were measured for the first time.

4.1 Experimental results

The two experiments at SHIPTRAP were performed in October 2005 (run #1) and December 2005 (run #2). A ^{58}Ni beam with an energy of 4.36 MeV/u and 4.60 MeV/u, respectively, hit a 0.626 mg/cm^2 thick ^{92}Mo foil to produce neutron-deficient isotopes in the region around ^{147}Ho in fusion evaporation reactions. The average nickel beam intensity was around 200 particle-nA. The molybdenum foil was specified to be enriched to 97.4% of ^{92}Mo. However, the detection of the three nuclides ^{147}Tb, ^{147}Dy and ^{148}Ho suggested a lower ^{92}Mo content. Since the β-decay half-lives of ^{147}Ho and ^{148}Er are much longer than the typical measurement cycle time of one second, these nuclides could only have been produced from the molybdenum isotopes heavier than ^{92}Mo.

Table 4.1: Half-life $T_{1/2}$ and spin-parity I^P of the investigated nuclides taken from [Aud03a]. The brackets () indicate uncertain spin and/or parity values. Values marked with # are only estimated from systematic trends. E_{exc} is the excitation energy of the first isomeric state [Aud03a].

Nuclide	$T_{1/2}$	I^P	E_{exc} (keV)
^{143}Tb	12 s	$(11/2^-)$	
^{143m}Tb	<21 s	$\#5/2^+$	#0(100)
^{147}Tb	1.64 h	$\#1/2^+$	
^{147m}Tb	1.87 min	$(11/2^-)$	50.6(9)
^{143}Dy	5.6 s	$(1/2^+)$	
^{143m}Dy	3.0 s	$(11/2^-)$	310.7(6)
^{144}Dy	9.1 s	0^+	
^{145}Dy	9.5 s	$(1/2^+)$	
^{145}Dy	14.2 s	$(11/2^-)$	118.2(2)
^{146}Dy	33.2 s	0^+	
^{147}Dy	40 s	$1/2^+$	
^{147m}Dy	55 s	$11/2^-$	750.5(4)
^{148}Dy	3.3 min	0^+	
^{144}Ho	700 ms		
^{145}Ho	2.4 s	$(11/2^-)$	
^{146}Ho	3.6 s	10^+	
^{147}Ho	5.8 s	$(11/2^-)$	
^{148}Ho	2.2 s	1^+	
^{148m}Ho	9.49 s	(6^-)	#400(100)
^{146}Er	1.7 s	0^+	
^{147}Er	2.5 s	$(1/2^+)$	
^{147m}Er	2.5 s	$(11/2^-)$	#100(50)
^{148}Er	4.6 s	0^+	
^{147}Tm	580 ms	$11/2^-$	
^{148}Tm	700 ms	(10^+)	

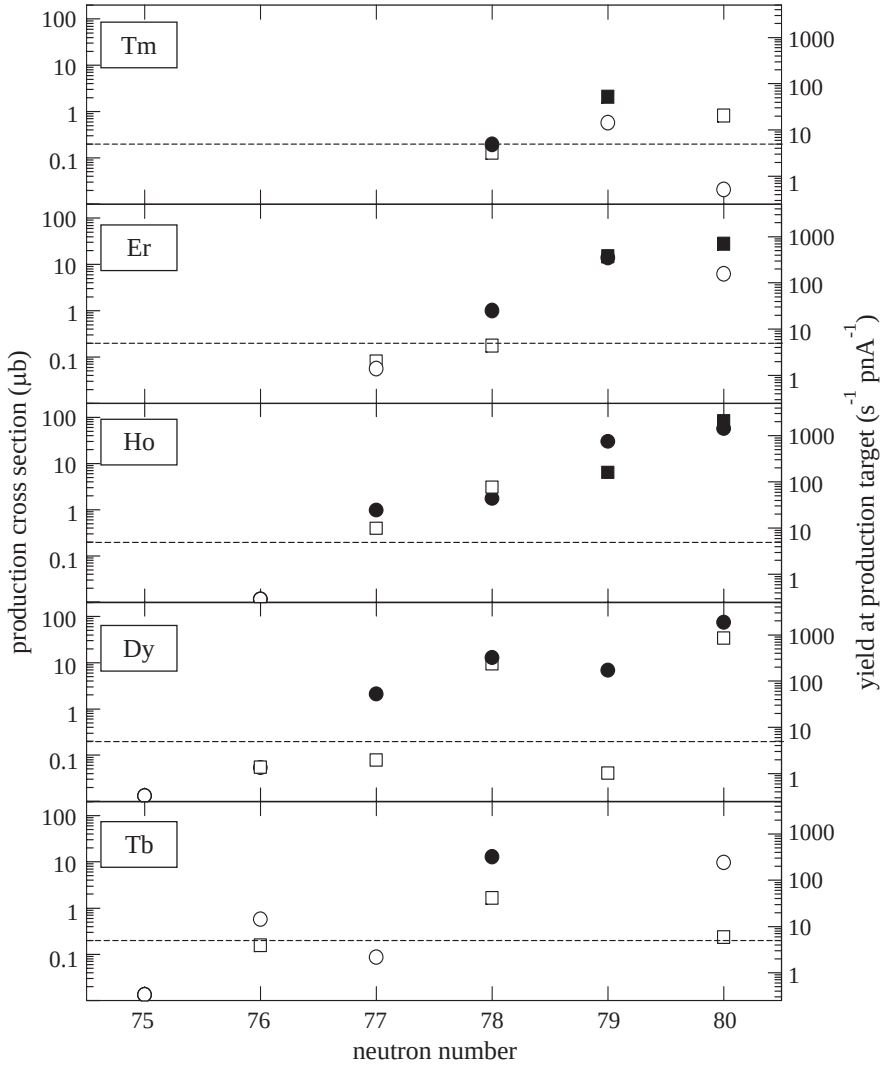

Figure 4.2: Production cross sections and corresponding yields for the reaction ^{58}Ni on 0.626 mg/cm^2 ^{92}Mo calculated using the HIVAP code [Rei81]. The beam energies are 4.36 MeV/u (squares) and 4.6 MeV/u (circles). The full symbols indicate the nuclides measured within this work. ^{147}Tm has with around 200 μb the lowest production cross section of all nuclides (dashed line).

The radioactive ions were stopped in the gas cell, accumulated in the RFQ buncher and transferred into the purification trap. As discussed in section 2.2 neither SHIP nor the SHIPTRAP devices preceding the traps are very mass selective. The first unambiguous identification and separation of the fusion evaporation products is therefore performed in the purification trap by the mass-selective buffer-gas technique. Figure 2.12 on page 18 shows as an example a cooling resonance around ^{147}Ho. A mass resolving power of $R = 50\,000$ was sufficient to clearly separate the isobars at mass number 147.

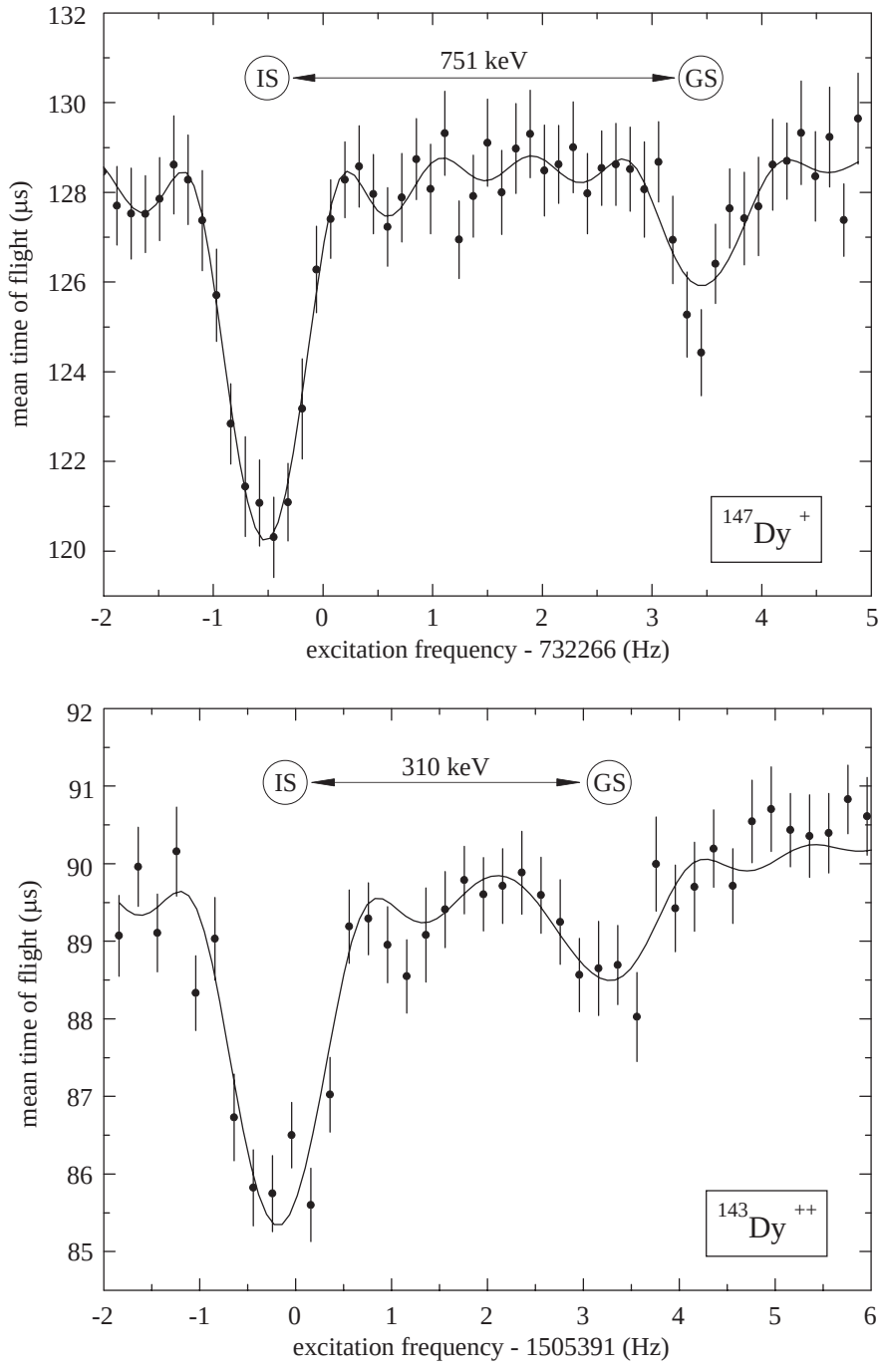

Figure 4.3: Cyclotron resonances of $^{143}Dy^{++}$ and $^{147}Dy^{+}$. An excitation time of 900 ms leading to a mass resolving power of $1.5{\cdot}10^6$ was used to separate the ground state (GS) from the isomeric state (IS) with an excitation energy of 310 keV and 751 keV, respectively. The solid line represents a fit of the theoretically expected line shape [Kön95] to the data points.

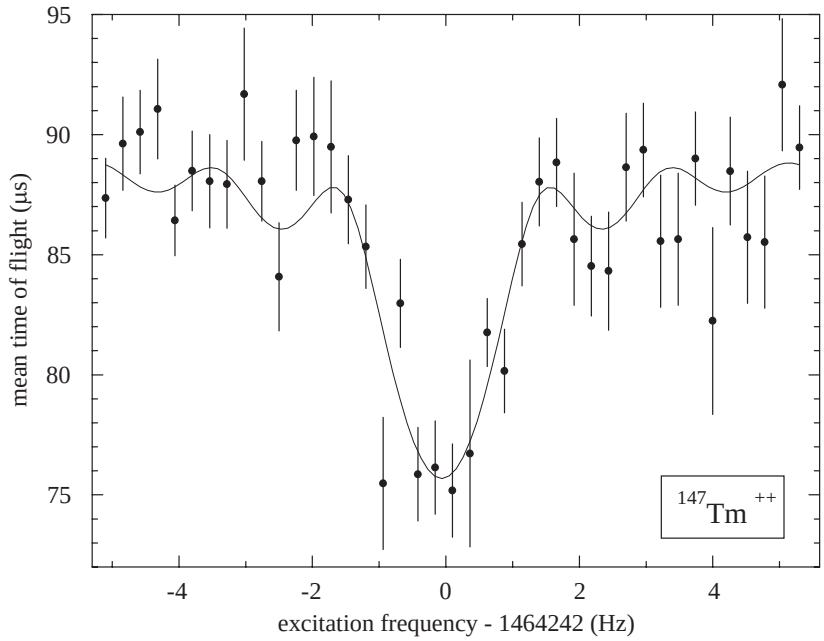

Figure 4.4: Cyclotron resonance of $^{147}Tm^{++}$. For this resonance 308 ions were recorded in 70 min. The excitation time was 600 ms. The solid line represents a fit of the theoretically expected line shape [Kön95] to the data points.

The cyclotron frequency in the purification trap was fixed to select and transfer only the specific nuclide of interest into the measurement trap. Here, the cyclotron frequency of this nuclide was measured with the TOF-ICR method (s. section 2.2.4). In total, we were able to determine the masses of 18 short-lived nuclides as visualized in fig. 4.1. Table 4.1 summarizes the half-lives and spin-parity values of the investigated nuclides. The production cross sections and yields are plotted in fig. 4.2. They were calculated for the reaction ^{58}Ni on ^{92}Mo for the two used beam energies using HIVAP [Rei81]. The production cross sections range from 200 μb (^{147}Tm) to 80 mb (^{147}Ho). Assuming a beam intensity of 200 particle-nA and a SHIP transmission of 50 % these cross sections correspond to an ion rate of 500 to 200 000 ions/s in front of the gas cell.

The excitation time in the measurement trap was usually 900 ms leading to a resolving power of $1.5 \cdot 10^6$. This allowed us to separate the first isomeric states of ^{143}Dy and ^{147}Dy (s. fig. 4.3) with excitation energies of about 310 keV and 750 keV [Aud03a], respectively. The cyclotron frequency of both states were individually extracted and treated as two measurements. They were both used to determine the mass of the corresponding ground state as described in detail in section 4.3.2.

^{147}Tm is in many respects the most exotic of the measured nuclides. With 100 - 200 μb and 700 ms it has the smallest production cross section and shortest half-life of all 18 nuclides (c.f. section 2.3). With an average count rate of 2 ions/s a measurement time of 5 h was necessary to measure the frequency ratio to an uncertainty below $1 \cdot 10^{-7}$.

Table 4.2: Frequency ratios $r = \nu_c/\nu_{ref}$ with their statistical (first bracket) and total uncertainty (second bracket) of the measured nuclides. The index x indicates a measurement in which a possible isomeric state was not resolved, which necessitates a special treatment in the mass evaluation (s. section 4.3.2). Columns three and four show the number of recorded scans N_s and the number of ions N_{ion} recorded in all scans. Column six lists the relative overall uncertainties.

Nuclide	Ref.	N_s	N_{ion}	Frequency ratio r (σ_{stat}) (σ_{tot})	σ_{tot}/r $\cdot 10^8$
Run #1					
$^{147x}Tb^{+}$	$^{133}Cs^{+}$	3	728	1.105478772(76)(89)	8.1
$^{147}Dy^{+}$	$^{133}Cs^{+}$	3	2644	1.105531393(99)(109)	9.9
$^{147m}Dy^{+}$	$^{133}Cs^{+}$	4	5799	1.105537346(54)(71)	5.4
$^{148}Dy^{+}$	$^{133}Cs^{+}$	2	1216	1.113025899(92)(103)	9.3
$^{146}Ho^{+}$	$^{133}Cs^{+}$	6	1937	1.098111737(63)(78)	7.1
$^{147}Ho^{+}$	$^{133}Cs^{+}$	11	7190	1.105599461(36)(59)	5.3
$^{147x}Er^{+}$	$^{133}Cs^{+}$	3	1464	1.105674084(65)(80)	7.2
$^{148}Er^{+}$	$^{133}Cs^{+}$	3	1502	1.113158224(67)(82)	7.4
$^{148}Tm^{+}$	$^{133}Cs^{+}$	5	1633	1.113260920(70)(84)	7.6
Run #2					
$^{143x}Tb^{++}$	$^{85}Rb^{+}$	2	2763	0.841667357(34)(49)	5.8
$^{143}Dy^{++}$	$^{85}Rb^{+}$	2	745	0.841719457(93)(101)	12.0
$^{143m}Dy^{++}$	$^{85}Rb^{+}$	2	1205	0.841721522(74)(83)	7.4
$^{144}Dy^{++}$	$^{85}Rb^{+}$	6	3322	0.847580193(28)(45)	5.3
$^{145x}Dy^{++}$	$^{85}Rb^{+}$	5	9122	0.853458676(17)(40)	4.7
$^{146}Dy^{++}$	$^{85}Rb^{+}$	13	13372	0.859319365(22)(43)	5.0
$^{144}Ho^{++}$	$^{85}Rb^{+}$	3	2114	0.847655803(40)(54)	6.3
$^{145}Ho^{++}$	$^{85}Rb^{+}$	4	2587	0.853515790(30)(47)	5.5
$^{146}Ho^{++}$	$^{85}Rb^{+}$	3	4609	0.859390963(49)(61)	7.1
$^{147}Ho^{++}$	$^{85}Rb^{+}$	9	11078	0.865250860(24)(44)	5.0
$^{148x}Ho^{++}$	$^{85}Rb^{+}$	4	2116	0.871126392(42)(56)	6.4
$^{146}Er^{++}$	$^{85}Rb^{+}$	3	1613	0.859434605(41)(54)	6.3
$^{147x}Er^{++}$	$^{85}Rb^{+}$	4	8420	0.865309144(32)(49)	5.7
$^{147}Tm^{++}$	$^{85}Rb^{+}$	3	617	0.865375925(51)(63)	7.2

Table 4.2 gives an overview over the results obtained. A detailed description of the analysis procedure follows in the next section. In the first experiment only singly charged ions were detected, while in the second one the majority of the ions were doubly charged. The availability of sizable amounts of doubly charged ions is a clear indication for excellent vacuum conditions during the experiment: A pressure of about 10^{-10} mbar had been reached in the gas cell before it was filled with helium buffer gas. To minimize mass-dependent systematic uncertainties ^{133}Cs and ^{85}Rb were used as reference ions for the singly and doubly charged ions, respectively. Three nuclides (^{146}Ho, ^{147}Ho and ^{147}Er) were measured in both beamtimes, which allows for a consistency check of the data.

The relative total uncertainties (s. column seven in tab. 4.2) range from $4.7 \cdot 10^{-8}$ to $12 \cdot 10^{-8}$ with an average value of $6.8 \cdot 10^{-8}$. The systematic uncertainties are often the major part of the total uncertainty. An improvement of the statistical uncertainty by prolonging the excitation time or measuring further resonances would decrease the total uncertainty by at most a factor of three.

4.2 Data analysis

The frequency ratios from the experiments presented in the previous section were analyzed similarly to the method used at ISOLTRAP [Kel03]. This section describes the analysis procedure in detail.

- The first step is a fit of the theoretically expected line shape to the measured resonance, as described in section 2.2.4. One of the free parameters is the center of the resonance, i.e. the cyclotron frequency. The fit also yields the statistical uncertainty σ_s.
- Contaminations from e.g. isomers of the nuclide of interest can shift the cyclotron frequency. Therefore a count rate class analysis was performed where possible [Kel03]. This usually slightly shifts the frequency and increases the uncertainty by a factor of two to three. If this analysis was not possible, mostly because of low statistics, the uncertainty of the frequency was manually increased to an averaged value. The latter was determined from the cases in which the count rate class analysis had been applied successfully. Without such an adjustment a resonance with poor statistics would unreasonably get a lower uncertainty than those with good statistics.
- The cyclotron frequencies of the reference ions were measured about once per hour alternately with the measurements of the ions of interest. To obtain the reference frequency at the time of the measurement of the radioactive ion the two adjacent values were interpolated linearly.
- The frequency ratios were calculated and an uncertainty $\sigma_B = 3 \cdot 10^{-9}/\mathrm{h}$ depending on the time interval between the two reference measurements was quadratically added to the uncertainty of each frequency ratio. As discussed in detail in section 3.3 the uncertainty arises due to fluctuations of the magnetic field.
- All frequency ratios obtained for a given nuclide were averaged. Both the internal uncertainty

$$\sigma_{\mathrm{in}} = 1/\sqrt{\sum_i 1/\sigma_i^2} \tag{4.1}$$

and the external or outer uncertainty

$$\sigma_{\mathrm{out}} = \sqrt{\frac{\sum_i \left((r_i - < r >)^2 / \sigma_i^2 \right)}{(N-1) \sum_i 1/\sigma_i^2}} \tag{4.2}$$

were calculated and compared. The ratio $\sigma_{\text{out}}/\sigma_{\text{in}}$ is always close to one, which signifies that the remaining scattering of the individual measurements is purely statistical. For all nuclides the inner uncertainty was used.

- From cross-reference mass measurements with carbon clusters a relative, mass-dependent shift of $\epsilon_m = (1.1 \pm 1.7) \cdot 10^{-10}/u \cdot \Delta(m/q)$ was determined [Cha06], where $\Delta(m/q)$ is the difference between the mass-to-charge ratio of the reference ion relative to that of the ion of interest. The averaged frequency ratio was corrected by using ϵ_m and the uncertainty of ϵ_m was quadratically added to the total uncertainty.

- The cross-reference measurements also allowed for a determination of a relative residual uncertainty of $4.2 \cdot 10^{-8}$ [Cha06], which was quadratically added to give the total uncertainty of the frequency ratio.

4.3 Atomic mass evaluation

The frequency ratios obtained in this work (tab. 4.2) were included in the Atomic Mass Evaluation (AME). This was done in collaboration with Georges Audi during an extended visit at the Centre de Spectrométrie Nucléaire et de Spectrométrie de Masse (CSNSM) in Orsay. The AME primarily collects all available mass data from mass spectrometric as well as decay energy measurements. Moreover, wherever multiple input data exist for a given nuclide an adjustment procedure is performed using the least-squares method [Wap03]. In the following all mass values are given as mass excess

$$M = m - A\,u \tag{4.3}$$

with m being the atomic mass, A the mass number and u the atomic mass unit.

Table 4.3 shows all in- and output values in comparison with the previous literature values [Aud03b]. The data are plotted in fig. 4.5. For some nuclides a contamination with an isomeric state could not be excluded, hence a correction, which is described in the next section, had to be applied. It is followed by a detailed description of the treatment of the input values and a summary of the results of the evaluation.

4.3.1 Correction for admixtures of isomers with known abundance ratios

When two states, usually the ground and the first isomeric state, of unknown mixture are not resolved in a measurement, the data are corrected as described in appendix B of [Wap03]. This procedure usually leads to a significantly increased uncertainty mainly due to the fact that the mixing ratio R_m between ground state and isomer is not sufficiently well known. In this work, however, R_m could be estimated for some nuclides: In the TOF-ICR signals of ^{143}Dy and ^{147}Dy

Table 4.3: Results of the atomic mass evaluation. Column two to four give the mass excesses of the data obtained in this work M_{exp}, the previous literature values M_{AME} [Aud03b] and the newly adjusted values M_{new}. ΔM are the rounded differences between the experimental data and the previous ones ($M_{\mathrm{exp}} - M_{\mathrm{AME}}$). The influences of our experimental mass on the new adjusted mass is given in column six. The symbol # indicates that the mass excess was estimated in AME 03 from systematic trends. For ^{146}Er and ^{147}Tm the influence is not 100 % due to a Q_p measurement of the proton decay. For 13 nuclides the new mass value is only determined by the SHIPTRAP measurement. For ^{147}Tb, ^{147}Dy, ^{148}Dy, ^{146}Er and ^{147}Tm the adjustment procedure slightly changes the mass excess.

Nuclide	M_{exp} (keV)	M_{AME} (keV)	M_{new} (keV)	ΔM (keV)	Infl (%)
^{143}Tb	-60420(50)	-60430(60)	-60420(50)	10(80)	100
^{147}Tb	-70740(11)	-70752(12)	-70746.2(8.1)	12(16)	53
^{143}Dy	-52169(13)	-52320(200)#	-52169(13)	150(200)	100
^{144}Dy	-56570.1(7.1)	-56580(30)	-56570.1(7.1)	10(30)	100
^{145}Dy	-58242.6(6.5)	-58290(50)	-58242.6(6.5)	47(50)	100
^{146}Dy	-62554.7(6.7)	-62554(27)	-62554.9(6.7)	0(28)	100
^{147}Dy	-64197.9(8.8)	-64188(20)	-64194.7(8.1)	-10(22)	83
^{148}Dy	-67861(13)	-67859(11)	-67860.2(8.2)	-2(17)	40
^{144}Ho	-44609.5(8.5)	-45200(300)#	-44609.5(8.5)	590(300)	100
^{145}Ho	-49120.1(7.5)	-49180(300)#	-49120.1(7.5)	60(300)	100
^{146}Ho	-51238.2(6.6)	-51570(200)#	-51238.2(6.6)	330(200)	100
^{147}Ho	-55757.1(5.0)	-55837(28)	-55757.1(5.0)	80(28)	100
^{148}Ho	-57990(80)	-58020(130)	-57990(80)	30(150)	100
^{146}Er	-44325.0(8.6)	-44710(300)#	-44322.0(6.7)	390(300)	61
^{147}Er	-46610(40)	-47050(300)#	-46610(40)	440(300)	100
^{148}Er	-51479(10)	-51650(200)#	-51479(10)	170(200)	100
^{147}Tm	-35969.8(9.9)	-36370(300)#	-35974.4(6.8)	400(300)	45
^{148}Tm	-38765(10)	-39270(400)#	-38765(10)	500(400)	100

both the $1/2^+$-ground state and the $11/2^-$-isomeric state were clearly resolved (fig. 4.3), which allowed for a determination of R_m according to

$$R_m = A_{IS}/(A_{IS} + A_{GS}) \quad , \tag{4.4}$$

where A_{IS} and A_{GS} are the amplitudes of the signals assigned to the isomer and the ground state in the TOF-ICR spectra. One ^{143}Dy file ($R_m = 0.71(9)$) and three ^{147}Dy files ($R_m = 0.76(5)$, 0.74(2), 0.74(2)), all being in good agreement within each other, result in a weighted mean of $R_m = 0.741(13)$. The same R_m value was used for nuclides with non-resolved isomeric states but equal spin and parity values, i.e. ^{147}Tb, ^{145}Dy and ^{147}Er. This approximation is based on the assumption that the production reactions for the $1/2^+$ ground state and the $11/2^-$ isomer of these isotopes, i.e. ^{94}Mo(^{58}Ni, $5p$), ^{92}Mo(^{58}Ni, $4p\,1n$) and ^{92}Mo(^{58}Ni, $2p\,1n$) yield the same R_m value as that found for ^{143}Dy and ^{147}Dy, produced through ^{92}Mo(^{58}Ni, $4p\,3n$) and ^{94}Mo(^{58}Ni, $4p\,1n$).

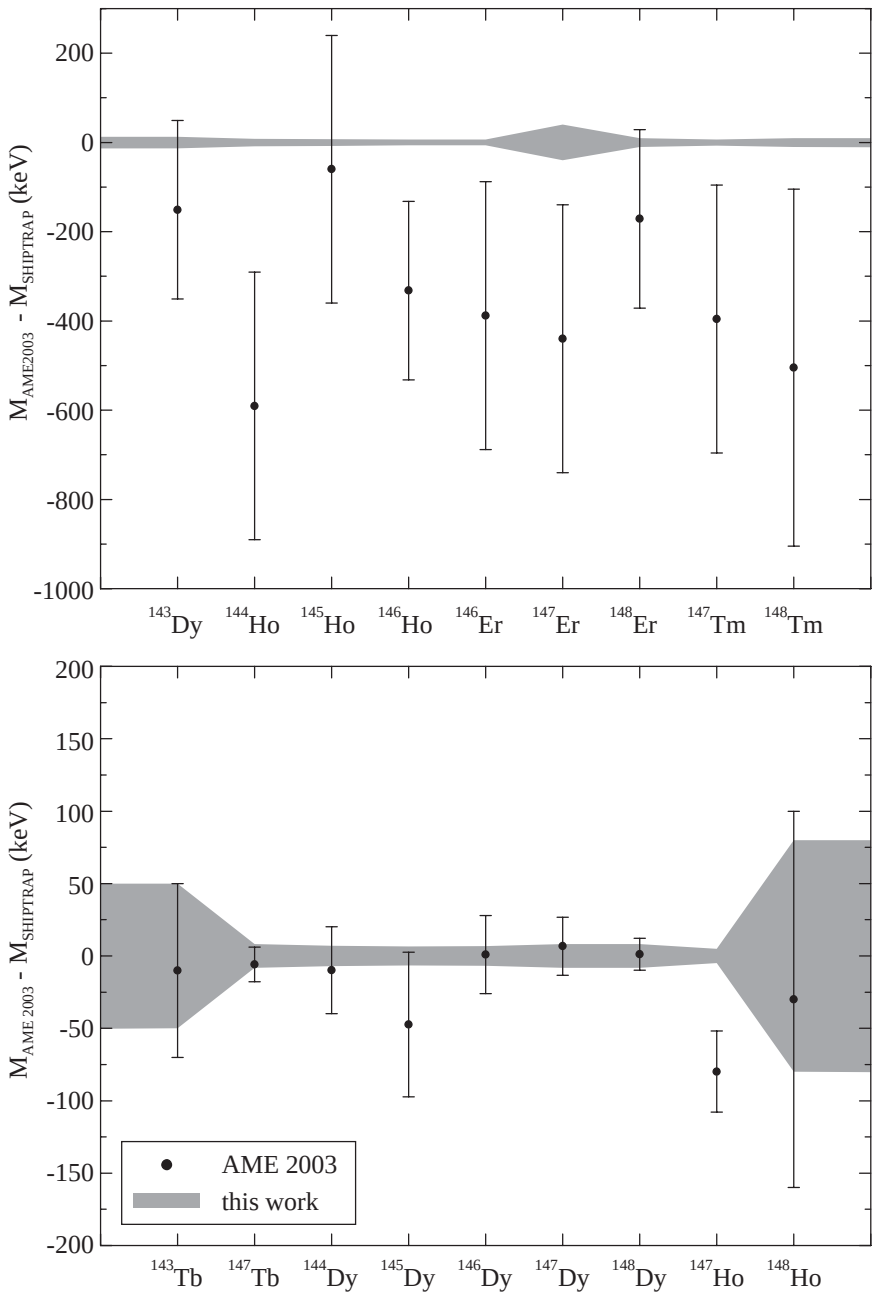

Figure 4.5: Comparison between the AME mass values [Aud03b] and the data from this work. The new data define the zero line. The uncertainties are indicated by an error band. The upper graph compares the new mass values with those data that were only estimated from systematic trends, while the lower graph compares them to already known but less accurately measured data.

The mass excess of the ground state can then be calculated by

$$M_{GS} = M_{exp} - R_m \cdot E_{exc} \quad , \tag{4.5}$$

where M_{exp} is the measured mass excess, E_{exc} the excitation energy of the isomeric state and R_m the ratio determined by the resolved resonances of ^{143}Dy and ^{147}Dy.

For ^{148}Ho, with 6^--isomeric and 1^+-ground state (s. tab. 4.1), we assumed the same ratio because of the fact that the spin difference is the same as for ^{143}Dy and ^{147}Dy. Since the absolute spin values are different we increased the uncertainty by a factor of 10 and applied $R_m = 0.74(15)$.

4.3.2 Treatment of input values

^{143}Tb

The measured mass excess of $-60419.5(7.8)$ keV for ^{143}Tb was corrected for an admixture of a possible isomeric state with unknown abundance and an estimated excitation energy of $0(100)$ keV to $-60420(50)$keV. This agrees with the previous value of $-60434(60)$ keV [Aud03b], which was determined by a mass measurement ($-60434(32)$ keV) at the Experimental Storage Ring (ESR) of GSI [Lit05] that was also corrected for isomeric contamination. An averaging of the two data would artificially decrease the uncertainty that arises due to the lack of information on the isomeric state. Since the ESR result has a much higher uncertainty only the SHIPTRAP measurement will thus be considered in the AME.

^{147}Tb

^{147}Tb has an isomeric state with an excitation energy of $50.6(9)$ keV [Alk93] that could not be resolved in the measurement. The spin and parity values of ground ($1/2^+$) and isomeric state ($11/2^-$) correspond to those of ^{143}Dy and ^{147}Dy. Hence the same mixing ratio of $R_m = 0.741(13)$ is assumed, as described in section 4.3.1. The measured value of $-70702(11)$ keV is corrected in this way to $-70740(11)$ keV, which agrees with the previous result of $-70752(12)$ keV [Aud03b]. The newly adjusted mass value is $-70746.2(8.1)$ keV determined to 53% by this work and 47% by Q_{β^+} measurements, all input data being in good agreement.

^{143}Dy

For ^{143}Dy the mass excess of the ground state ($-52178(16)$ keV) and of the first isomeric state ($-51851(13)$ keV) were measured. The difference of $327(21)$ keV agrees with the previously measured excitation energy of $310.7(6)$ keV [Xu03]. The mass excess of the isomeric state minus the excitation energy is averaged with the ground state value. The smaller uncertainty is used since the two data are correlated and the averaging would artificially decrease the uncertainty. The new value of $-52169(13)$ keV agrees with the previously estimated value of $-52320(200)$ keV.

^{144}Dy

The measured mass excess of $-56570.1(7.1)$ keV for ^{144}Dy agrees with the previously measured value of $-56585(31)$ keV [Lit05]. Due to its four times lower uncertainty the new value supersedes the previous result.

^{145}Dy

The known isomeric state of ^{145}Dy with an excitation energy of 118.2(2) keV [Tot93a] could not be resolved in the measurement. Again the spin and parity values of ground $(1/2^+)$ and isomeric state $(11/2^-)$ match those of ^{143}Dy and ^{147}Dy thus an abundance ratio of $R_m = 0.741(13)$ is assumed. This leads to a correction of the measured value of $-58155.0(6.3)$ keV to $-58242.6(6.5)$ keV. The new value agrees with the previous one of $-58290(50)$ keV [Aud03b] coming from Q_β measurements that will not be considered any further because of its seven times higher uncertainty.

^{146}Dy

^{146}Dy has a known isomeric state with a half-life of only 150 ms [Gui82] which is too short to create a contamination in our experiment. The measured mass excess of $-62554.7(6.7)$ keV agrees with the previous value of $-62554(27)$ keV [Aud03b] that was mainly influenced by an ESR measurement ($-62550(28)$ keV) [Lit05]. The adjusted value is -62554.9(6.7)keV.

^{147}Dy

The TOF-ICR spectra of ^{147}Dy allowed for a determination of the mass excess of the ground state ($-64188(14)$ keV) and the first isomeric state ($-63450.8(8.8)$ keV). The mass difference of 737(16) keV confirms the excitation energy of 750.5(4) keV [Aud03a]. The mass of the isomeric state minus the excitation energy is averaged with the ground state value to $-64197.9(8.8)$ keV. Like for ^{143}Dy only the smaller uncertainty is used. This value agrees with the previous one of $-64188(20)$ keV [Aud03b] and leads to a new mass excess of $-64194.7(8.1)$ keV, influenced to 17% from two ESR measurements [Lit05] and 83% from SHIPTRAP, which agree well with each other.

^{148}Dy

The result of this measurement of $-67861(13)$ keV agrees with the previous value of $-67859(11)$ keV that was mainly determined by ISOLTRAP [Bec00] and ESR [Lit05] measurements. The newly adjusted value results in $-67860.2(8.2)$ keV, influenced to 40% from this work, 30% from ISOLTRAP, 26% ESR and 4% from Q_{β^+} measurements [Kel95]. All values are in good agreement with each other.

^{144}Ho

The measured mass excess of $-44609.5(8.5)$ keV for ^{144}Ho deviates from the previously estimated value ($-45200(300)$ keV) by 590 keV or about two standard

deviations. This is the largest deviation occurring in this set of measurements. There is a report about an isomeric state [Cul01] that is, with a half-life of only 500 ns, not detectable in this experiment. Likewise the spectra and the count rate class analysis did not show an indication for possible contaminations.

^{145}Ho

Estimates suggest for ^{145}Ho an isomeric state with a half-life of 100 ms [Aud03a] that is too short to be observed in this experiment. The measured value of $-49120.1(7.5)$ keV agrees with the estimate of $-49180(300)$ keV. For measurements that show a longer half-life, this mass has to be corrected for a mixture of isomeric and ground state.

^{146}Ho

^{146}Ho is one of the three nuclides where two independent measurements were performed in the two runs. The singly charged ion $^{146}Ho^{+}$ yields with ^{133}Cs as a reference a mass excess of $-51248.1(9.6)$ keV, while the doubly charged ion $^{146}Ho^{++}$ with ^{85}Rb as a reference results in a mass excess of $-51228.7(9.7)$ keV. Both values agree within their combined uncertainties. The averaged value of $-51238.2(6.6)$keV is 330 keV higher than the estimate of $-51570(200)$ keV. There is no report of an isomeric state until now and neither the spectra nor the count rate class analysis give an indication for its existence.

^{147}Ho

^{147}Ho was also measured independently in the two runs. Both results, $-55761.0(7.3)$ keV compared to ^{133}Cs and $-55753.6(6.9)$ keV compared to ^{85}Rb, agree well with each other but deviate by two standard deviations from the previously measured value of $-55837(28)$ keV [Lit05]. The reason for this discrepancy is presently not understood. ^{147}Ho is with 20 measurements the nuclide with the highest statistics. Furthermore, it was determined in both runs compared to different reference ions. In fig. 4.6 the results of all measurements are shown, which agree very well with each other. The discrepancy could lie in the existence of an isomeric contamination in one of the two experiments, but neither the TOF-ICR spectra and nor the count rate class analysis gave evidence for such a contamination in this experiment. Because of the larger uncertainty the previous value will not be used in the future. The newly adjusted mass excess is $-55755.1(5.0)$ keV.

^{148}Ho

^{148}Ho has a known long-lived isomeric state with an estimated excitation energy of 400(100) keV [Aud03a]. If this was correct and if the isomer was produced in sizable amount in the ^{94}Mo(^{58}Ni, $3p\,1n$) reaction, the two states could be resolved with the present set-up as shown for ^{143}Dy. The measured spectra, however, did not give any indication of an isomeric state, which led to the suggestion that the estimated excitation energy was too high. As a result the

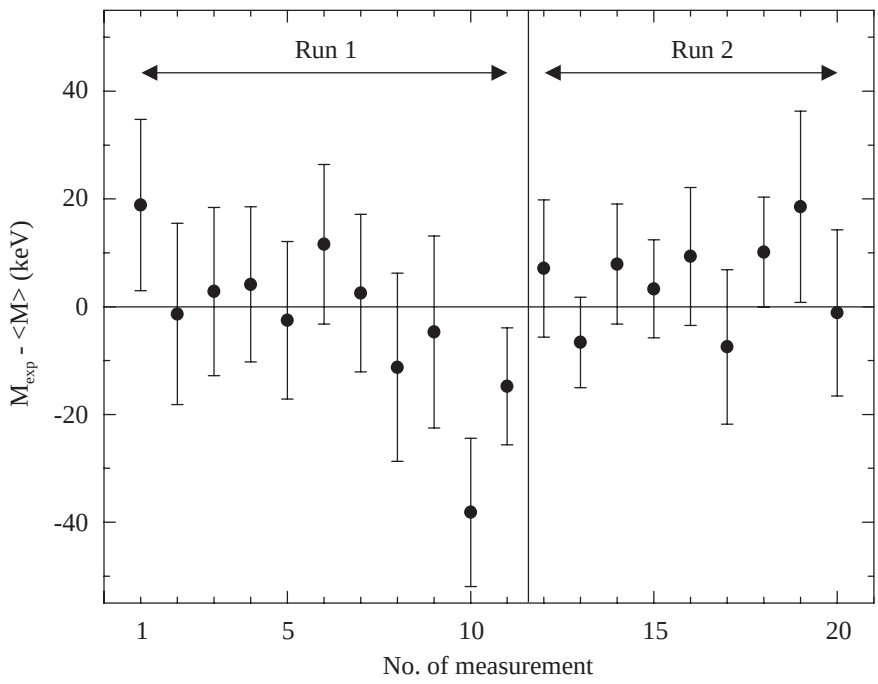

Figure 4.6: Results of the individual ^{147}Ho cyclotron resonances. Shown is the deviation from the weighted mean <M> for both experiments.

value was changed to 250(100) keV. With this excitation energy and a mixing ratio of $R_m = 0.74(15)$ (as described in section 4.3.1) the measured mass excess of −57805.4(8.8) keV was corrected to −57990(80) keV. The modification of the excitation energy similarly changes the correction of the previous result of −57815(30) keV [Lit05] from −58020(130) keV to −57940(90) keV. Like for ^{143}Tb an averaging of the two data would lead to an artificial decrease in the uncertainty. Therefore only the SHIPTRAP measurement will be considered in the AME since the original ESR result has a much higher uncertainty.

^{146}Er

The result of this measurement for ^{146}Er, −44325.0(8.6) keV, deviates from the previously estimated mass excess of −44710(300) keV by 390 keV. The adjusted mass excess results in −44322.0(6.7) keV. It is determined to 61% by this work and 39% by a Q_p measurement [Sel93] that links ^{146}Er with ^{147}Tm.

^{147}Er

For ^{147}Er, like for ^{146}Ho and ^{147}Ho, two independent measurements were made. The result of the first and the second run, −46522.7(9.9) keV and −46533.8(7.8) keV, respectively, are in good agreement with each other. ^{147}Er has an isomeric state with an estimated excitation energy of 100(50) keV. The spin and parity values of ground ($1/2^+$) and isomeric ($11/2^-$) state [Aud03a] correspond to those of ^{143}Dy and ^{147}Dy, hence the same mixing ratio ($R_m =$

0.741(13)) is assumed, leading to corrected mass values of −46600(40) keV and −46610(40) keV. For the final result only the latter value with the originally smaller uncertainty was taken since the averaging of the two values would result in an unreasonable decrease of the uncertainty. The value deviates from the previous estimate of −47050(300) keV by 440 keV.

^{148}Er

The mass excess of −51479(10) keV for ^{148}Er deviates from the previously estimated value of -51650(200) keV by 170 keV.

^{147}Tm

^{147}Tm has a very short-lived (360 μs) isomeric state [Sel93] that does not survive the stopping process in the gas cell. The ground state decays via proton emission to ^{146}Er. Since both mass values were measured the Q_p value of this decay can be determined to 1066(14) keV, which agrees with the known value of 1058(3) keV [Sel93]. The measured mass excess of −35969.8(9.9) keV deviates from the previously estimated value of −36370(300) keV by 390 keV. This is the same deviation as for ^{146}Er since the previously estimated mass excess was derived by combining the ^{146}Er estimate with the measured ^{147}Tm Q_p value. The adjusted mass excess results in −35974.4(6.8) keV influenced to 45% by this work and 55% by the Q_p measurement.

^{148}Tm

The mass excess measured for ^{148}Tm of −38765(10) keV deviates from the previously estimated value of −39270(400) keV by 500 keV. There is no indication in the spectra or the count rate class analysis of a possible isomeric state.

4.3.3 Results of the evaluation

Compared to the input values plotted in fig. 4.5 the adjustment procedure slightly changed the mass values of ^{147}Tb, ^{147}Dy, ^{148}Dy, ^{146}Er and ^{147}Tm. In all other cases the new mass value is determined only by the data from this work (c.f. tab. 4.3). The previous data from ^{143}Tb, ^{144}Dy, ^{145}Dy, ^{146}Dy, ^{147}Ho and ^{148}Ho do no longer contribute to the adjusted mass value due to significantly larger uncertainties. The results of the evaluation are plotted in fig. 4.7 together with the previous AME values. The lower graph shows a comparison for those nine nuclides for which the mass was already measured prior to this work. One recognizes the good agreement. The only deviation is found for ^{147}Ho. The most probable explanation is an unknown isomeric state that was measured in the previous experiment [Lit05].

The upper graph shows the comparison with masses estimated from systematic trends [Wap03]. The data show the general tendency that the nuclides in this region are less bound than predicted. Since all estimates are based on trends of the mass surface the new values demand the mass surface to rise. The

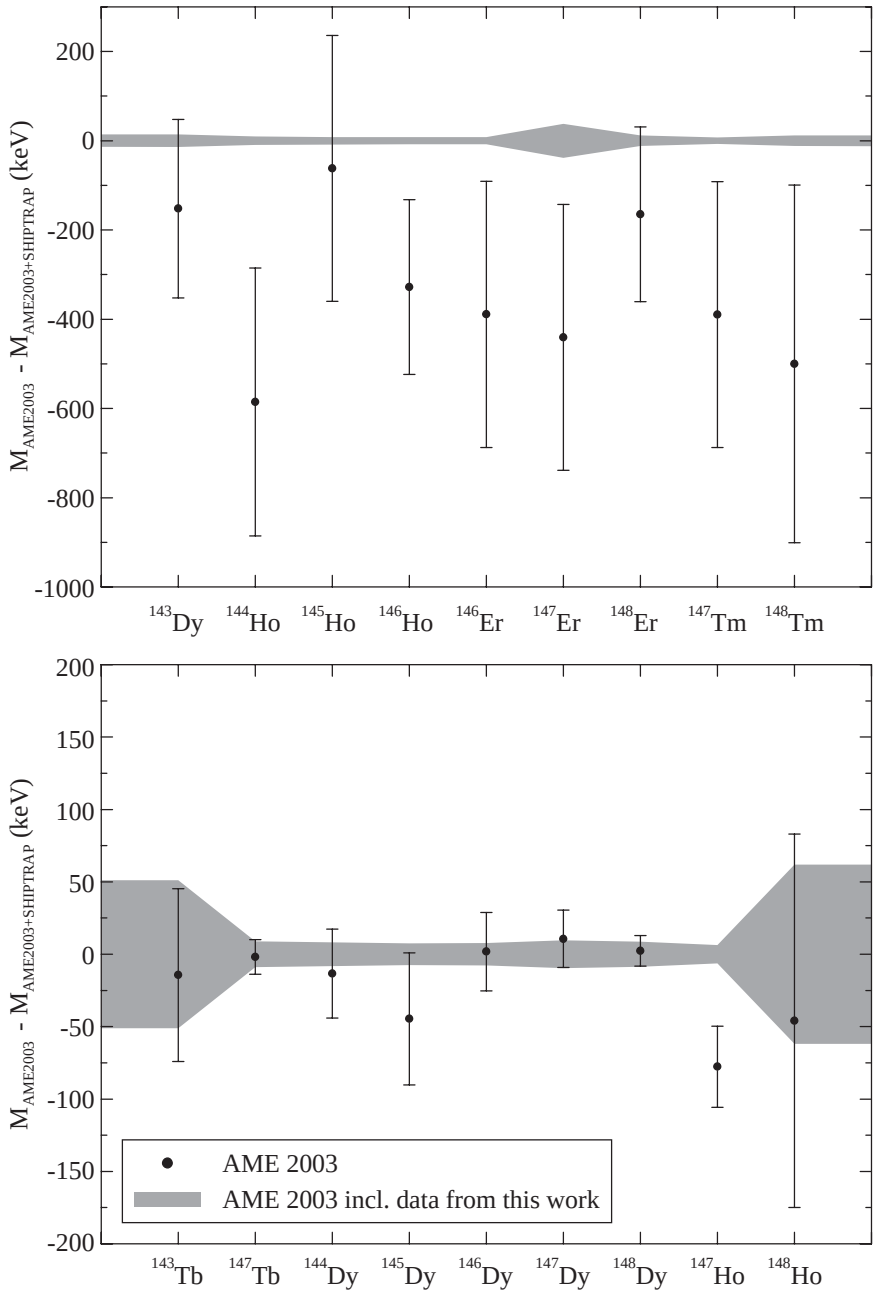

Figure 4.7: Comparison between the AME mass values before [Aud03b] and after the data from this work were included. The new data define the zero line. The uncertainties are indicated by an error band. The upper graph shows the comparison for those data that were only estimated from systematic trends prior to this work, while the lower graph compares them to already known but less accurately measured data. Only the mass values of ^{147}Tb, ^{147}Dy, ^{148}Dy, ^{146}Er and ^{147}Tm slightly differ compared to the data plotted in fig. 4.5 (c.f. tab. 4.3).

Table 4.4: Differences ΔM of masses extrapolated from systematic trends [Aud03b] and a new extrapolation taking the masses into account that were determined in this work.

Nuclide	ΔM (keV)	Nuclide	ΔM (keV)
^{126}Pm	180	^{138}Dy	150
^{126}Pm	180	^{138}Dy	150
^{127}Pm	110	^{139}Dy	60
^{128}Pm	80	^{140}Dy	110
^{128}Sm	100	^{141}Dy	90
^{129}Sm	160	^{142}Dy	-400
^{130}Sm	140	^{140}Ho	190
^{131}Sm	90	^{142}Ho	220
^{132}Sm	280	^{143}Ho	260
^{133}Sm	-140	^{143}Er	-120
^{134}Sm	110	^{144}Er	180
^{132}Eu	160	^{145}Er	270
^{133}Eu	200	^{149}Tm	160
^{134}Gd	290	^{150}Tm	120
^{136}Gd	130	^{148}Yb	150
^{138}Gd	120	^{149}Yb	300
^{139}Gd	-100	^{150}Yb	90
^{136}Tb	260	^{150}Lu	140
^{137}Tb	260	^{154}Lu	100
^{138}Tb	180	^{155}Ta	-200
^{139}Tb	180	^{156}Ta	-70
^{142}Tb	470	^{158}Ta	-130

manually performed reshape by Georges Audi primarily changes the estimates of several other nuclides but also effects the separation energies of this sector. Table 4.4 lists all 42 nuclides with a changed mass estimate.

In the neutron-deficient rare-earth region many masses have not been measured directly but are linked by α-decay chains to nuclides of known mass. The precise measurement of these 'base nuclides' automatically influences all connected nuclides. In this work the measurements of ^{147}Tb and ^{148}Dy also influenced the masses of 18 other nuclides via α chains up to ^{180}Pb, as can be seen in fig. 4.8. Since the masses of ^{147}Tb and ^{148}Dy were known before and are only changed by -2 keV and +2 keV, respectively, due to the new data, all dependent mass values are also only slightly modified.

In summary, the adjustment of the data presented in this work within the AME allows for two conclusions: First, the mass measurements in this mass region are obviously reliable in most cases. This can be seen in the good agreement with previous mass determinations stemming not only from Penning trap experiments but also from storage rings and Q_β measurements. In addition, the

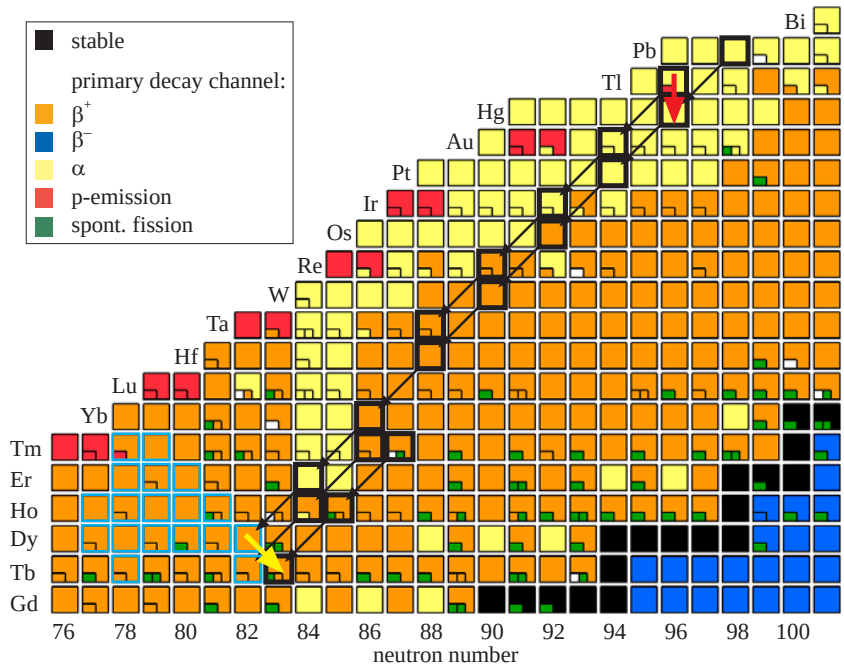

Figure 4.8: Influence of the mass measurements on other nuclides. The nuclides marked with a blue frame were directly measured. The black frame indicates nuclides that are linked by α decay chains (black arrows), β decay (yellow arrow) and proton decay (red arrow) to ^{147}Tb and ^{148}Dy.

results of the three nuclides measured in both runs (^{146,147}Ho and ^{147}Er) show that the mass values are reproducible. Second, the uncertainties attributed to the SHIPTRAP mass values are correct. This is confirmed by a partial consistency factor of $\chi^2_{\mathrm{red}} = 0.914$ for the SHIPTRAP data resulting from the AME adjustment procedure.

4.4 Discussion of the results

The new mass values allows one to get new insight in the nuclear structure in that region of the nuclear chart but also to determine the location of the proton drip-line more precisely. This is discussed in this section with the two-neutron and one-proton separation energies.

4.4.1 Two-neutron separation energies

The two-neutron separation energy S_{2n} is defined as

$$\begin{aligned} S_{2n} &= B(Z,N) - B(Z,N-2) \\ &= -M(Z,N) + M(Z,N-2) + 2M_n \quad , \end{aligned} \tag{4.6}$$

where $B(Z,N)$ and $M(Z,N)$ stand for the binding energy and the mass of a nucleus with Z protons and N neutrons and M_n is the mass of the neutron.

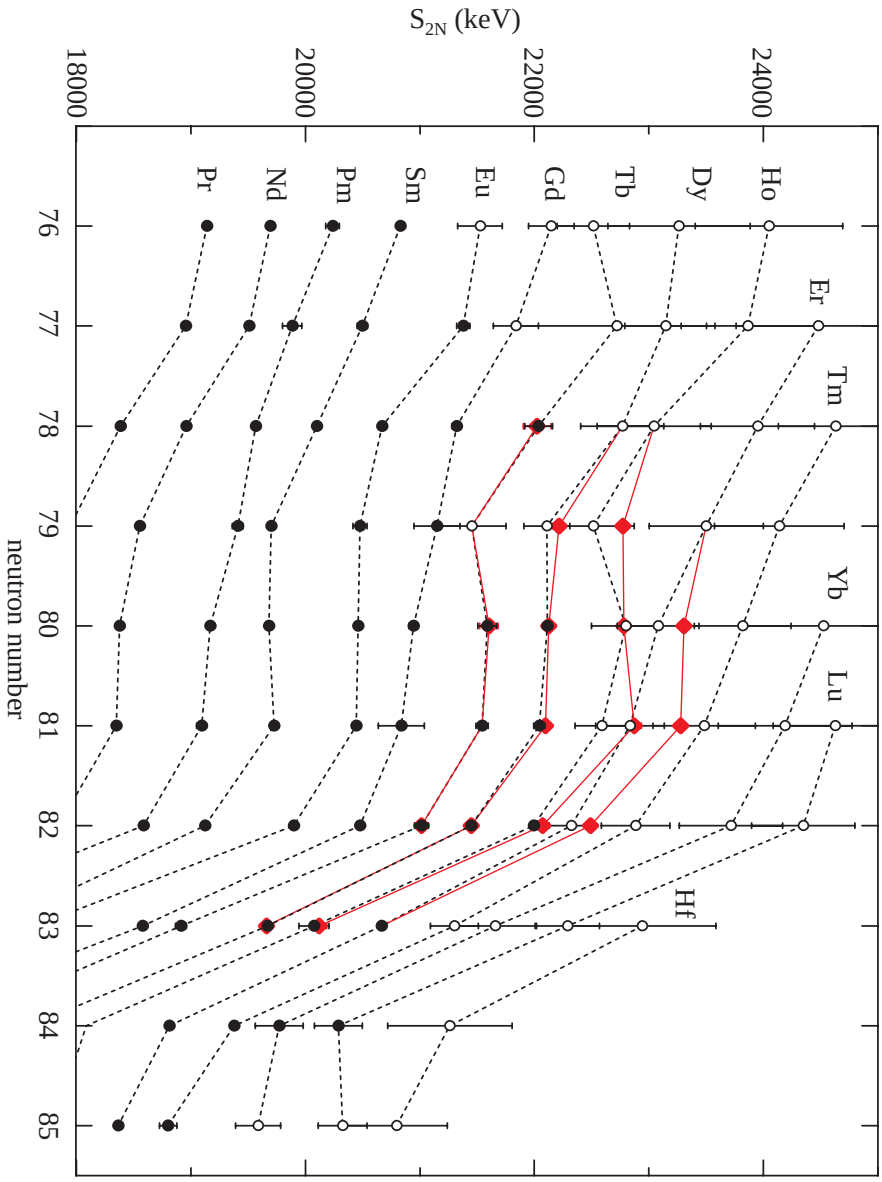

Figure 4.9: Two-neutron separation energies as a function of the neutron number for neutron-deficient isotopes of the elements praseodymium to hafnium. The circles, connected by dashed lines, show the previous data from [Aud03b]. Full circles correspond to measured data, while empty circles show values that are estimated from systematic trends. The data obtained in this work are indicated as red diamonds and connected by solid red lines.

Plotting S_{2n} as a function of N is an appropriate tool to visualize nuclear shell structure effects such as shell closures or shape transitions [Lun03].

Figure 4.9 shows the two-neutron separation energies for the region around ^{147}Ho. Going from the valley of stability towards the proton drip-line, one clearly recognizes the steep edge of the $N = 82$ shell closure followed by a plateau that indicates the transition from spherical to deformed shape. The known data are confirmed but the uncertainties are drastically reduced, which now gives clear evidence that the previously only estimated values shift to higher separation energies. Especially for the $N = 81$ isotones the values are significantly increased leading to a flat and more pronounced plateau for the elements dysprosium, holmium and erbium. The local minimum for ^{146}Ho at $N = 79$ was not confirmed. Both the shell closure as well as the deformation transition seem to persist for elements close to the proton drip-line. A shell quenching as it is known for neutron-rich $N = 82$ nuclides [Dil03] has not been observed for their proton-rich isotones.

4.4.2 Proton separation energies

The proton separation energy S_p, defined as

$$\begin{aligned} S_p &= B(Z,N) - B(Z-1,N) \\ &= -M(Z,N) + M(Z-1,N) + M_H \quad , \end{aligned} \tag{4.7}$$

where M_H is the atomic mass of hydrogen, allows one to distinguish between the proton-bound ($S_p > 0$) and the proton-unbound ($S_p < 0$) nuclei or in other words to determine the proton drip-line. From the present data the S_p values of four nuclides (^{144,145}Ho and ^{147,148}Tm) were determined to be negative. Table 4.5 shows the results in comparison with the previous values. Only ^{147}Tm is a known and measured proton emitter [Kle82, Sel93], while for the other three nuclides the S_p values had prior to this work only been deduced from mass estimates. However, due to the large uncertainties of these estimates, they did not allow for an unambiguous assignment of the sign of S_p and therefore of the position of the drip-line.

The determination of the proton drip-line on the basis of experimental data is visualized in fig. 4.10. Here the S_p values for the isotopes of the two elements

Table 4.5: Nuclides with negative S_p value. The partial half-lives for proton decay T_p are given in the last column according to eq. (4.8).

Nuclide	S_p (keV)		T_p (s)
	This work	Literature	
^{144}Ho	-271(16)	-160(360)	10^{25}
^{145}Ho	-161(10)	-110(300)	10^{40}
^{147}Tm	-1066(13)	-1058(3)	3
^{148}Tm	-560(40)	-490(500)	10^{11}

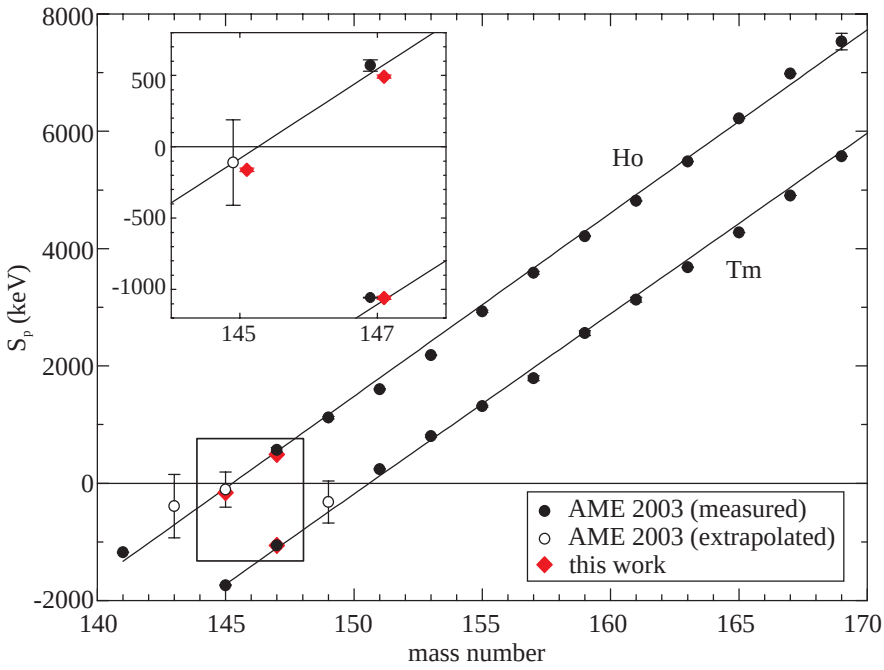

Figure 4.10: Proton separation energies versus mass number for the odd-Z elements holmium ($Z = 67$) and thulium ($Z = 69$). Only the even-N isotopes are plotted. Data from previous measurements (full circles) and estimates (empty circles) are taken from [Aud03b], while the data from this work are indicated as red diamonds. The lines show a linear fit of the data. For better visibility the inner box enlarges the interesting region around the drip-line.

holmium and thulium are plotted for their even-N isotopes only, thus avoiding the odd-even staggering due to the pairing energy. Three data points from the present work were included. The new S_p value obtained for ^{147}Tm agrees well with that determined previously [Sel93]. The measurement of ^{147}Ho slightly shifts the previous result to a lower separation energy. The value of ^{145}Ho was never measured before and the measurements clearly show that ^{145}Ho is proton-unbound. All data agree with the expected linear trend and confirm the location of the drip lines: between $A = 145$ and $A = 147$ for holmium and $A = 149$ and $A = 151$ for thulium.

The question whether the three new proton-unbound nuclides are accessible to investigations with proton spectroscopy can be answered by looking at the partial half-lives of this decay mode. In a simple, semi-empirical approach applying the WKB approximation the proton decay can be described similarly to the α decay [Hof95]. The decay constant

$$\lambda_p = \frac{\ln 2}{T_p} = \nu_0 \cdot e^{-2C_p} \tag{4.8}$$

is in this picture the product of a frequency factor ν_0 and an exponential transmission term. The factor ν_0 is in first order the inverse of the characteristic nuclear time and mainly defined by the velocity of the proton and the radius

of the nucleus. In the investigated region of the nuclear chart ν_0 has a typical value of $6 \cdot 10^{22}$ Hz [Hof95] and is more or less constant. The transmission term, usually called Gamow factor, describes the tunneling probability through the Coulomb and centrifugal potential barriers. The exponent C_p is the integral over the 'forbidden' region of the potential. It depends mainly on the energy and angular momentum of the proton and can be calculated numerically. An angular momentum of 5 was estimated by comparing the calculated half-life of ^{147}Tm with the measured one.

All calculated partial half-lives are shown in the last column of tab. 4.5. Only for ^{147}Tm the proton decay is an observable decay channel. While for ^{148}Tm it is experimentally very difficult to discriminate the proton from the β background, ^{144}Ho and ^{145}Ho are surely far out of reach for the study of proton decay as their partial half-lives for this decay mode are longer than the age of the universe.

Chapter 5

Summary and conclusions

This thesis gave an overview of the SHIPTRAP facility and showed results of off-line optimizations and on-line mass measurements. All parts of the SHIPTRAP setup, which are the gas cell including the extraction RFQ, the RFQ cooler and buncher and the Penning traps, are completed now and operate routinely. The measurement procedure and all important devices are fully computer controlled. Additionally, a real-time control system was set up for vacuum control and safety.

The properties of the gas cell window foils were investigated. Simulations showed how sensitively the stopping distribution and efficiency depend on the thickness of the foil. In a dedicated test setup consisting mainly of a α source and a silicon detector the window thickness was determined by measuring the energy loss of the α particles. The broadening of the α line was analyzed to obtain information on the roughness of the window foils. The results reproduced the specified thicknesses but also showed that the roughness of the investigated foils are on a scale that already affects the stopping efficiency. Here, on-line measurements of the stopping distribution will clarify the situation in the near future.

The contrast of the time-of-flight ion-cyclotron resonance curve was optimized. It was shown how the potentials of the ejection electrodes strongly influence the shape and quality of the resonance curve. The optimization led to an increase in contrast by 80 %, which allows one to determine the masses of radionuclides with only 300 ions.

Furthermore, uncertainties arising from fluctuations of the magnetic field were studied. The effects on the mass determination were described and a method to determine its magnitude presented. The uncertainty depends on the time between the reference measurements and increases the residual systematic uncertainty of $4.2 \cdot 10^{-8}$ by $3 \cdot 10^{-9}$/h.

The central part of this dissertation addresses mass measurements of neutron-deficient isotopes of the elements terbium to thulium. These are the first precision mass determinations performed at SHIPTRAP. In two on-line experiments the masses of 18 nuclides were measured. Highlights were the resolution of two isomeric states in ^{143}Dy and ^{147}Dy with excitation energies of

310 keV and 750 keV and the measurement of ^{147}Tm with a half-life of 580 ms and a production cross-section of only 100–200 μb. The SHIPTRAP set-up was operated with an overall efficiency of about $2 \cdot 10^{-4}$ and a mass resolving power of $1.2 \cdot 10^{6}$, which led to an average relative mass uncertainty of $6.8 \cdot 10^{-8}$.

The data were introduced into the Atomic Mass Evaluation. Nine nuclides had been measured before this work by Penning-trap, storage-ring and Q_β measurements. The new values show generally good agreement with the previous one but have a significantly improved accuracy. The only 3σ discrepancy found is that of ^{147}Ho. The origin of this deviation could lie in an unresolved isomer in the previous experiment. The masses of the other nine nuclides had not yet been measured prior to this work. They were only estimated by extrapolation of the mass surface. The masses from the newly measured nuclides were mainly lighter than the estimates, which led to a change in the mass surface and to refined estimates for yet unknown nuclides of that region.

Finally, the impact of the new mass data on the nuclear structure and the location of the proton drip-line were discussed. The two-neutron separation energies showed that the most prominent effects of this region, i.e. the $N = 82$ shell closure and the shape transition towards neutron-deficient nuclides, persist both up to the proton drip-line and beyond. The proton separation energies of four nuclides (^{144,145}Ho and ^{147,148}Tm) were determined to be negative, which pins down the location of the proton drip-line in this region more precisely. While ^{147}Tm was a known ground-state proton emitter, the other three nuclides had not yet been measured by means of proton spectroscopy. Simple model calculations of the partial half-lives showed that direct measurements of the proton decay are not feasible or, for ^{148}Tm, at least extremely ambitious.

The SHIPTRAP facility has the great potential to study also isotopes of transuranium or even transactinide elements. However, one feature of those nuclides above $Z = 100$ is that they exhibit comparably low production cross sections below 1 μb. One of the nuclides of that region with highest cross section, ^{254}No, has a measured cross section of 3.2 μbarn [Gäg89]. Comparing this to the measurement of ^{147}Tm (100-200 μb), which represents approximately the current limit of feasibility with respect to production cross sections, leads to the conclusion that a factor of 100 has to be gained. This should be in reach either by increasing the primary beam intensity and/or the efficiency of the SHIPTRAP setup.

Recalling tab. 2.6 on page 22, where the efficiencies of the individual segments of SHIPTRAP are listed, one might imagine the following improvements: A factor of three can be gained by changing the MCP detector (30 %) to a 100 % efficient channeltron. Additionally, a carefull optimization of the transfer and trap settings could result in another factor of four. The efficieny of the gas cell, where the biggest losses occur, is not easy to improve. To increase the extraction efficiency one needs higher electrical RF fields especially at the funnel electrodes that are not possible without discharges with the current design. A higher stopping efficiency asks for a higher gas pressure combined with thinner window foils, which is technically very demanding at the moment. Here, a

cryogenic gas cell would offer a higher gas density at constant gas pressure. For example, keeping the gas cell with a cryocooler at 77 K the density is increased by a factor of four. This reduces the width of the stopping distribution in the gas cell and enhances the stopping efficiency. Furthermore, the extraction efficiency could be also increased due to higher RF amplitudes that can be applied at the funnel.

Concerning the beam intensity a gain factor of ten is possible. ^{254}No is usually produced in the reaction ^{208}Pb(^{48}Ca, 2 n)^{254}No. The expensive isotope ^{48}Ca is ionized at GSI with an electron-cyclotron-resonance (ECR) source, which has a ten times higher beam intensity compared to the Penning source used for the here presented measurements. All these estimates show that the measurement of ^{254}No is already achievable with the present room temperature setup.

Next to mass measurements in the transuranium region major technical developments are under way. These are a redesign of the gas cell funnel and a high-efficiency detection setup. Furthermore, the current destructive TOF-ICR detection method will be replaced by the non-destructive Fourier-transform (FT) ICR method. A new trap system was constructed [Web05] and is currently being build up allowing to obtain cyclotron frequencies of single ions in the measurement trap by measuring their image currents in the trap electrodes.

Bibliography

[Alk93] G. D. Alkhazov, L. H. Batist, A. A. Bykov, F. V. Moroz, S. Yu. Orlov, V. K. Tarasov, and V. D. Wittmann. *Beta-decay energy measurements using total gamma-absorption spectroscopy.* Z. Phys. A **344**, 425 (1993).

[And62] P. W. Anderson. *Theory of Flux Creep in Hard Superconductors.* Phys. Rev. Lett. **9**, 309 (1962).

[And64] P. W. Anderson and Y. B. Kim. *Hard Superconductivity: Theory of the Motion of Abrikosov Flux Lines.* Rev. Mod. Phys. **36**, 39 (1964).

[Aud03a] G. Audi, O. Bersillon, J. Blachot, A. H. Wapstra, and C. Thibault. *The NUBASE evaluation of nuclear and decay properties.* Nucl. Phys. A **729**, 3 (2003).

[Aud03b] G. Audi, A. H. Wapstra, and C. Thibault. *The AME2003 atomic mass evaluation (II). Tables, graphs and references.* Nucl. Phys. A **729**, 337 (2003).

[Bec00] D. Beck, F. Ames, G. Audi, G. Bollen, F. Herfurth, H.-J. Kluge, A. Kohl, M. König, D. Lunney, I. Martel, R. B. Moore, H. Raimbault-Hartmann, E. Schark, S. Schwarz, M. de Saint Simon, J. Szerypo, and the ISOLDE Collaboration. *Accurate masses of unstable rare earth isotopes by ISOLTRAP.* Eur. Phys. J. A **8**, 307 (2000).

[Bec04] D. Beck, K. Blaum, H. Brand, F. Herfurth, and S. Schwarz. *A new control system for ISOLTRAP.* Nucl. Instr. and Meth. A **527**, 567 (2004).

[Bec06] D. Beck, H. Brand, C. Karagiannis, and C. Rauth. *The First Approach to Object Oriented Programming for LabVIEW Real-Time Targets.* IEEE Trans. Nucl. Sci. **53**, 930 (2006).

[Ber02] I. Bergström, C. Carlberg, T. Fritioff, G. Douysset, J. Schönfelder, and R. Schuch. *SMILETRAP - A Penning trap facility for precision mass measurements using highly charged ions.* Nucl. Instr. and Meth. A **487**, 618 (2002).

[Bie80] J. P. Biersack and L. G. Haggmark. *A Monte Carlo Computer Program for the Transport of Energetic Ions in Amorphous Targets.* Nucl. Instr. and Meth. **174**, 257 (1980).

[Bla06] K. Blaum. *High-accuracy mass spectrometry with stored ions.* Phys. Rep. **425**, 1 (2006).

[Bol96] G. Bollen, S. Becker, H.-J. Kluge, M. König, R. B. Moore, T. Otto, H. Raimbault-Hartmann, G. Savard, L. Schweikhard, and H. Stolzenberg. *ISOLTRAP: a tandem Penning trap system for accurate on-line mass determination of short-lived isotopes.* Nucl. Instr. and Meth. A **368**, 675 (1996).

[Bol01] G. Bollen. *Mass measurements of short-lived nuclides with ion traps.* Nucl. Phys. A **693**, 3 (2001).

[Bol06] G. Bollen, D. Davies, M. Facina, J. Huikari, E. Kwan, P. A. Lofy, D. J. Morrissey, A. Prinke, R. Ringle, J. Savory, P. Schury, S. Schwarz, C. Sumithrarachchi, T. Sun, and L. Weissman. *Experiments with Thermalized Rare Isotope Beams from Projectile Fragmentation: A Precision Mass Measurement of the Superallowed β Emitter ^{38}Ca.* Phys. Rev. Lett. **96**, 152501 (2006).

[Bro86] L. S. Brown and G. Gabrielse. *Geonium theory: Physics of a single electron or ion in a Penning trap.* Rev. Mod. Phys. **58**, 233 (1986).

[Cha06] A. Chaudhuri. *Carbon-cluster mass calibration at SHIPTRAP.* Accepted for publication in Eur. Phys. J. A (2006).

[Cul01] D. M. Cullen, C. Scholey, C. Fox, A. J. Boston, E. S. Paul, H. C. Scraggs, S. L. Shepherd, O. Stezowski, T. Enqvist, P. A. Butler, A. M. Bruce, P. M. Walker, M. Caamaro, J. Garcés-Narro, M. A. Bentley, D. T. Joss, P. T. Greenlees, K. Helariutta, P. M. Jones, R. Julin, S. Juutinen, H. Kettunen, M. Leino, M. Muikku, O. Dorvaux, P. Rahkila, J. Uusitalo, and P. Nieminen. *Recoil-isomer tagging near the mass 140 proton drip line.* Nucl. Phys. A **682**, 264c (2001).

[Deh90] H. Dehmelt. *Experiments with an isolated subatomic particle at rest.* Rev. Mod. Phys. **62**, 525 (1990).

[Dil03] I. Dillmann, K.-L. Kratz, A. Wöhr, O. Arndt, B. A. Brown, P. Hoff, M. Hjorth-Jensen, U. Köster, A. N. Ostrowski, B. Pfeiffer, D. Seweryniak, J. Shergur, W. B. Walters, and the ISOLDE Collaboration. *$N = 82$ Shell Quenching of the Classical r-Process "Waiting-Point" Nucleus ^{130}Cd.* Phys. Rev. Lett. **91**, 162503 (2003).

[Dwo06] M. Dworschak. *Optimierung der Zyklotronfrequenzbestimmung und Hochpräzisionsmassenmessungen an neutronenreichen Zinnisotopen mit ISOLTRAP.* Diploma thesis, Universität Mainz (2006).

[Dyc04] R. S. Van Dyck, S. L. Zafonte, S. Van Liew, D. B. Pinegar, and P. B. Schwinberg. *Ultraprecise Atomic Mass Measurement of the α Particle and ^{4}He.* Phys. Rev. Lett. **92**, 220802 (2004).

[Eli02] S. Eliseev. *Design, Construction and Commissioning of an Ortho-TOF Mass Spectrometer for Investigations of Exotic Nuclei.* PhD thesis, Universität Gießen (2002).

[Eli06a] S. Eliseev. *Extraction efficiency and extraction times of the SHIPTRAP gas-filled stopping cell.* Nucl. Instr. and Meth. B (2006), to be submitted.

[Eli06b] S. Eliseev. *Octupolar Excitation of Ions Stored in a Penning Trap Mass Spectrometer - a Study Performed at SHIPTRAP.* Int. J. Mass Spectrom. (2006), to be submitted.

[Emm93] J. Emmes. *Präzisionsmassenspektrometrie in der Penningfalle.* Diploma thesis, Universität Mainz (1993).

[Fau79] W. Faust, K. Güttner, G. Münzenberg, S. Hofmann, W. Reisdorf, K. H. Schmidt, and P. Armbruster. *The Efficiency of the Velocity Filter SHIP for Unslowed Evaporation Residues.* Nucl. Instr. and Meth. **166**, 397 (1979).

[Gab84] G. Gabrielse and F. C. Mackintosh. *Cylindrical Penning traps with orthogonalized anharmonicity compensation.* Int. J. Mass Spectrom. Ion Proc. **57**, 1 (1984).

[Gab89] G. Gabrielse, L. Haarsma, and S. L. Rolston. *Open-endcap Penning traps for high precision experiments.* Int. J. Mass Spectrom. Ion Proc. **88**, 319 (1989).

[Gab99] G. Gabrielse, A. Khabbaz, D. S. Hall, C. Heimann, H. Kalinowsky, and W. Jhe. *Precision Mass Spectroscopy of the Antiproton and Proton Using Simultaneously Trapped Particles.* Phys. Rev. Lett. **82**, 3198 (1999).

[Gäg89] H. W. Gäggeler, D. T. Jost, A. Türler, P. Armbruster, W. Brüchle, H. Folger, F. P. Heßberger, S. Hofmann, G. Münzenberg, V. Ninov, W. Reisdorf, M. Schädel, K. Sümmerer, J. V. Kratz, and U. Scherer. *Cold fusion reactions with ^{48}Ca.* Nucl. Phys. A **502**, 561c (1989).

[Grä80] G. Gräff, H. Kalinowsky, and J. Traut. *A direct determination of the proton electron mass ratio.* Z. Phys. A **297**, 35 (1980).

[Gui82] S. Z. Gui, G. Colombo, and E. Nolte. *A 150 ms 10^+ Isomer in ^{146}Dy.* Z. Phys. A **305**, 297 (1982).

[Har05] J. C. Hardy and I. S. Towner. *Superallowed $0^+ \rightarrow 0^+$ nuclear β decays: A critical survey with tests of the conserved vector current hypothesis and the standard model.* Phys. Rev. C **71**, 055501 (2005).

[Her01] F. Herfurth, J. Dilling, A. Kellerbauer, G. Bollen, S. Henry, H.-J. Kluge, E. Lamour, D. Lunney, R. B. Moore, C. Scheidenberger, S. Schwarz, G. Sikler, and J. Szerypo. *A linear radiofrequency ion trap for accumulation, bunching, and emittance improvement of radioactive ion beams.* Nucl. Instr. and Meth. A **469**, 254 (2001).

[Her03] F. Herfurth. *Segmented linear RFQ traps for nuclear physics.* Nucl. Instr. and Meth. B **204**, 587 (2003).

[Her06] A. Herlert, S. Baruah, K. Blaum, M. Breitenfeldt, P. Delahaye, M. Dworschak, S. George, C. Guénaut, U. Hager, F. Herfurth, A. Kellerbauer, H.-J. Kluge, D. Lunney, R. Savreux, S. Schwarz, L. Schweikhard, and C. Yazidjian. *High-precision mass measurements for reliable nuclear astrophysics calculations.* Proc. Sci. **51**, 1 (2006).

[Hof82] S. Hofmann, W. Reisdorf, G. Münzenberg, F. P. Heßberger, J. R. H. Schneider, and P. Armbruster. *Proton radioactivity of* ^{151}Lu. Z. Phys. A **305**, 111 (1982).

[Hof95] S. Hofmann. *Proton Radioactivity.* Radiochim. Acta **70/71**, 93 (1995).

[Hof00] S. Hofmann and G. Münzenberg. *The discovery of the heaviest elements.* Rev. Mod. Phys. **72**, 733 (2000).

[Huy02] M. Huyse, M. Facina, Y. Kudryavtsev, and P. Van Duppen. *Intensity limitations of a gas cell for stopping, storing and guiding of radioactive ions.* Nucl. Instr. and Meth. B **187**, 535 (2002).

[Jac70] K. P. Jackson, C. U. Cardinal, H. C. Evans, N. A. Jelley, and J. Cerny. $^{53}Co^{m}$*: A Proton-Unstable Isomer.* Phys. Lett. B **33**, 281 (1970).

[Kel95] H. Keller, R. Kirchner, B. Rubio, J. L. Tain, Th. Dörfler, W.-D. Schmidt-Ott, and E. Roeckl. *Beta-decay energy and atomic mass of* ^{148}Tb. Z. Phys. A **352**, 1 (1995).

[Kel03] A. Kellerbauer, K. Blaum, G. Bollen, F. Herfurth, H.-J. Kluge, M. Kuckein, E. Sauvan, C. Scheidenberger, and L. Schweikhard. *From Direct to Absolute Mass Measurements: A Study of the Accuracy of ISOLTRAP.* Eur. Phys. J. D **22**, 53 (2003).

[Kle82] O. Klepper, T. Batsch, S. Hofmann, R. Kirchner, W. Kurcewicz, W. Reisdorf, and E. Roeckl. *Direct and Beta-Delayed Proton Decay of Very Neutron-Deficient Rare-Earth Isotopes Produced in the Reaction* $^{85}Ni+^{92}Mo$. Z. Phys. A **305**, 125 (1982).

[Kol04] V. S. Kolhinen, S. Kopecky, T. Eronen, U. Hager, J. Hakala, J. Huikari, A. Jokinen, A. Nieminen, S. Rinta-Antila, J. Szerypo, and J. Äystö. *JYFLTRAP: a cylindrical Penning trap for isobaric*

beam purification at IGISOL. Nucl. Instr. and Meth. A **528**, 776 (2004).

[Kön95] M. Konig, G. Bollen, H.-J. Kluge, T. Otto, and J. Szerypo. *Quadrupole excitation of stored ion motion at the true cyclotron frequency.* Int. J. Mass Spectrom. Ion Proc. **142**, 95 (1995).

[Lit05] Yu. A. Litvinov, H. Geissel, T. Radon, F. Attallah, G. Audi, K. Beckert, F. Bosch, M. Falch, B. Franzke, M. Hausmann, M. Hellström, Th. Kerscher, O. Klepper, H.-J. Kluge, C. Kozhuharov, K. E. G. Löbner, G. Münzenberg, F. Nolden, Yu. N. Novikov, W. Quint, Z. Patyk, H. Reich, C. Scheidenberger, B. Schlitt, M. Steck, K. Sümmerer, L. Vermeeren, M. Winkler, Th. Winkler, and H. Wollnik. *Mass measurement of cooled neutron-deficient bismuth projectile fragments with time-resolved Schottky mass spectrometry at the FRS-ESR facility.* Nucl. Phys. A **756**, 3 (2005).

[Lun03] D. Lunney, J. M. Pearson, and C. Thibault. *Recent trends in the determination of nuclear masses.* Rev. Mod. Phys. **75**, 1021 (2003).

[Mar05] M. Marie-Jeanne. *Stabilisation en pression et en température du champ magnétique dans le piège à ions de précision d'ISOLTRAP au CERN.* PhD thesis, École Nationale Supérieure d'Ingénieurs de Caen (2005).

[Maz06] M. Mazzocho, private communication (2006).

[Mün79] G. Münzenberg, W. Faust, S. Hofmann, P. Armbruster, K. Güttner, and H. Ewald. *The velocity filter SHIP, a separator of unslowed heavy ion fusion products.* Nucl. Instr. and Meth. **161**, 65 (1979).

[Nei06] D. Neidherr. *Entwicklung einer Pumpsperre für das Penning-Fallen-Massenspektrometer SHIPTRAP.* Diploma thesis, Universität Mainz (2006).

[Neu06] J. B. Neumayr, L. Beck, D. Habs, S. Heinz, J. Szerypo, P. G. Thirolf, V. Varentsov, F. Voit, D. Ackermann, D. Beck, M. Block, Z. Di, S. A. Eliseev, H. Geissel, F. Herfurth, F. P. Heßberger, S. Hofmann, H.-J. Kluge, M. Mukherjee, G. Münzenberg, M. Petrick, W. Quint, S. Rahaman, C. Rauth, D. Rodríguez, C. Scheidenberger, G. Sikler, Z. Wang, C. Weber, W. R. Plaß, M. Breitenfeldt, A. Chaudhuri, G. Marx, L. Schweikhard, A. F. Dodonov, Y. Novikov, and M. Suhonen. *The ion-catcher device for SHIPTRAP.* Nucl. Instr. and Meth. B **244**, 489 (2006).

[Nov02] Yu. N. Novikov, F. Attallah, F. Bosch, M. Falch, H. Geissel, M. Hausmann, Th. Kerscher, O. Klepper, H.-J. Kluge, C. Kozhuharov, Yu. A. Litvinov, K. E. G. Löbner, G. Münzenberg, Z. Patyk, T. Radon, C. Scheidenberger, A. H. Wapstra, and H. Wollnik. *Mass mapping of a new area of neutron-deficient suburanium nuclides.* Nucl. Phys. A **697**, 92 (2002).

[Pfe98] G. Pfennig, H. Klewe-Nebius, and W. Seelmann-Eggebert. *Karlsruher Nuklidkarte.* 6. korrig. Auflage. Forschungszentrum Karlsruhe (1998).

[Rah05] S. Rahaman. *First on-line mass measurements at SHIPTRAP and mass determinations of neutron-rich Fr and Ra isotopes at ISOLTRAP.* PhD thesis, Universität Heidelberg (2005).

[Rau06a] C. Rauth. *Direct mass measurements around A = 146 at SHIPTRAP.* Accepted for publication in Eur. Phys. J. A (2006).

[Rau06b] C. Rauth. *Direct mass measurements beyond the proton drip-line.* Submitted to Phys. Rev. Lett. (2006).

[Rei81] W. Reisdorf. *Analysis of Fissionability Data at High Excitation Energies.* Z. Phys. A **300**, 227 (1981).

[Rod02] D. Rodríguez. *A Radiofrequency Quadrupole Buncher for SHIPTRAP.* PhD thesis, Universidad de Valencia (2002).

[Sav91] G. Savard, St. Becker, G. Bollen, H.-J. Kluge, R. B. Moore, Th. Otto, L. Schweikhard, H. Stolzenberg, and U. Wiess. *A new cooling technique for heavy ions in a Penning trap.* Phys. Lett. A **158**, 247 (1991).

[Sch98a] H. Schatz, A. Aprahamian, J. Görres, M. Wiescher, T. Rauscher, J. F. Rembges, F.-K. Thielemann, B. Pfeiffer, P. Möller, K.-L. Kratz, H. Herndl, B. A. Brown, and H. Rebel. *rp-Process Nucleosynthesis at Extreme Temperature and Density Conditions.* Phys. Rep. **294**, 167 (1998).

[Sch98b] C. Scheidenberger and H. Geissel. *Penetration of relativistic heavy ions through matter.* Nucl. Instr. and Meth. B **135**, 25 (1998).

[Sch01] H. Schatz, A. Aprahamian, V. Barnard, L. Bildsten, A. Cumming, M. Ouellette, T. Rauscher, F.-K. Thielemann, and M. Wiescher. *End Point of the rp Process on Accreting Neutron Stars.* Phys. Rev. Lett. **86**, 3471 (2001).

[Sch06] L. Schweikhard and G. Bollen (Ed.). *Ultra-Accurate Mass Determination and Related Topics.* Int. J. Mass Spectrom. **251**, 85 (2006).

[Sel93] P. J. Sellin, P. J. Woods, T. Davinson, N. J. Davis, K. Livingston, R. D. Page, A. C. Shotter, S. Hofmann, and A. N. James. *Proton spectroscopy beyond the drip line near A = 150.* Phys. Rev. C **47**, 1933 (1993).

[Sew97] D. Seweryniak, C. N. Davids, W. B. Walters, P. J. Woods, I. Ahmad, H. Amro, D. J. Blumenthal, L. T. Brown, M. P. Carpenter, T. Davinson, S. M. Fischer, D. J. Henderson, R. V. F. Janssens, T. L. Khoo, I. Hibbert, R. J. Irvine, C. J. Lister, J. A. Mackenzie,

D. Nisius, C. Parry, and R. Wadsworth. *In-beam γ-ray spectroscopy of the proton emitter $^{147}_{69}Tm$ using recoil-decay tagging.* Phys. Rev. C **55**, R2137 (1997).

[Sik03] G. Sikler. *Massenspektrometrie kurzlebiger Sr- und Sn-Isotope und Aufbau der SHIPTRAP-Penningfallen.* PhD thesis, Universität Heidelberg (2003).

[Tot93a] K. S. Toth, D. C. Sousa, J. M. Nitschke, K. S. Vierinen, and P. A. Wilmarth. *Identification of the $s_{1/2}$ ^{145}Dy ground state.* Phys. Rev. C **48**, 436 (1993).

[Tot93b] K. S. Toth, D. C. Sousa, P. A. Wilmarth, J. M. Nitschke, and K. S. Vierinen. *Electron capture and β^+b decay of ^{147}Tm.* Phys. Rev. C **47**, 1804 (1993).

[Wap03] A. H. Wapstra, G. Audi, and C. Thibault. *The AME2003 atomic mass evaluation (I). Evaluation of the input data, adjustment procedures.* Nucl. Phys. A **729**, 129 (2003).

[Web05] C. Weber, K. Blaum, M. Block, R. Ferrer, F. Herfurth, H.-J. Kluge, C. Kozhuharov, G. Marx, M. Mukherjee, W. Quint, S. Rahaman, and S. Stahl. *FT-ICR: A non-destructive detection for on-line mass measurements at SHIPTRAP.* Eur. Phys. J. A **25**, 65 (2005).

[Wei06] H. Weick, H. Geissel, C. Scheidenberger, P. Malzacher, and J. Kunzendorf. *The ATIMA program* (2006).
`http://www-linux.gsi.de/~weick/atima/`

[Woo97] P. J. Woods and C. N. Davids. *Nuclei Beyond the Proton Drip-Line.* Ann. Rev. Nucl. Part. Sci. **47**, 541 (1997).

[Xu03] S.-W. Xu, Y.-X. Xie, Z.-K. Li, X.-D. Wang, B. Guo, C.-G. Leng, C.-F. Wang, and Y. Yu. *(EC + β^+) decays of the $11/2^-$ isomer and $1/2^+$ ground state of ^{143}Dy.* Eur. Phys. J. A **16**, 347 (2003).

[Zie06] J. Ziegler. *SRIM + TRIM: Particles interacting with matter* (2006).
`http://www.srim.org/`

Acknowledgments

My sincere thanks go first of all to my Ph.D. supervisor Jürgen Kluge for offering me the position at SHIPTRAP and giving me help and advice whenever it was needed or necessary.

I am deeply grateful to my direct supervisors Michael Block and Frank Herfurth. Questions are surely an evident key to knowledge, but only if you find some way or someone to answer them. Luckily, I found the two as a permanent source of answers for my never ending questions.

SHIPTRAP is a large, still growing collaboration. From all of the many coworkers I especially like to thank the 'local' SHIPTRAPers Michael Dworschak, Ana B. Martín[2] and the Товарищи Sergey Eliseev and Gleb Vorobyev, but also my former colleagues Ankur Chaudhuri, Manas Mukherjee, Saidur Rahaman, Daniel Rodríguez and Christine Weber. I should not forget the associated HITRAPers notably my winterschool-roommates Stephen Koszudowski and Giancarlo Maero. It was a most excellent time.

Special thanks also to Georges Audi for his patience when introducing me into the big evaluation of the small masses, furthermore, to Yuri Novikov and Ernst Roeckl for their inspiration, suggestions and corrections particularly concerning the paper. I appreciate the scientific and substantial assistance from our SHIP colleagues, namely Sigurd Hofmann, Dieter Ackermann and Fritz Heßberger.

The wonders of LabVIEW were shown to me by Dietrich Beck and Holger Brand. I would like to thank them for their support and helpfulness.

Not only during the 'Schülerpraktikum' I experienced a lot of help from my AP colleagues. Representatively for all of them I would like to thank Fritz Bosch, Stefanie Lüttges, Heinrich Wesp and Davide Racano.

Summed up, I spend over 100 days during the three years in a car somewhere between Mainz and Wixhausen. That this time was not completely wasted is due to my car pool fellows Andreas Reiter and Guido Ewald. Thanks to vivid discussions commuting became almost enjoyable.

Last, but definitely not least, I want to thank Nina for her patience throughout the three years, for her understanding in the unusual working times and her constant effort in showing me that there is a life beyond physics.